UNIVERSITÀ DI PARMA

UNIVERSITÀ DEGLI STUDI DI PARMA

DOTTORATO DI RICERCA IN
“TECNOLOGIE DELL’INFORMAZIONE”

CICLO XXXIII

Energy-Aware Dynamic Control for Multi-Actuated Electric Vehicles

Coordinatore:
Chiar.mo Prof. Marco Locatelli

Tutore:
Chiar.mo Prof. Carlo Concari

Dottorando: Matteo Dalboni

Anni Accademici 2017/2018–2019/2020

Al due tempi
e alla miscela al 3%.

Sommario

I veicoli elettrificati si stanno diffondendo ad un ritmo notevole, risultato di politiche nazionali favorevoli, infrastrutture in espansione e progressi tecnici nell'ambito dei sistemi di accumulo dell'energia e dei controlli di veicolo. Senza dubbio i mezzi elettrici con azionamenti multipli si prestano a controlli dinamici più sofisticati, che proiettano maneggevolezza, stabilità, sicurezza ed efficienza energetica del veicolo ad un livello superiore.

Indubbiamente, lo sviluppo di algoritmi di controllo dinamici per autovetture si basa largamente su modellazione e simulazione. Perciò, si effettua una approfondita analisi delle tecniche di modellazione fondamentali, spaziando dal multibody fino alla formulazione massa-molla atta a descrivere corpi deformabili. Un veicolo generico viene quindi replicato mediante le diverse tecniche di modellazione e le implementazioni sono messe a confronto attraverso tre manovre significative. Ciò permette di valutare accuratezza, predisposizione ad impieghi in tempo reale e contesti di applicazione più adatti di ciascuna formulazione.

Successivamente, un veicolo multi-attuato e con quattro motori elettrici nelle ruote è studiato dal punto di vista dell'efficienza energetica. Tre sistemi di attuazione, ossia torque vectoring, distribuzione del momento di antirollio tramite sospensioni attive e sterzo posteriore, oltre ad una strategia di ripartizione longitudinale della coppia dei motori elettrici, sono esaminate attraverso simulazioni usando un modello di veicolo ad alta fedeltà e sperimentalmente validato. Nello specifico, le potenzialità di risparmio energetico delle attuazioni singole e combinate sono valutate nel corso di una serie di manovre a rampa di sterzo eseguite per diverse condizioni di velocità, aderenza e carico dei motori. L'analisi rivela buone capacità di risparmio energetico del torque vectoring e dello sterzo posteriore a basse e medie accelerazioni laterali e notevoli potenzialità di risparmio di potenza della distribuzione del momento di antirollio alle accelerazioni laterali medio-alte. Inoltre, in caso di carico addizionale ai motori, la ripartizione longitudinale della coppia può accrescere notevolmente l'efficienza.

In seguito, il controllo predittivo basato su modello non lineare è applicato al torque vectoring e al controllo di distribuzione del momento di antirollio di un veicolo elettrico con quattro motori indipendenti e sospensioni attive. La funzione di costo è volta a minimizzare le perdite di potenza e, al contempo, migliorare la risposta del veicolo sia in condizioni stazionarie, sia transitorie. Le potenzialità della strategia di controllo sono valutate su due manovre, rampa di sterzo e doppio colpo di sterzo, con e senza la distribuzione attiva del momento di antirollio a supporto del torque vectoring. I risultati mostrano notevoli miglioramenti apportati dall'integrazione del contributo delle sospensioni attive e del torque vectoring in termini di risparmio energetico e stabilizzazione del veicolo.

Abstract

Electrified vehicles are spreading at considerable rate, as a consequence of supportive national policies, infrastructure expansion and technical advances in the areas of energy-storage systems and vehicle controls. Doubtless, electrified vehicles with multiple drives create the conditions for more sophisticated dynamic controls, which project vehicle handling, stability, safety and energy-efficiency to a higher level.

Absolutely, the development of dynamic control algorithms strongly rely on vehicle modelling and simulation. Therefore, a thorough analysis about the fundamental modelling techniques, spanning from multibody to mass-spring soft-body formulation, is carried out. A generic vehicle is then replicated through the distinct modelling techniques and the implementations are compared thanks to three significant manoeuvres. The approach allows to assess accuracy, real-time readiness and suitable contexts of application of each formulation.

Subsequently, a multi-actuated fully electric vehicle equipped with four in-wheel-motors is investigated from an energy-efficiency viewpoint. Three systems of actuation, namely, torque vectoring, anti-roll moment distribution via active suspensions and rear-wheel steering, in addition to a longitudinal motor torque distribution strategy, are explored through a systematic simulation campaign by using an experimentally-validated high-fidelity nonlinear vehicle model. Specifically, power-saving capabilities of single and combined actuations are assessed along a set of ramp-steer manoeuvres performed at different speeds, adherence levels and workload conditions. The analysis reveals good energy-saving capabilities related to torque vectoring and rear-wheel steering at low-to-medium lateral accelerations, and a substantial power-saving authority connected to anti-roll moment distribution at medium-to-high lateral accelerations. Also, in the presence of additional powertrain workload, longitudinal motor torque distribution can increase considerably the energy-efficiency.

Afterwards, nonlinear model predictive control (NMPC) is applied to the torque vectoring and front-to-total anti-roll moment distribution control of a four-wheel-drive electric vehicle with in-wheel-motors and active suspension actuators. The NMPC cost function formulation strives to minimise the power losses due to longitudinal and lateral tyre slips and the electric powertrains, while enhancing the vehicle cornering response in steady-state and transient conditions. The capabilities of the proposed controller are evaluated through simulations along ramp steer and double-step steer manoeuvres, with and without the active anti-roll moment distribution together with torque vectoring. The results show the considerable enhancement of energy saving and vehicle stabilisation performance brought by the integration of the active suspension contribution and torque vectoring.

Contents

Introduction: mobility electrification **1**

A new era of transportation 1

Electrification is not limited to passenger car 2

An emblematic case study 4

Electrification and vehicle dynamics 9

Dynamic controls in favour of energy-efficiency 9

What to expect 10

1 Vehicle modelling **13**

1.1 Introduction 13

1.2 Equations of motion 14

1.2.1 Newton-Euler equations of motion 14

1.2.2 Lagrange's equations of motion 17

1.2.3 Deformable bodies equations of motion 22

1.3 Analytical vehicle models 27

1.3.1 Equations of motion of a planar vehicle model 27

1.3.2 Equations of motion of a three-dimensional vehicle model . 29

1.4 Mass-spring soft-body model fitting 32

1.5 Simulations 34

1.5.1 Path-follower driver 37

1.5.2 Remarks on computational time 39

1.6 Conclusion 41

2 Energy-efficiency of multi-actuated electric vehicles 47
2.1 Introduction 47
2.2 Analytical background 49
2.3 Simulation environment 54
2.3.1 The high-fidelity vehicle model 54
2.3.2 Simulation campaign 60
2.4 Post-processing methodology 62
2.4.1 Data filter design 62
2.4.2 Extraction of the minimum power envelope 64
2.5 Simulation results 66
2.5.1 Relative distribution of minimum power 66
2.5.2 Relative profile of minimum power: optimal curve 70
2.5.3 Relative profile of minimum power: arbitrary curves 79
2.6 Conclusion 88

3 Energy-efficient torque vectoring and anti-roll moment control 91
3.1 Introduction 91
3.2 Internal model equations 94
3.3 Optimal control problem formulation 104
3.4 Controller implementation and virtual assessment 109
3.4.1 Ramp steer manoeuvre 112
3.4.2 Double step steer manoeuvre 118
3.5 Conclusion 123

Conclusion 127

A Code for extracting the subset for minimum power envelope 131

B Relative distribution of minimum power: additional figures 137

C Relative profile of minimum power: additional figures 141

Bibliography 155

Introduction: mobility electrification

A new era of transportation

Nowadays, we are experiencing a quite remarkable phenomenon in the field of transportation and mobility. After several years of general distrust on the part of the market, to some extent fed by factual technical and economic limitations, consumers' perception and attitude towards electrified vehicles has been changing substantially. Improved technologies, enhancements of infrastructures, incentives and a reduced purchase price have contributed to attract consumers and businesses to choose the electric alternatives [1]. Indeed, in the presence of incentives, high utilisation and larger-sized vehicles, electrified solutions are more cost-competitive than those equipped with internal combustion engine when considering the long-term costs of ownership [2]. As a matter of fact, battery replacement costs still influence the capability of electric vehicles to be cost-competitive with traditional alternatives [2]. However, the developments in the field of Li-ion battery materials and technologies have turned into increased energy density and overall battery pack cost drop. The late versions of some common electric car models display a battery energy density that is 20-100% higher compared to their counterparts in 2012 and the battery cost is more than 85% lower than was in 2010 [1]. And battery price is likely to fall more in the next years. After all, industry reports indicate a very eloquent fact: the average battery pack cost per kWh dropped from approximately 1100 USD/kWh in 2010 to 156 USD/kWh in 2019.

As a results, a higher number of electric vehicle with longer range is available to fulfil the rising mass-market demand. This virtuous circle is further fed by many national governments which are boosting the mobility electrification through supportive policies for electric vehicle purchase. Measures that find a place in higher projects for polluting emissions abatement against global warming such as the European Green Deal. In addition, the charging infrastructure displayed, in 2019, 7.3 million chargers worldwide, of which 6.3 were private [1]. As a result, despite the stagnant sales of passenger cars, 2019 featured another extraordinary increase of electric cars globally, which topped 2.1 million [1].

Indeed, the growing number of hybrid and, even more, fully electric vehicles that travel on public roads testifies also how their range is no longer such an overwhelming concern. In addition to an increased number of private and publicly accessible charging points, progress that brought to range extension of electrified vehicles must be sought both in the electrochemical field and the vehicle control area. The former research domain is related to the development of novel energy-conversion and storage systems, namely batteries with higher density. The latter realm concerns the strategies that allow for a better management of the energy resources, possibly in connection with vehicle dynamics.

Electrification is not limited to passenger cars

Interestingly, the electrification phenomenon is not limited to lightweight on-road cars, but it is also affecting the area of heavy-duty [1] and off-road vehicles [3, 4, 5], with no exclusion of the agricultural sector [6, 7], though with some peculiar motivations [8].

The internal combustion engine (ICE) of a light-duty vehicle such as a passenger car has typically a dynamic and varied spectrum of operation, which may incorporate regions with poor energy-efficiency. Hence, the main purpose of a hybrid system is to allow the engine to function in the most efficient area as much as possible. To this end, the excess energy converted by the engine is stored and delivered when needed to actuate the motors. On the contrary, off-road vehicles very often operate at constant speed and load for a protracted time. Frequently, they work at low speed while needing high torques; moreover, they spend long periods in idling conditions [5].

Briefly, the main reasons supporting the electrification of off-road vehicles such as agricultural tractors are listed hereinafter [9].

- *Engine downsizing*. Indeed, the downsizing of the engine is an essential requirement to meet the new European regulation 2016/1628 (better known as STAGE V) [10], which defines the emission limits for engines in non-road mobile machinery (category NRE), and, ultimately, to reduce the emissions without resorting to auxiliary components. In fact, according to the aforementioned regulation, expensive, bulky and invasive systems (i.e. urea injector and tank, selective catalytic reduction devices, modified post-treatment system etc.) are mandatory above the 55 kW power size.

- *Enhancement of the range of functionalities of a traditional architecture*. In fact, the addition of the electric motors beside the internal combustion engine widens considerably the capabilities of an off-road vehicle. Primarily, it is possible to use the same vehicle outdoor and indoor; the operations inside greenhouses and sheds can be performed in full-electric, thus averting, for instance, livestock intoxication. Secondly, a motor can be utilised as an effective replacement for the so-called creeper gear, that is a suitable mechanism for very low speed motion. This operating condition is extremely demanding and inefficient for a traditional solution because of the small gear ratio and the bad working region of the engine. Conversely, in the same conditions, an electric motor offers a high amount of torque and a very low energy consumption. Thirdly, a motor can act as a parking brake and it helps the driver to smooth start-and-stop transitions on sloping surfaces while reducing the clutch overload and the related overheating [11].

- *Factual energy saving*. Naturally, vehicle electrification, which typically affects also the auxiliaries [12, 13], enhances considerably the overall energy-efficiency of the system compared to traditional solutions. Certainly, this is a paramount incentive for the development of hybrid or full-electric passenger cars, but it is also a good reason to spread the technology in the sector of heavy-duty off-road vehicles.

An emblematic case study

An emblematic case study concerning the electrification of a compact farm tractor is described by [11]. It constitutes a very effective example to convey the remarkable potentialities of electrified agricultural vehicles in connection with proper rule-based powertrain control strategies. For this reason, the study is presented in detail below, going through the construction details, the control schemes and the simulation results.

The starting point of the electrification is the downsizing of a Diesel engine from a 4-cylinder 77 kW (used in the pre-existing design) to a 3-cylinder 55 kW unit, the basic step to meet the STAGE V European regulation. The additional room that is obtained through the cylinder removal allows to insert supplementary components without increasing the vehicle wheelbase. Namely, an up-to 60 kW permanent magnet (PM) motor is connected to the ICE to implement a P2 parallel-hybrid scheme. The fundamental advantages deriving from this architecture are described in [14]: among these, the possibility to operate in full electric mode by decoupling the ICE and the motor through the clutch and the opportunity to force the ICE to work in a more efficient region. The motor choice is driven by the need to work in full-electric mode and in continuous conditions in a wide range of scenarios. Moreover, a hydraulically-actuated clutch, which is in charge of decoupling the engine and the motor to attain the desired policies, is positioned between them. The battery pack is based on $LiFePO_4$ cells, which are suitable for such application thanks to the high thermal stability and safety in case of perforation or crash [15, 16]. The 25 kWh-rated battery pack is adequate to ensure a wide range of operations in full-electric mode, and to store a sufficient amount of excess energy deriving from a smart control of the powertrain. Moreover, the selected battery pack capacity is appropriate for maintaining the C-rate within the proper limits.

A Pareto optimisation is performed to determine the optimal threshold in terms of power under which the full-electric mode is automatically activated. This value

Table 1: Description of the sub-modes of the hybrid mode: the energy management of the electric motor is defined by its torque T_{em}. P_{req} is the power request, $P_{ice,max}$ is the maximum power the engine can deliver at the given speed, $P_{ice,\eta}$ is the maximum efficiency power level at the given speed, SOC is the state of charge

Sub-mode	EM torque	Condition
Full ICE	$T_{em} = 0$	(User choice AND $P_{req} \leq P_{ice,max}$) OR $P_{ice,\eta} < P_{req} < P_{ice,max}$ OR $\text{SOC} \geq \text{SOC}_{\text{max}}$ OR $\text{SOC} \leq \text{SOC}_{\text{min}}$
Battery charge	$T_{em} < 0$	$\text{SOC} < \text{SOC}_{\text{max}}$ AND $P_{req} < P_{ice,\eta}$
Power boost	$T_{em} > 0$	$\text{SOC} > \text{SOC}_{\text{min}}$ AND $P_{req} > P_{ice,max}$

must be a good compromise to reduce the fuel consumption, increase the battery life, decrease the engine usage and limit the number of starts and stops of the ICE. It turns out that, for the given application, 15 kW is the best threshold.

An interesting aspect of the implementation in question is the strategy that rules the transition between the full-electric and the hybrid mode. This procedure is depicted in Fig. 1 through a simplified Finite State Machine (FSM). Briefly, the strategy is such that the the transition from full-electric (Full-E) to hybrid takes place when the rotational speeds of motor (ω_{EM}) and engine (ω_{ICE}) are essentially equal to each other, which is the condition that allows to minimise the slip during clutch engagement. To achieve the velocity equality condition, both units are controlled in terms of speed. Subsequently, within hybrid mode, the electric motor (EM) is subject to torque control. To revert back to Full-E state, EM is put again under speed control to prevent excessive spinning and then, after clutch disengagement, it is turned off. Regarding the hybrid mode, electric motor torque T_{em} can be zero, in case of full ICE mode, negative for battery charge purposes, positive for assisting the ICE in the most burdensome tasks. The details about the hybrid sub-modes are condensed in Table 1. Furthermore, during the ‘Battery charge’ sub-mode, the control strategy manages the electric motor in order

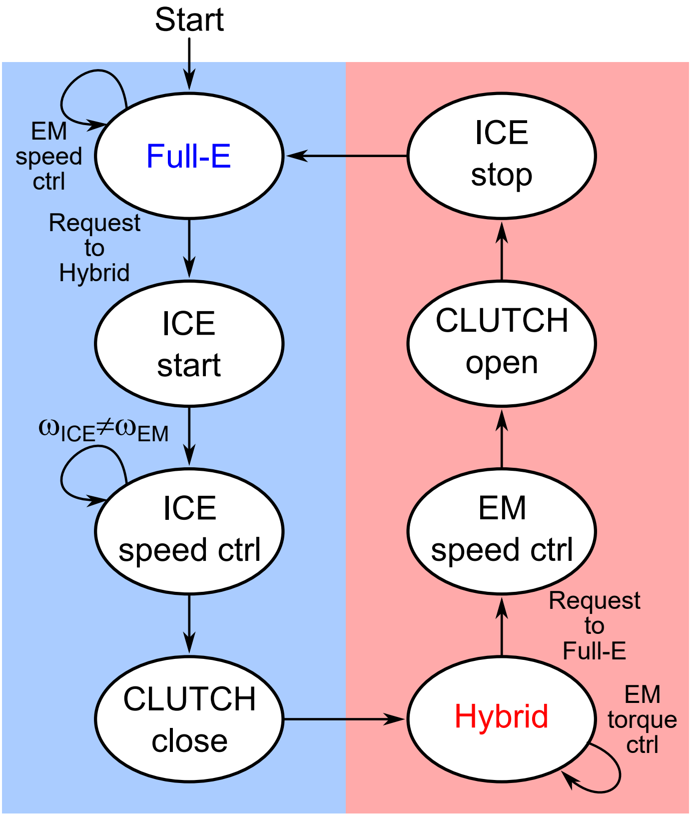

Figure 1: Simplified Finite State Machine for the transition between full-electric and hybrid modes. The tractor always starts in full-electric mode.

to induce the engine to operate within the high-efficiency region. This is accomplished through a regenerative braking programme: the amount of power that exceeds the demand is recovered by means of the electric motor. Thus, the stored energy can be employed by the electric unit itself to carry out special tasks requiring high torque at low speed and to assist the engine. This is, in fact, an established technology for light-duty hybrid cars [17]. Moreover, the control ensures that the battery state of charge (SOC) is always between 60% and 80%. When the SOC reaches the lower bound (SOC_{min}), charging occurs until the upper limit is reached; subsequently, the discharge takes place as long as the SOC is above the lower value. Moreover, the upper limit is recommended to preserve the battery pack health [18], whereas the lower bound is conceived as the energy that allows the operator to perform a task for an hour in full-electric mode. Essentially, the electric unit acts as a motor when the requested torque is greater than the maximum amount that the ICE can deliver: in this case, the motor provides the difference in terms of torque. Conversely, if the needed torque is lower than that given by the ICE, and the SOC is within the above-mentioned bounds, the electric unit acts as a generator by braking the ICE; also, the dissipative braking due to the hydraulic system occurs when the state of charge is above the superior limit of the SOC ($\mathrm{SOC}_{\mathrm{max}}$).

Therefore, a simulation campaign is conducted based of the experimental workloads of the twelve duty cycles identified from real life scenarios and measured on the baseline traditional ICE-based tractor without hybridisation. These cycles are characterised by different load profiles for the towing activity, for the power take-off (PTO) and for the electrically-actuated hydraulic pumps. The simulation-based approach allows to assess the power-saving potentialities of the electrification in conjunction with the proposed empirical and rule-based strategies described above. Interestingly, the simulations show that the control scheme can translate to substantial energy usage reduction in many scenarios. The numerical results are summarised in Table 2 and the fundamental outcomes are listed below.

- The consumption benefit relative to the original engine is always possible in hybrid mode.

- With respect to the duty cycles requiring high average power (cycles 1–7 in Table 2), the benefit ranges from 3% to 6.9%. However, the advantage is ascribable almost exclusively to the engine downsizing rather than to the control strategy.

- If the average power request is high as in cycles 1–7, full-electric mode is even counterproductive and detrimental due to the repeated energy switches and to the high battery current.

Table 2: Specific fuel consumption related to the different duty cycles and benefits deriving from hybrid and full-electric modes.

Cycle ID	Average Power of the Cycle [kW]	Average Original ICE Specific Fuel Consumption [g/kWh]	Hybrid Consumption Benefit [%]	Full-electric Consumption Benefit [%]
1	35.6	256.6	4.6	-9.7
2	33.4	286.1	6.9	1.7
3	28.7	267.1	6.2	-5.4
4	29.9	262.9	6.2	-7.0
5	34.9	264.5	6.1	-6.4
6	12.0	332.4	3.0	n/a
7	16.2	260.5	6.4	-8.0
8	6.5	478.2	39.2	41.2
9	6.7	461.6	38.0	39.1
10	6.7	350.8	22.8	19.8
11	3.9	375.6	28.3	25.1
12	2.6	404.6	33.6	30.5

- Significant benefits connected to the electrification can be obtained during those cycles that, on average, need less energy (cycles 8–12) both in hybrid and full-electric mode. In this case, the convenience is also connected to the usage of the electric motor as a replacement to the creeper gear, avoiding the ICE to work for a protracted time in unfavourable conditions. A further benefit related to these low-power cycles is the fact that, due to the relatively low energy consumption, the battery discharge is slow, allowing to keep the engine off for a long period.

Electrification and vehicle dynamics

It is evident that the limited accelerations experienced by an agricultural tractor legitimate completely an energy-oriented optimisation process which neglects the dynamic response of the system. However, this may not be the case for a light-duty vehicle such as a passenger car because this can operate also in more challenging transient scenarios. As a matter of fact, the electrification also brings a dowry of flexibility in terms of powertrain architecture which may turn into remarkable advantages on the side of vehicle dynamics. Multiple motors as independent drives set the scene to torque vectoring (TV), a strategy that aims to allocate the motor torques disjointly in order to inject the desired direct yaw moment. Doubtless, its effects on vehicle handling and stability are massive, especially because they go largely to the benefit of safety, which is priceless [19].

In the last decades, some other actuations for general road vehicles have been extensively studied from a handling and stability viewpoint and, as the mobility shifts towards the electrification, such systems find new applications in tandem with the novel powertrains. Undoubtedly, rear-wheel steering and active suspensions for longitudinal roll stiffness distribution purposes play a leading role. A thorough analysis of the two systems in addition to individual driving and braking torque allocation is presented in a work that dates back to 1994 [20], which is a confirmation of how much these technologies are established in automotive for influencing yaw moment.

Dynamic controls in favour of energy-efficiency

Not only affects torque vectoring the cornering response of the vehicle, giving considerable advantages in terms of handling and stability even in the most safety-critical scenarios, but it also influences the mechanical and electrical power losses, uncovering some relevant energy-saving potentialities. In fact, in the last years, torque vectoring has also gained a prominent role as a strategy for enhancing the energy-efficiency while preserving its unquestionable dynamic benefits [21, 22, 23, 24]. Indeed, a torque vectoring strategy is viable for tracking the so-called energy-efficient understeer characteristic [25, 26], that is, a properly shaped understeer curve which allows to minimise the overall power usage thanks to the better state in which powertrain and tyres work. For clarity, the understeer characteristic is the function that relates the steering wheel angle to the lateral acceleration of the vehicle, thus indicating its cornering behaviour. With respect to rear-wheel steering, there are some works that investigated its energy-efficiency potentialities, especially in conjunction with torque vectoring. A noteworthy and recent example is [27], in which active rear steering and propulsion on individual wheels are investigated for improving the cornering energy-efficiency in non-safety-critical scenarios. Interestingly, the study revealed some remarkable energy-saving capabilities connected to the double actuation. As regards the power-saving aspect of active suspensions, there exists a number of works which address the energy efficiency of the suspension actuators themselves [28, 29]. Another study describes how to exploit the regenerative capabilities of the suspensions [30]. However, energy-related effects of roll moment distribution in connection with vehicle cornering response are still uncharted.

What to expect

Given the premises, this thesis aims to extend the analysis concerning the energy-efficiency descending from multiple actuations in connection with electric vehicles with independent drives.

Owing to the paramount role of dynamics modelling for the sake of vehicle response exploration and control development, Chapter 1 is entirely devoted to modelling techniques, including rigid and soft-body dynamics, that make possible the simulation of a vehicle system.

Chapter 2 deepens the exploration on energy-saving capabilities of single and combined actuations, namely, individual motor torque allocation, rear-wheel steering and roll stiffness distribution via active suspensions, for different speed, friction and workload conditions. To this end, a comprehensive simulation campaign is performed.

Based on the outcomes of the previous chapters, Chapter 3 deals with the development of an integrated energy-efficient model predictive control oriented to optimal wheel torque allocation and allotment of anti-roll moment between front and rear axles. The controller is assessed through simulations by using an experimentally validated high-fidelity vehicle model, along ramp steer and multiple step steer manoeuvres, including and excluding the direct yaw moment and active anti-roll moment distribution actuations.

Therefore, the ultimate objectives of the present thesis are:

- presenting a comprehensive assessment of the power-saving authority regarding torque vectoring, anti-roll moment distribution and rear-wheel steering;
- proposing an integrated control algorithm suitable for managing two of the aforementioned systems (with the exclusion of rear-wheel steering, which will be considered in future works) for power-loss minimisation while honouring dynamic and safety-critical constraints.

The author has already explored the field of model-based design devoted to vehicle electrification [31, 32, 33, 11], including a contribution from power converters reliability perspective [32]. Additionally, the author has detected an alternative modelling technique as a viable approach also for dynamic vehicle control [34].

Chapter 1

Vehicle modelling

1.1 Introduction

Vehicle models are fundamental tools for car makers and researchers. Thanks to them it is possible to speed up dramatically the development process of a vehicle: a wide range of working conditions can be explored in a faster, safer and relatively cheaper way since the number of experiments and tests in the real world can be significantly reduced. Furthermore, in the last years, by virtue of the growing spread of hybrid and electric vehicles, dynamic control strategies have become more sophisticated and elaborate, as demonstrated by torque vectoring (TV). Indeed, the design of these algorithms typically relies largely on car simulators [35, 36].

Of course, there are many different kinds of vehicle models; each of them is the result of a peculiar theoretical approach and set of approximations. Naturally, if the purpose is to design control algorithms to manage the driving and braking torque allocation among the motors, at least a planar model is required to account for the lateral dynamics and the vertical load distributions on the four wheels. This typology of car model is widely used inside state observers, state predictors and reference generators for dynamic control strategies [37, 38, 39, 40]. Additionally, if a more accurate simulation is needed to describe the vertical dynamics and the vehicle behaviour on an arbitrary surface while preserving a very low computational load, the choice could fall on a three-dimensional single rigid body model. However, if accuracy is the priority, multibody modelling should be selected [41]. In addition, an alternative approach to describe the vehicle system as a deformable entity is given by the soft-body physics formulation based on the mass-spring model (MSM), as demonstrated by a couple of vehicle simulators [42, 43]: MSM can be very attractive thanks to its low computational load. Therefore, the choice of a vehicle model must be accurately pondered.

This chapter is intended as a survey about the most convenient modelling techniques that can be adopted to develop a vehicle model and about the most notable simulators that are already available, with special attention towards open source solutions, namely Project Chrono and Rigs of Rods. Simplified analytical car models as well as multibody models made of rigid or deformable bodies are reviewed, digging into the equations that rule their dynamics; the mass-spring formulation applied to the vehicle simulation is also analysed. These simulators, besides a commercial one (CarSim), are compared through three significant manoeuvres (elk test, circle path, slalom), to point out their accuracy, parameters tuning effort and computational burden in sight of real-time application.

1.2 Equations of motion

1.2.1 Newton-Euler equations of motion

Newton-Euler equations of motion represent the classic formulation to describe the dynamics of a mechanical system. This method relies on the balance of forces and moments acting on a system; thus, it is essentially in contrast with the energy approach of the Lagrangian dynamics, which will be discussed in the next section.

Certainly, Newton-Euler equations are often adopted as a starting point to develop basic vehicle simulators thanks to their simplicity and clarity, but they can also be utilised as the basis for more complex models like multibody software.

Before deriving the equations of motion for the rigid body, it is fundamental to distinguish among the ground coordinate system, which is inertial, and the body coordinate system, which is rigidly connected to the centre of gravity of the body itself. It is thus essential to recall the equation that establishes the relationship between the absolute time derivative $\left(\frac{D}{Dt}\right)$ and the relative time derivative $\left(\frac{d}{dt}\right)$ of a generic vector function $\boldsymbol{h}(t)$; notice that the former is calculated with respect to the fixed reference frame, whereas the latter is calculated with respect to a moving system of reference that rotates according to the angular velocity vector $\boldsymbol{\omega}_\tau$. Thus, the above-mentioned equation is

$$\frac{D\boldsymbol{h}(t)}{Dt} = \frac{d\boldsymbol{h}(t)}{dt} + \boldsymbol{\omega}_\tau \times \boldsymbol{h}(t) \tag{1.1}$$

where the symbol $(\times)$ indicates the cross product.

First of all, consider the translation of a rigid body with respect to the ground reference frame; by using a Cartesian coordinate system, the absolute centre of gravity position is identified by Newton's equation

$$m\frac{D\boldsymbol{v}}{Dt} = \sum_k \boldsymbol{f}_k \tag{1.2}$$

in which m is the body mass, which is assumed to be constant, $\boldsymbol{v}$ is its speed and $\boldsymbol{f}_k$ is the k-th force acting on the body. It may be useful to point out that, if the speed is defined with respect to the inertial frame, the absolute time derivative and the relative one coincide.

As regards the balance of moments, it may be convenient to express the Euler's equation with respect to the body coordinate system especially for one reason: the rigid body inertia tensor $\bar{\boldsymbol{I}}_{\theta\theta}$ expressed in the body frame is constant during the motion. Quantities that are defined in respect of the body frame will be denoted by the bar over the symbol henceforth. In particular, $\bar{\boldsymbol{I}}_{\theta\theta}$ is defined as follows:

$$\bar{\boldsymbol{I}}_{\theta\theta} = \begin{bmatrix} I_{11} & I_{12} & I_{13} \\ & I_{22} & I_{23} \\ sym. & & I_{33} \end{bmatrix} \tag{1.3}$$

where

$$\begin{aligned} I_{11} &= \int_{\mathcal{V}} \rho (x_2^2 + x_3^2)\, d\mathcal{V} & I_{12} &= -\int_{V} \rho x_1 x_2\, d\mathcal{V} \\ I_{22} &= \int_{\mathcal{V}} \rho (x_1^2 + x_3^2)\, d\mathcal{V} & I_{13} &= -\int_{V} \rho x_1 x_3\, d\mathcal{V} \\ I_{33} &= \int_{\mathcal{V}} \rho (x_1^2 + x_2^2)\, d\mathcal{V} & I_{23} &= -\int_{V} \rho x_2 x_3\, d\mathcal{V} \end{aligned} \tag{1.4}$$

in which $\mathcal{V}$ and ρ are, respectively, the body volume and mass density, whereas x_1, x_2 and x_3 are the components of $\bar{\boldsymbol{u}}$, that is the location of an arbitrary point with respect to the body reference frame (as denoted by the bar over the symbol). Thus, by making use of (1.1), Euler's equation with respect to the body centre of gravity can be expressed as follows:

$$\bar{\boldsymbol{I}}_{\theta\theta} \frac{D\bar{\boldsymbol{\omega}}}{Dt} = \bar{\boldsymbol{I}}_{\theta\theta} \frac{d\bar{\boldsymbol{\omega}}}{dt} + \bar{\boldsymbol{\omega}} \times (\bar{\boldsymbol{I}}_{\theta\theta} \bar{\boldsymbol{\omega}}) = \sum_k \bar{\boldsymbol{\tau}}_k \tag{1.5}$$

where $\bar{\boldsymbol{\omega}}$ is the angular velocity of the body defined in its coordinate system as well as the angular velocity of the moving reference frame by virtue of the fact that this frame of reference is rigidly connected to the body. Moreover, $\bar{\boldsymbol{\tau}}_k$ is the k-th moment acting on the body, which can be a pure moment or a moment of force.

Hence, (1.2) and (1.5) can be arranged in a matrix form, that is

$$\begin{bmatrix} m\boldsymbol{I} & \mathbf{0} \\ \mathbf{0} & \bar{\boldsymbol{I}}_{\theta\theta} \end{bmatrix} \begin{bmatrix} \dot{\boldsymbol{v}} \\ \dot{\bar{\boldsymbol{\omega}}} \end{bmatrix} + \begin{bmatrix} \mathbf{0} \\ \bar{\boldsymbol{\omega}} \times (\bar{\boldsymbol{I}}_{\theta\theta} \bar{\boldsymbol{\omega}}) \end{bmatrix} = \begin{bmatrix} \sum_k \boldsymbol{f}_k \\ \sum_k \bar{\boldsymbol{\tau}}_k \end{bmatrix} \tag{1.6}$$

in which $\boldsymbol{I}$ is the identity matrix and $\bar{\boldsymbol{\omega}} \times (\bar{\boldsymbol{I}}_{\theta\theta} \bar{\boldsymbol{\omega}})$ is the gyroscopic term; notice that the time derivatives are here indicated by $(\dot{\ })$ since there is no ambiguity.

Nevertheless, sometimes it is preferable to express also the speed $\boldsymbol{v}$ in Newton's equation (1.2) with respect to the body reference frame, similarly to the angular speed $\bar{\boldsymbol{\omega}}$ in Euler's equation. In this case, the matrix equation of motion becomes

$$\begin{bmatrix} m\boldsymbol{I} & \mathbf{0} \\ \mathbf{0} & \bar{\boldsymbol{I}}_{\theta\theta} \end{bmatrix} \begin{bmatrix} \dot{\bar{\boldsymbol{v}}} \\ \dot{\bar{\boldsymbol{\omega}}} \end{bmatrix} + \begin{bmatrix} \bar{\boldsymbol{\omega}} \times (m\bar{\boldsymbol{v}}) \\ \bar{\boldsymbol{\omega}} \times (\bar{\boldsymbol{I}}_{\theta\theta} \bar{\boldsymbol{\omega}}) \end{bmatrix} = \begin{bmatrix} \sum_k \bar{\boldsymbol{f}}_k \\ \sum_k \bar{\boldsymbol{\tau}}_k \end{bmatrix}. \tag{1.7}$$

1.2.2 Lagrange's equations of motion

Alternatively to Newton-Euler method, Lagrangian dynamics represents a very suitable approach to obtain the equations of motion. Different schemes may be carried out to derive the motion laws for the system; however, for general purpose simulators characterised by holonomic and/or nonholonomic constraints, a convenient technique is the so-called *augmented formulation* [44]. This approach makes use of redundant coordinates and Lagrange multipliers; as a consequence, every single body of the system is considered as a 6-DoF-entity subject to constraints, external forces and moments. Moreover, actual constraints reactions are functions of the Lagrange multipliers λ_j, $j = 1, 2, ..., n_c$, where n_c is the number of constrained DoFs.

As a result, the augmented formulation leads to the following equation

$$\frac{d}{dt}\left(\frac{\partial \mathscr{L}}{\partial \dot{\boldsymbol{q}}}\right) - \frac{\partial \mathscr{L}}{\partial \boldsymbol{q}} + \boldsymbol{\lambda}^T \boldsymbol{C}_{\boldsymbol{q}} = \boldsymbol{Q}_{nc}^T \tag{1.8}$$

where $\mathscr{L}$ is the Lagrangian function, that is

$$\mathscr{L} = \mathscr{T} - \mathscr{U} \tag{1.9}$$

in which $\mathscr{T}$ is the kinetic energy of the system and $\mathscr{U}$ is its potential energy. Moreover, $\boldsymbol{q}$ is the vector of generalised coordinates, $\boldsymbol{\lambda}$ is the vector of the Lagrange multipliers, $\boldsymbol{Q}_{nc}$ is the vector of nonconservative applied forces and moments and $\boldsymbol{C}_{\boldsymbol{q}}$ is the *system Jacobian* matrix. In particular, consider a set of holonomic constraints; its equations can be expressed in the form

$$\boldsymbol{C}(\boldsymbol{q}, t) = \mathbf{o} \tag{1.10}$$

By differentiating twice with respect to time t and by rearranging the terms, the following system can be obtained:

$$\boldsymbol{C}_{\boldsymbol{q}} \ddot{\boldsymbol{q}} = \boldsymbol{Q}_c. \tag{1.11}$$

Moreover, after performing the derivatives and rearranging its terms, (1.8) for the single i-th rigid body can be rewritten in the following form

$$\boldsymbol{M}^i \ddot{\boldsymbol{q}}_r^i + \boldsymbol{C}_{\boldsymbol{q}_r^i}^T \boldsymbol{\lambda} = \boldsymbol{Q}_e^i + \boldsymbol{Q}_v^i \tag{1.12}$$

where $\boldsymbol{M}^i$ is the inertia matrix; $\boldsymbol{C}_{\boldsymbol{q}_r^i}$ is the block of the system Jacobian corresponding to $\boldsymbol{q}_r^i$, that is the vector of reference coordinates of body i; $\boldsymbol{Q}_e^i$ is the vector of the externally applied forces and moments and $\boldsymbol{Q}_v^i$ is a quadratic velocity vector. More precisely, considering the special case in which the origin of the body reference frame is attached to its centre of mass, the inertia matrix is partitioned as follows:

$$\boldsymbol{M}^i = \begin{bmatrix} \boldsymbol{m}_{RR}^i & 0 \\ 0 & \boldsymbol{m}_{\theta\theta}^i \end{bmatrix} \tag{1.13}$$

in which $\boldsymbol{m}_{RR}^i$ is a diagonal matrix having the mass m of the i-th body as nonzero elements, that is

$$\boldsymbol{m}_{RR}^i = \begin{bmatrix} m^i & 0 & 0 \\ 0 & m^i & 0 \\ 0 & 0 & m^i \end{bmatrix} \tag{1.14}$$

and the rotational block is calculated as follows:

$$\boldsymbol{m}_{\theta\theta}^i = \bar{\boldsymbol{G}}^{i^T} \bar{\boldsymbol{I}}_{\theta\theta}^i \bar{\boldsymbol{G}}^i \tag{1.15}$$

where $\bar{\boldsymbol{I}}_{\theta\theta}^i$ is the inertia tensor of the i-th body expressed in the body coordinate system (see (1.3) and (1.4)) and $\bar{\boldsymbol{G}}^i$ is a proper transformation matrix, which depends on the formulation used to describe the orientation.

Thus, the vector of generalised reference coordinates for the i-th body is

$$\boldsymbol{q}_r^i = \begin{bmatrix} \boldsymbol{R}^{i^T} & \boldsymbol{\Theta}^{i^T} \end{bmatrix}^T \tag{1.16}$$

where $\boldsymbol{R}^i$ is the position vector of the centre of mass and $\boldsymbol{\Theta}^i$ is the vector of the rotational coordinates, which identify the orientation of the rigid body. Consequently, the angular velocity of the rigid body defined in its coordinate system is expressed as:

$$\bar{\boldsymbol{\omega}}^i = \bar{\boldsymbol{G}}^i \dot{\boldsymbol{\Theta}}^i. \tag{1.17}$$

Finally, the quadratic velocity vector can be calculated as follows:

$$\boldsymbol{Q}_v^i = \begin{bmatrix} \mathbf{o}^T & -2\bar{\boldsymbol{\omega}}^{i^T} \bar{\boldsymbol{I}}_{\theta\theta} \dot{\bar{\boldsymbol{G}}}^i \end{bmatrix}^T. \tag{1.18}$$

As already stated, $\bar{\boldsymbol{G}}^i$ depends on the formalism adopted to describe the orientation, which can be essentially based on Euler's angles or Euler's parameters. For instance, let ϕ^i be the rotation angle about the axis that is oriented as the unit vector $\boldsymbol{d}_i = [d_1^i \quad d_2^i \quad d_3^i]^T$; Euler's parameters

$$\theta_0^i = \cos\frac{\phi^i}{2}, \quad \theta_1^i = d_1^i \sin\frac{\phi^i}{2}, \quad \theta_2^i = d_2^i \sin\frac{\phi^i}{2}, \quad \theta_3^i = d_3^i \sin\frac{\phi^i}{2} \tag{1.19}$$

can be arranged to obtain a quaternion. As a consequence, using Euler's parameters, $\boldsymbol{\Theta}^i$ becomes

$$\boldsymbol{\Theta}^i = \begin{bmatrix} \theta_0^i & \theta_1^i & \theta_2^i & \theta_3^i \end{bmatrix}^T \tag{1.20}$$

and the transformation matrix $\bar{\boldsymbol{G}}^i$

$$\bar{\boldsymbol{G}}^i = 2 \begin{bmatrix} -\theta_1^i & \theta_0^i & \theta_3^i & -\theta_2^i \\ -\theta_2^i & -\theta_3^i & \theta_0^i & \theta_1^i \\ -\theta_3^i & \theta_2^i & -\theta_1^i & \theta_0^i \end{bmatrix} \tag{1.21}$$

It is appropriate to point out that unit quaternions represent a very suitable parametrisation for rotations by virtue of the absence of singularity and gimbal lock problems [45].

As for the generalised forces applied to the body, which contribute to create the vector $\boldsymbol{Q}_e^i$, they are calculated as

$$Q_{j,k}^i = \boldsymbol{f}_k^T \frac{\partial \boldsymbol{r}_k^i}{\partial q_j^i} \tag{1.22}$$

and

$$Q_{j,l}^i = \boldsymbol{\tau}_l^T \frac{\partial \boldsymbol{\omega}^i}{\partial \dot{q}_j^i} \tag{1.23}$$

where $\boldsymbol{r}_k^i$ is the position vector representing the application point of the k-th force $\boldsymbol{f}_k$; similarly, $\boldsymbol{\omega}^i$ is the angular velocity vector of i-th body defined in the global coordinate system and $\boldsymbol{\tau}_l$ is the l-th moment applied to the same body. In particular, let $\bar{\boldsymbol{u}}^i$ be the position vector expressed in the i-th body reference frame; let $\boldsymbol{f}_k$ be the k-th applied force; indicating with $\boldsymbol{A}^i$ the rotation matrix,

$$\boldsymbol{r}_k^i = \boldsymbol{R}^i + \boldsymbol{A}^i \bar{\boldsymbol{u}}^i \tag{1.24}$$

and

$$\boldsymbol{\omega}^i = \boldsymbol{G}^i \dot{\boldsymbol{\Theta}}^i \tag{1.25}$$

In turn, $\boldsymbol{A}^i$ can be calculated as follows

$$\boldsymbol{A}^i = \frac{1}{4} \boldsymbol{G}^i \bar{\boldsymbol{G}}^{iT} \tag{1.26}$$

where

$$\boldsymbol{G}^i = 2 \begin{bmatrix} -\theta_1^i & \theta_0^i & -\theta_3^i & \theta_2^i \\ -\theta_2^i & \theta_3^i & \theta_0^i & -\theta_1^i \\ -\theta_3^i & -\theta_2^i & \theta_1^i & \theta_0^i \end{bmatrix} \tag{1.27}$$

Consequently, the overall generalised force vector can be expressed as

$$\boldsymbol{Q}_e^i = \begin{bmatrix} \sum_{k=1}^{n_f^i} Q_{1,k}^i + \sum_{k=1}^{n_\tau^i} Q_{1,k}^i \\ \vdots \\ \sum_{k=1}^{n_f^i} Q_{n,k}^i + \sum_{k=1}^{n_\tau^i} Q_{n,k}^i \end{bmatrix} \tag{1.28}$$

where n, n_f^i and n_τ^i are, respectively, the number of generalised coordinates, applied forces and torques related to i-th body.

Furthermore, matrices $\boldsymbol{C_q}$ and $\boldsymbol{Q}_c$ can be pre-assembled for every fundamental constraint. By way of example, consider a spherical joint; its constraint equation, which translates the superposition of two points belonging to different bodies, is

$$\boldsymbol{R}' + \boldsymbol{A}'\bar{\boldsymbol{u}}' - \boldsymbol{R}'' - \boldsymbol{A}''\bar{\boldsymbol{u}}'' = \mathbf{0} \tag{1.29}$$

in which the superscripts $(')$ and $('')$ are used to indicate the quantities referring to the first and second body. Similarly, in addition to (1.29), the constraint equations for a revolute joint that allows the rotation about the axis oriented as the unit vector $\bar{\boldsymbol{s}}_\eta^i$ are

$$\begin{cases} (\boldsymbol{A}'\bar{\boldsymbol{s}}_\xi')^T(\boldsymbol{A}''\bar{\boldsymbol{s}}_\eta'') = 0 \\ (\boldsymbol{A}'\bar{\boldsymbol{s}}_\zeta')^T(\boldsymbol{A}''\bar{\boldsymbol{s}}_\eta'') = 0 \end{cases} \tag{1.30}$$

where $\{\bar{\boldsymbol{s}}_\xi^i, \bar{\boldsymbol{s}}_\eta^i, \bar{\boldsymbol{s}}_\zeta^i\}$ is the triad that identifies the joint orientation with respect to the i-th rigid body [46]. Thus, by deriving twice with respect to time (1.29), (1.30) or those corresponding to other constraints in the form of (1.10), the expression in (1.11) can be obtained, which incorporates all the constraints of the system. Considering a vehicle, joints such as those presented above can be found, for instance, between the bodies that constitute the suspensions and the steering assembly [41].

Afterwards, (1.12) can be written for each single body that composes the system; hence, these equations can be arranged as follows

$$\boldsymbol{M}\ddot{\boldsymbol{q}} + \boldsymbol{C}_{\boldsymbol{q}}^{T}\boldsymbol{\lambda} = \boldsymbol{Q}_e + \boldsymbol{Q}_v \tag{1.31}$$

in which

$$\boldsymbol{M} = \begin{bmatrix} \boldsymbol{M}^1 & & \mathbf{0} \\ & \ddots & \\ \mathbf{0} & & \boldsymbol{M}^{n_b} \end{bmatrix} \quad \boldsymbol{C}_{\boldsymbol{q}}^{T} = \begin{bmatrix} \boldsymbol{C}_{\boldsymbol{q}_r^1}^{T} \\ \vdots \\ \boldsymbol{C}_{\boldsymbol{q}_r^{n_b}}^{T} \end{bmatrix} \quad \boldsymbol{Q}_e = \begin{bmatrix} \boldsymbol{Q}_e^1 \\ \vdots \\ \boldsymbol{Q}_e^{n_b} \end{bmatrix} \quad \boldsymbol{Q}_v = \begin{bmatrix} \boldsymbol{Q}_v^1 \\ \vdots \\ \boldsymbol{Q}_v^{n_b} \end{bmatrix} \tag{1.32}$$

where n_b is the overall number of rigid bodies of the system.

Finally, it is possible to assemble (1.11) and (1.31) in order to obtain the fundamental system of differential-algebraic equations (DAE) that rules the motion of a multibody system:

$$\begin{bmatrix} \boldsymbol{M} & \boldsymbol{C}_{\boldsymbol{q}}^{T} \\ \boldsymbol{C}_{\boldsymbol{q}} & \mathbf{0} \end{bmatrix} \begin{bmatrix} \ddot{\boldsymbol{q}} \\ \boldsymbol{\lambda} \end{bmatrix} = \begin{bmatrix} \boldsymbol{Q}_e + \boldsymbol{Q}_v \\ \boldsymbol{Q}_c \end{bmatrix} \tag{1.33}$$

At this point, (1.33) obtaining the vector of the accelerations $\ddot{\boldsymbol{q}}$ and the one of the Lagrange multipliers $\boldsymbol{\lambda}$ is straightforward; the former can be integrated once to obtain the generalised velocities and twice for the generalised coordinates.

The equations presented so far have general validity for any dynamical system. As regards the special case of a vehicle, typically, such a system is made up of a rigid body representing the chassis, a set of bodies constituting the suspensions and the steering assemblies and four bodies for the wheels [41]. External applied forces of (1.12) are, essentially, due to the aerodynamic friction of the air acting on the chassis and to the rolling and sliding friction generated by the contact of the wheels on the ground [41].

1.2.3 Deformable bodies equations of motion

The fundamental concepts and modelling methods concerning deformable bodies are briefly presented in this section. More in-depth discussions on this subject can be found in [44] and [46].

Floating frame of reference formulation

This formulation, which is widely used in flexible multibody simulations, is based on the definition of a reference frame connected to each body of the system: the frame is utilised to determine the reference coordinates of the *i*-th body, that is $\boldsymbol{q}_r^i$ (see (1.16)), and the so-called flexible (or elastic) coordinates $\boldsymbol{q}_f^i$, which are employed to describe the deformation with respect to the body coordinate system. As a result, the vector of generalised coordinates can be partitioned as follows:

$$\boldsymbol{q}^i = \begin{bmatrix} \boldsymbol{q}_r^{i\,T} & \boldsymbol{q}_f^{i\,T} \end{bmatrix}^T \tag{1.34}$$

Essentially, the characterisation of the deformation field can be carried out by using classical approximation techniques such as Rayleigh-Ritz method and Galërkin method [47]; both make use of the truncated series to describe the displacement field of an arbitrary point belonging to a deformable body. Furthermore, the Rayleigh-Ritz method delineates the body deformation as a whole, whereas the finite-element method [48], which is based on Galërkin's formulation, describes the displacement by partitioning the body into elements. These small regions are interconnected to each other at the nodal points.

Thus, let $\boldsymbol{r}_P^i$ be the position vector on an arbitrary point *P* of *i*-th body; the Rayleigh-Ritz method leads to the following equation:

$$\boldsymbol{r}_P^i = \boldsymbol{R}^i + \boldsymbol{A}^i \bar{\boldsymbol{u}}^i = \boldsymbol{R}^i + \boldsymbol{A}^i(\bar{\boldsymbol{u}}_0^i + \boldsymbol{S}^i \boldsymbol{q}_f^i) \tag{1.35}$$

where $\boldsymbol{R}^i$ is the vector that identifies the location of the origin of the body reference frame, $\boldsymbol{A}^i$ is the transformation matrix describing the body orientation; $\bar{\boldsymbol{u}}^i$, that is the position vector of point *P* with respect to the body coordinate system, as indicated in (1.35), can be expressed as the sum of the undeformed position vector $\bar{\boldsymbol{u}}_0^i$ and of the term $\boldsymbol{S}^i\boldsymbol{q}_f^i$, in which $\boldsymbol{S}^i$ is the so-called shape function, that is the matrix conveying the deformation law for every point of the i-th body.

Subsequently, by differentiating (1.35) with respect to time, it is possible to calculate the kinetic energy T^i of body i:

$$T^i = \int_{\mathscr{V}^i} \rho^i \left(\dot{\boldsymbol{r}}^i\right)^T \dot{\boldsymbol{r}}^i \, d\mathscr{V}^i \tag{1.36}$$

where ρ^i is the density function and $\mathscr{V}^i$ is the body volume. Hence, thanks to (1.36), $\boldsymbol{M}^i$, i.e. the mass matrix of the deformable body i, can be determined. It is worth pointing out that this method employed to calculate $\boldsymbol{M}^i$ is the so-called *consistent mass formulation*; an alternative approach, the *lumped mass formulation*, consists in evaluating selected grid points by using shape vectors instead of shape functions.

Therefore, further calculations, which are omitted for the sake of brevity but which can be found in [44], lead to the following equations of motion for the deformable i-th body

$$\boldsymbol{M}^i\ddot{\boldsymbol{q}}^i + \boldsymbol{K}^i\boldsymbol{q}^i + \boldsymbol{C}_{\boldsymbol{q}^i}^T\boldsymbol{\lambda} = \boldsymbol{Q}_e^i + \boldsymbol{Q}_v^i \tag{1.37}$$

which alternatively may be written in the partitioned form

$$\begin{aligned} &\begin{bmatrix} \boldsymbol{m}_{RR}^i & \boldsymbol{m}_{R\theta}^i & \boldsymbol{m}_{Rf}^i \\ & \boldsymbol{m}_{\theta\theta}^i & \boldsymbol{m}_{\theta f}^i \\ sym. & & \boldsymbol{m}_{ff}^i \end{bmatrix} \begin{bmatrix} \ddot{\boldsymbol{R}}^i \\ \ddot{\boldsymbol{\Theta}}^i \\ \ddot{\boldsymbol{q}}_f^i \end{bmatrix} + \begin{bmatrix} \mathbf{0} & \mathbf{0} & \mathbf{0} \\ \mathbf{0} & \mathbf{0} & \mathbf{0} \\ \mathbf{0} & \mathbf{0} & \boldsymbol{K}_{ff}^i \end{bmatrix} \begin{bmatrix} \boldsymbol{R}^i \\ \boldsymbol{\Theta}^i \\ {\boldsymbol{q}_f}^i \end{bmatrix} \\ &+ \begin{bmatrix} \boldsymbol{C}_{\boldsymbol{R}^i}^T \\ \boldsymbol{C}_{\boldsymbol{\Theta}^i}^T \\ \boldsymbol{C}_{\boldsymbol{q}_f^i}^T \end{bmatrix} \boldsymbol{\lambda} = \begin{bmatrix} (\boldsymbol{Q}_e^i)_R \\ (\boldsymbol{Q}_e^i)_\theta \\ (\boldsymbol{Q}_e^i)_f \end{bmatrix} + \begin{bmatrix} (\boldsymbol{Q}_v^i)_R \\ (\boldsymbol{Q}_v^i)_\theta \\ (\boldsymbol{Q}_v^i)_f \end{bmatrix} \end{aligned} \tag{1.38}$$

Namely, $\boldsymbol{K}^i$ is the stiffness matrix, which can be calculated by exploiting the definition of strain energy; $\boldsymbol{C}_{\boldsymbol{q}^i}$ is the constraint Jacobian matrix; $\boldsymbol{\lambda}$ is the vector of Lagrange multipliers; $\boldsymbol{Q}_e^i$ is the vector of externally applied generalised forces; $\boldsymbol{Q}_v^i$ is a quadratic vector velocity.

Finally, by writing (1.37) (or (1.38)) for all the bodies that compose the system and by combining it with the second time derivative of the constraints equations, which is analogous to (1.11), the following matrix equation is obtained:

$$\begin{bmatrix} \boldsymbol{M} & \boldsymbol{C}_{\boldsymbol{q}}^{\boldsymbol{T}} \\ \boldsymbol{C}_{\boldsymbol{q}} & \mathbf{0} \end{bmatrix} \begin{bmatrix} \ddot{q} \\ \boldsymbol{\lambda} \end{bmatrix} = \begin{bmatrix} \boldsymbol{Q}_e + \boldsymbol{Q}_v - \boldsymbol{K}\boldsymbol{q} \\ \boldsymbol{Q}_c \end{bmatrix} \tag{1.39}$$

It is worth observing that (1.39) has the same form as (1.33).

Unfortunately, the determination of a suitable shape matrix, which is required by the Rayleigh-Ritz method, can be a difficult task, especially if the body has a complex geometry. In addition, the displacement field calculated by means of the Rayleigh-Ritz formulation typically requires adjustments before the use to fit the boundary conditions. In order to reduce these problems, the finite-element method can be adopted. Essentially, the finite-element technique can be considered as a particular case of the Rayleigh-Ritz method: the concept of shape function is applied to every single j-th element of i-th body according to the following equation

$$\boldsymbol{w}^{ij} = \boldsymbol{S}^{ij}\boldsymbol{e}^{ij} \tag{1.40}$$

where $\boldsymbol{w}^{ij}$ is the displacement field, $\boldsymbol{S}^{ij}$ is the element shape function and $\boldsymbol{e}^{ij}$ is the vector of nodal coordinates that represent displacements, slopes and curvatures of the nodal points.

Briefly, the mass and the stiffness matrices can be calculated for each element of the body; by summing up the former and the latter, the total mass and the total stiffness matrices of the single body are respectively obtained. Hence, these matrices can be substituted in (1.39).

The floating frame of reference formulation can be adopted to describe the dynamics of flexible components of a vehicle, provided that the deformations are relatively small. As an example, the technique is suitable to study the (relatively small) deformations of the suspensions assembly.

Absolute-nodal coordinate formulation

This formulation is an alternative technique to the classical floating frame of reference approach introduced above. Absolute-nodal coordinate formulation (ANCF) is useful to analyse the motion of systems of flexible bodies subject to arbitrary displacements, rotations and large deformations; notice that, in general, these conditions cannot be handled effectively neither through the traditional Rayleigh-Ritz formulation nor by means of the classical finite-element method.

As the name may suggest, the absolute-nodal coordinate formulation employs absolute displacements and slopes at the nodal point as the element nodal coordinates. Therefore, the absolute position vector $\boldsymbol{r}$ of a given point belonging to an element of the flexible body is calculated by means of the following equation:

$$\boldsymbol{r} = \boldsymbol{S}\boldsymbol{e} \tag{1.41}$$

where $\boldsymbol{S}$ is the global shape function and $\boldsymbol{e}$ is the vector of element nodal coordinates. Furthermore, after calculating the time derivative of (1.41), the kinetic energy of the element can be indicated as follows (see also (1.36)):

$$T = \frac{1}{2}\dot{\boldsymbol{e}}^T \boldsymbol{M_a} \dot{\boldsymbol{e}} \tag{1.42}$$

where $\boldsymbol{M_a}$ is the element mass matrix, which is defined as

$$\boldsymbol{M_a} = \int_V \rho \boldsymbol{S}^T \boldsymbol{S}\, dV \tag{1.43}$$

Moreover, the displacement of a generic point of the element with respect to the reference point O, which belongs to the same element, is defined as

$$\boldsymbol{u} = \boldsymbol{r} - \boldsymbol{r_O} = (\boldsymbol{S} - \boldsymbol{S_O})\boldsymbol{e} \tag{1.44}$$

where $\boldsymbol{r_O}$ is the position vector of the reference point O and $\boldsymbol{S_O}$ is the global shape function defined at the point O; notice that $\boldsymbol{u}$ is expressed in the global coordinate frame. Additionally, by isolating the stiffness matrix of the element $\boldsymbol{K_a}$, the strain energy of the finite element is

$$U = \frac{1}{2}\boldsymbol{e}^T \boldsymbol{K_a} \boldsymbol{e} \tag{1.45}$$

Essentially, by using an elastic model, the stiffness matrix of the element $\boldsymbol{K_a}$ can be determined.

Finally, the equation of motion of the single element can be expressed in the following form:

$$\boldsymbol{M_a}\ddot{\boldsymbol{e}}+\boldsymbol{K_a}\boldsymbol{e}=\boldsymbol{Q_a} \tag{1.46}$$

where $\boldsymbol{Q_a}$ is the vector of generalised nodal forces.

Since the ANCF is suitable to handle large deformation, it is indicated for the simulation of soft components such as tyres [49].

Mass-spring soft-body formulation

A quite peculiar approach used to describe the deformation of a body while retaining a relatively low computational load is the one implemented in Rigs of Rods (RoR) [42]. Basically, the system is described as a lattice of massless rods (beams) connecting nodes endowed with mass (material points); rods are free to deform along their main axis by the effect of internal and external forces, which are applied to the nodes.

The analytical core the mass-spring model (MSM) is built upon is rather straightforward [50]. Newton's second law for all the nodes of the systems assumes the form

$$\boldsymbol{M}\ddot{\boldsymbol{x}}=\boldsymbol{f}\left(\boldsymbol{x},\boldsymbol{v}\right) \tag{1.47}$$

where $\boldsymbol{M}$ is the $3n \times 3n$ diagonal mass matrix, in which n is the number of nodes that make up the system, and $\boldsymbol{f}$ is the vector of external and internal forces acting on the material points. By integrating (1.47), the states of each particle, namely the speed $\boldsymbol{v}=\dot{\boldsymbol{x}}$ and the position $\boldsymbol{x}$, are obtained. Also, the internal contribution of the overall nodal force exerted by j-th node on the i-th particle can be decomposed into the elastic force $\boldsymbol{f}_{e,ij}$ and the damping force $\boldsymbol{f}_{d,ij}$. Specifically,

$$\boldsymbol{f}_{e,ij}=k\left[\left|\boldsymbol{x}_{ij}\right|-l_{ij}\right]\frac{\boldsymbol{x}_{ij}}{\left|\boldsymbol{x}_{ij}\right|} \tag{1.48}$$

where k is the stiffness of the beam that connects the two particles, l_{ij} is its natural length and $\boldsymbol{x}_{ij}=\boldsymbol{x}_j-\boldsymbol{x}_i$ is the vector difference of the two ends of the beam;

$$\boldsymbol{f}_{d,ij}=c\left[\boldsymbol{v}_{ij}\cdot\frac{\boldsymbol{x}_{ij}}{\left|\boldsymbol{x}_{ij}\right|}\right]\frac{\boldsymbol{x}_{ij}}{\left|\boldsymbol{x}_{ij}\right|} \tag{1.49}$$

in which c is the damping constant. Note that the damping force is computed by projecting the speed vector difference $\boldsymbol{v}_{ij} = \boldsymbol{v}_j - \boldsymbol{v}_i$ onto the beam. Regarding the external contribution, it is mainly ascribable to gravity and friction.

It is worth pointing out that this lumped-parameter technique is essentially biased towards computational lightness rather than accuracy. Nevertheless, an accurate fitting of the mechanical properties of the lattice, namely mass distribution and rods stiffness and damping coefficients, may increase significantly the physical correctness of such method [51]. As a matter of fact, validated simulators which exploit this formulation for tyre dynamics description are already available [52].

1.3 Analytical vehicle models

1.3.1 Equations of motion of a planar vehicle model

Often, dynamic control algorithms rely on simple planar vehicle models. They can be employed to generate reference quantities required by the control itself. Moreover, in case of model predictive controls (MPC), they generally constitute the internal model, which predicts the states trajectories.

To derive the equations of motion, one may utilise the Newton-Euler formulation by making the assumption that the car can be described as a single rigid body which moves on a horizontal flat surface (see Fig. 1.1). Moreover, it may be helpful to express the speed $\boldsymbol{v}$ of the centre of mass with respect to the reference frame of the vehicle; in this case, $\boldsymbol{v}$ is as follows

$$\bar{\boldsymbol{v}} = V \cos\beta \, \boldsymbol{i}'_1 + V \sin\beta \, \boldsymbol{i}'_2 \tag{1.50}$$

where V is the magnitude of $\bar{\boldsymbol{v}}$, $\boldsymbol{i}'_1$ and $\boldsymbol{i}'_2$ are the unit vectors along the body frame axis and β is the sideslip angle of the vehicle (Fig. 1.1). Because the speed is expressed with respect to a moving frame of reference, as indicated in (1.1), its absolute time

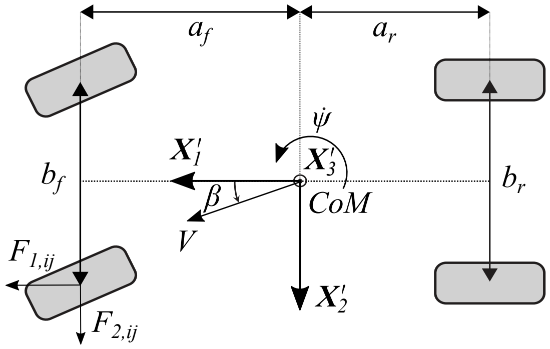

Figure 1.1: Planar vehicle model scheme. *CoM* is the acronym used to indicate the centre of mass.

derivative is

$$\begin{aligned}
&\frac{D\bar{\boldsymbol{v}}}{Dt} = \frac{d\bar{\boldsymbol{v}}}{dt} + \bar{\boldsymbol{\omega}} \times \bar{\boldsymbol{v}} \\
&\frac{d\bar{\boldsymbol{v}}}{dt} = (\dot{V}\cos\beta - V\dot{\beta}\sin\beta)\,\boldsymbol{i}'_1 + (\dot{V}\sin\beta + V\dot{\beta}\cos\beta)\,\boldsymbol{i}'_2 \\
&\bar{\boldsymbol{\omega}} \times \bar{\boldsymbol{v}} = -V\dot{\psi}\sin\beta\,\boldsymbol{i}'_1 + V\dot{\psi}\cos\beta\,\boldsymbol{i}'_2
\end{aligned} \tag{1.51}$$

where $\bar{\boldsymbol{\omega}} = \dot{\psi}\,\boldsymbol{i}'_3$ is the angular velocity of the vehicle. Therefore, by making use of (1.2), (1.5) and (1.51), the following scalar equations are obtained:

$$\begin{aligned}
\dot{V} &= \frac{1}{m}\left[\cos\beta\left(\sum_{i,j} F_{1,ij} - F_{drag}\right) + \sin\beta\left(\sum_{i,j} F_{2,ij}\right)\right] \\
\dot{\beta} &= \frac{1}{mV}\left[\cos\beta\left(\sum_{i,j} F_{2,ij}\right) - \sin\beta\left(\sum_{i,j} F_{1,ij} - F_{drag}\right)\right] - \dot{\psi} \\
\ddot{\psi} &= \frac{1}{I_{33}}\left[a_f(F_{2,fl} + F_{2,fr}) - a_r(F_{2,rl} + F_{2,rr})\right. \\
&\qquad \left. + \frac{b_f}{2}(F_{1,fr} - F_{1,fl}) + \frac{b_r}{2}(F_{1,rr} - F_{1,rl})\right]
\end{aligned} \tag{1.52}$$

where m is the total mass of the vehicle, I_{33} is the moment of inertia about the vertical axis (1.3); a_f and a_r are the distances between the centre of mass and, respectively, front and rear axle; b_f and b_r are, respectively, front and rear track; F_{drag} is the longitudinal resisting force; $F_{1,ij}$ and $F_{2,ij}$ are, respectively, longitudinal and lateral forces due to the ij-wheel with respect to the reference frame of the vehicle: the subscript i can be equal either to f (front) or to r (rear), whereas j can be equal either to l (left) or to r (right). Of course, these forces produced by the wheels may be calculated by means of a proper tyre model; Pacejka's Magic Formula is probably one of the most famous and widely used formulations [53, 54]. Finally, by combining (1.52) with four dynamic equations describing the rotation of the wheels about their main axis, a 7-DoF planar vehicle model is derived. Precisely, the ij-wheel rotational dynamics can be expressed by

$$J_{w,ij}\dot{\Omega}_{ij} = T_{ij} - F_{x,ij}R - M_{y,ij} \tag{1.53}$$

where $J_{w,ij}$ is the wheel moment of inertia, Ω_{ij} is the rotational velocity, T_{ij} is the wheel torque, $F_{x,ij}$ is the longitudinal force expressed in the wheel reference frame, R is the wheel radius, and $M_{y,ij}$ is the rolling resistance torque.

1.3.2 Equations of motion of a basic three-dimensional vehicle model

A basic three-dimensional model, which may be regarded as the immediate evolution of the planar model, is presented in this section. Also in this case, the vehicle is described as a single rigid body characterised by the barycentric reference system $\boldsymbol{X'_1}\boldsymbol{X'_2}\boldsymbol{X'_3}$: $\boldsymbol{X'_1}$ axis is forward, $\boldsymbol{X'_2}$ axis is towards the left side and $\boldsymbol{X'_3}$ axis is upward (Fig. 1.2). The speed of the centre of mass defined in the coordinate system of the car can be expressed in the following form:

$$\bar{\boldsymbol{v}} = V\cos\beta\cos\gamma\boldsymbol{i'_1} + V\sin\beta\cos\gamma\boldsymbol{i'_2} - V\sin\gamma\boldsymbol{i'_3} \tag{1.54}$$

where γ denotes the complementary polar angle and β is the azimuthal angle (Fig. 1.2), or, in vehicle terminology, sideslip angle. Moreover, the angular velocity defined in the reference frame of the vehicle is

$$\bar{\boldsymbol{\omega}} = \omega_1\,\boldsymbol{i'_1} + \omega_2\,\boldsymbol{i'_2} + \omega_3\,\boldsymbol{i'_3} \tag{1.55}$$

Thus, for the sake of compactness, let $\bar{\boldsymbol{F}} = [F_1\ F_2\ F_3]^T$ be the vector of the resultant force applied to the body defined in its coordinate system and let $\bar{\boldsymbol{M}} = [M_1\ M_2\ M_3]^T$

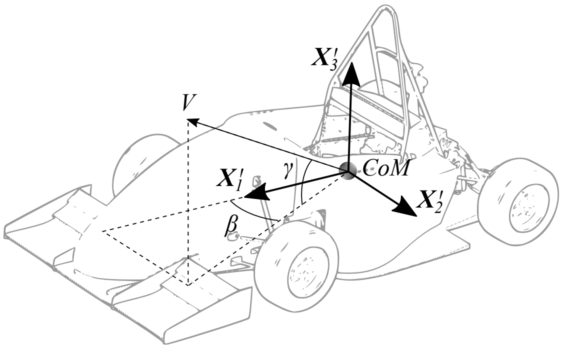

Figure 1.2: Single rigid body vehicle model scheme. The speed vector $\boldsymbol{v}$ makes an angle γ with its projection on the $\boldsymbol{X_1'X_2'}$ plane and the same projection makes an angle β with $\boldsymbol{X_1'}$ axis (commonly referred to as sideslip angle).

be the vector of the resultant moment; by performing time derivatives of (1.54) and of (1.55) and by employing (1.2) and (1.5), the following matrix equations are derived

$$\begin{aligned}
\begin{bmatrix} \dot{V} \\ \dot{\beta} \\ \dot{\gamma} \end{bmatrix} &= \boldsymbol{B}^{-1} \begin{bmatrix} V\omega_2 \sin\gamma + V\omega_3 \sin\beta\cos\gamma + \frac{F_1}{m} \\ -V\omega_1 \sin\gamma - V\omega_3 \cos\beta\cos\gamma + \frac{F_2}{m} \\ V\omega_1 \sin\beta\cos\gamma - V\omega_2\cos\beta\cos\gamma - \frac{F_3}{m} \end{bmatrix} \\
\begin{bmatrix} \dot{\omega}_1 \\ \dot{\omega}_2 \\ \dot{\omega}_3 \end{bmatrix} &= \bar{\boldsymbol{I}}_{\theta\theta}^{-1} \begin{bmatrix} (I_{22}-I_{33})\omega_2\omega_3 - I_{23}(\omega_2^2-\omega_3^2) - I_{13}\omega_1\omega_3 + I_{12}\omega_1\omega_3) + M_1 \\ (I_{33}-I_{11})\omega_1\omega_3 + I_{23}\omega_1\omega_2 + I_{13}(\omega_1^2-\omega_3^2) - I_{12}\omega_2\omega_3) + M_2 \\ (I_{11}-I_{22})\omega_1\omega_2 - I_{23}\omega_1\omega_3 + I_{13}\omega_2\omega_3 - I_{12}(\omega_1^2-\omega_2^2)) + M_3 \end{bmatrix}
\end{aligned} \tag{1.56}$$

where $\bar{\boldsymbol{I}}_{\theta\theta}$ is the inertia tensor (see (1.3)) and

$$\boldsymbol{B} = \begin{bmatrix} \cos\beta\cos\gamma & -v\sin\beta\cos\gamma & -v\cos\beta\sin\gamma \\ \sin\beta\cos\gamma & v\sin\beta\cos\gamma & -v\sin\beta\sin\gamma \\ \sin\gamma & 0 & v\cos\gamma \end{bmatrix} \tag{1.57}$$

Notice that (1.56) has the same form as (1.7).

An approximated approach consists in combining (1.56) with four equations that rule the rotation of the wheels about their main axis (see (1.53)), and with four equations describing the vertical motion of the unsprung masses, which can be expressed

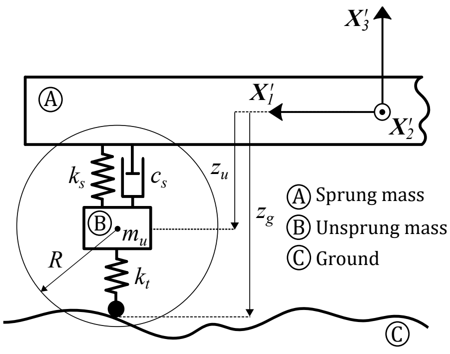

Figure 1.3: Approximated model representing the vertical dynamics of the unsprung mass relative to the sprung one.

as lumped entities connected to the vehicle body through elastic and damping forces. Therefore, considering the ij-corner, let $z_{u,ij}$ be the vertical displacement of the lumped unsprung mass $m_{u,ij}$; $z_{g,ij}$ the vertical displacement of the tyre point of contact on the ground; $l_{s,ij}$ the natural length of the suspension; $k_{s,ij}$ the suspension stiffness; $c_{s,ij}$ the suspension damping factor; $k_{t,ij}$ the tyre stiffness; $F_{s,ij}$ the total force given by the weight of the unsprung mass, by anti-roll bars and by actuators, if any. The vertical dynamics of the unsprung mass relative to the sprung one is given by

$$m_{u,ij}\ddot{z}_{u,ij} = -k_{s,ij}(z_{u,ij} + l_{s,ij}) - c_{s,ij}\dot{z}_{u,ij} - k_{t,ij}(z_{u,ij} - z_{g,ij} - R) + F_{s,ij} \tag{1.58}$$

Note that all the displacements in (1.58) are expressed with respect to the barycentric reference system of the vehicle body (Fig. 1.3). Overall, the equations (1.53) and (1.56), together with the dynamic equations of the unsprung masses (1.58), define a 14-DoF three-dimensional wheeled vehicle model. Such a model, despite the inherent limitations and approximations [55], is suitable for fast and thorough simulation of vehicles equipped with elastic suspensions, whether they are passive or active. In addition, the model in question can be useful in the presence of relatively large unsprung masses because it allows assessing their effects on tyre slips and handling: this can be the case of in-wheel-motor (IWM) electric vehicles.

Finally, it is worth observing that, by virtue of the three-dimensional description of motion, the formulation introduced in this section may be employed to simulate not only wheeled vehicles but also, for instance, aircrafts such as unmanned aerial vehicles (UAV) [56].

1.4 Mass-spring soft-body model fitting

Parameter translation and fitting play a significant role in connection with mass-spring model formulation. Indeed, the accuracy of a simulation based on this discrete approach is bonded inseparably to the identification of the beam parameters. After all, MSM technique, unlike, for instance, Finite Element Method (FEM) for structural analysis, lacks elastic theory as a foundation [50], which means that there is no clear physical connection between the target system (i.e. vehicle component to be replicated) and the MSM-based counterpart.

Within the context of this study, the identification process is achieved by means of a unique simulator based on the mass-spring model equations: this can be regarded with full rights as the fundamental tool for an attentive and methodical creation of the vehicle model and its subsystems, namely, chassis, suspensions and tyres. It is worth observing that, among other things, one of the main advantages deriving from the aforementioned implementation of the mass-spring model is the fact that a bare code containing only the essential elements may be easily generated and embedded in a real-time model predictive control.

When dealing with MSM, firstly, it is essential to place the nodes to meet the inertial requirements (i.e. mass distribution) and to assign suitable properties to the beams for obtaining the desired overall deformation of the vehicle components.

Certainly, tyre demands special attention during the aforementioned identification because, ultimately, it is largely responsible for vehicle behaviour; therefore, it is a crucial component for the development of an effective and reliable dynamic control. A lattice that provides an interesting trade-off between dynamic response faithfulness and computational load is the scheme displayed in Fig. 1.4. It is made of a set of radial beams which connect the tread band to the hub; a set of diagonal reinforcements contribute to the ultimate loading capacity of the tyre in case of lateral forces.

The interaction between tyre and ground relies on a collision model according

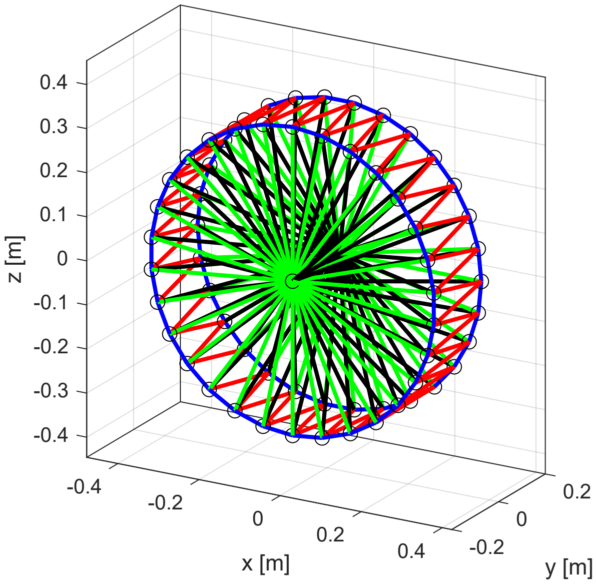

Figure 1.4: The tyre lattice in a Cartesian reference space. Beams are coloured based on their structural function: edge beams in blue, radial beams in green, tread beams in red and diagonal reinforcements in black. Nodes are circled.

to which the constraint reactions exerted by the terrain are applied to all the nodes which are touching the soil. Essentially, the contact produces the ground normal forces based on the sinkage of the node and on its normal approaching speed. Instead, the tangential speed of the node, that is the sliding velocity, is related to the friction force. The body contact is generally distributed over a set of nodes, which constitutes a more realistic representation than those offered by other physical or empirical models in which the contact is punctual, especially if the surface is uneven. Moreover, an interesting consequence descending from this approach is the fact that the rolling friction emerges spontaneously thanks to the asymmetric pressure distribution that arises on the nodes belonging to the contact patch.

First, to assign the stiffness and the damping values to the beams as a function of their structural purpose, these are classified into families: radial, edge, tread band and reinforcements. Moreover, Pacejka Magic Formula [57],[53] is assumed as the reference tyre model. Longitudinal and lateral forces produced by the interaction between the mass-spring tyre and the ground are compared with those provided by Pacejka's formulation, for a given vertical load, as a function of the longitudinal slip σ and of the lateral slip angle α. In addition, the test that is executed to assess the adherence to the reference model of the soft-body tyre for a given set of parameters is basically a virtual reproduction of the experiments which are performed in the real world to characterise an actual tyre. The wheel is fixed to a support that imposes the desired vertical load and sideslip angle; this support is also equipped with sensors (or special beams) for measuring the reactions exerted by the tyre. Hence, the wheel is pulled while a driving torque profile is applied: this procedure allows estimating the tyre forces for a wide range of values of the longitudinal slip.

1.5 Simulations

A set of simulations is performed to compare the different approaches oriented to vehicle dynamics description. To this end, the same vehicle is replicated through the different formulations presented above.

The multibody simulator that is selected to assemble the vehicle is Project Chrono (or, more briefly, Chrono) [49], an open source multi-physics simulation engine which supplies also a valid and reliable vehicle module. As regards the mass-spring soft-body implementation, Rigs of Rods (RoR) is the adopted simulator, albeit the model configuration is performed through a unique implementation. In the soft-physics-based vehicle model the Ackermann steering geometry is not implemented for simplicity purposes (though no inherent limitation of this formulation prevents from assembling this steering scheme). This choice may yield additional slip and traction loss in some conditions compared to the other models. Nonetheless, effects due to the lack of Ackermann geometry are generally negligible, especially if the steering angles are small. The mass distribution over the nodes of the vehicle chassis and suspensions is displayed in Fig. 1.5. Furthermore, to honour as much as possible the agreement between all the vehicle models, owing to the high mass of the wheels supports of the MSM model, the mass of the wheels of the analytical and multibody reproduction is

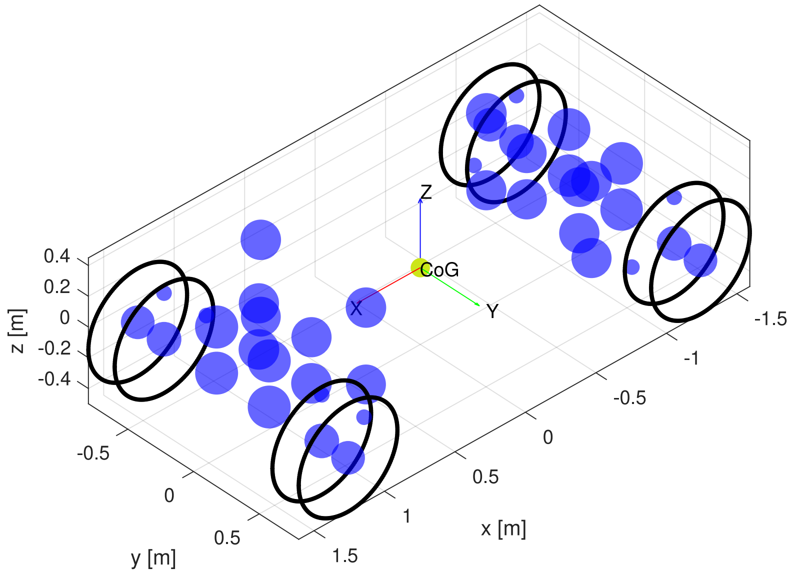

Figure 1.5: Mass distribution over the nodes of the chassis and suspensions for the mass-spring vehicle model. Circle size is representative of the magnitude of the corresponding node mass.

increased accordingly.

Moreover, the analytical models, i.e. the planar one (see Section 1.3.1) and the basic three-dimensional one (see Section 1.3.2), are developed in MATLAB environment. In the remainder of this study, the former will be also referred to as *Analytical 2D*, the latter as *Analytical 3D*.

To assess the validity of the different approaches, CarSim simulator is assumed as the reference implementation. Briefly, this commercial simulator is based on the multibody formalism. Every subsystem is also faithfully described through maps and plenty of experimental data; for instance, suspensions are characterised by means of kinematic and compliance (K&C) tests. Further, CarSim offers several tyre models, including Pacejka 5.2 version (the one selected for the present comparison) and FTire

Table 1.1: Tested simulators comparison.

Simulator	Formulation	Language	Time integrator	Integration step size
Chrono	multibody	C++	linearised implicit Euler	1 ms
RoR	mass-spring	C++	semi-implicit Euler	500 µs
Analyt. 3D	single body	MATLAB	NDF, order 1 to 5	variable
Analyt. 2D	single body	MATLAB	BDF (Gear), order 1 to 5	variable
CarSim	multibody	Lisp	Adams-Bashforth 2$^{\text{nd}}$ Order	500 µs

Table 1.2: Fundamental parameters of the vehicle model.

Description	Value	UoM
Vehicle mass	1093	kg
Wheel mass	72	kg
Wheel radius	0.35	m
Wheel inertia	2.45	$\mathrm{kg\,m^2}$
Wheelbase	2.5	m
Track	1.4	m
Maximum motor torque	365	Nm

[52].

Some additional features of the simulators embraced for this analysis are summarised in Table 1.1. Besides, Table 1.2 encloses the main parameters of the simulated vehicle model.

In the context of the present analysis, the accuracy of a specific vehicle implementation is assessed by comparing the errors of a given model reproduction with those produced by CarSim: ideally, a reliable model generates errors which are close to those provided by CarSim, the reference simulator [58, 59, 60, 61, 62]. Therefore, a set of performance indices are selected to carry out the comparison. Namely, mean and root mean square (RMS) of the speed error are useful to quantify the overall discrepancy of the actual vehicle speed relative to the set point. Similarly, maximum, mean and RMS of the displacement error are considered to assess the deviation of the centre of gravity relative to the ideal trajectory.

1.5.1 Path-follower driver

An honest comparison between the four models also imposes that the driver is the same for all the vehicle implementations. For this reason, a single driver model is developed in MATLAB. Specifically, it is based on a path follower algorithm which receives the lateral distance of the vehicle from the target trajectory, and produces a steering output through a proportional-integral (PI) controller with an anti-windup scheme based on a back-calculation algorithm. Moreover, the throttle command is managed by another PI controller, with the purpose of minimising the error between the attained vehicle speed and the reference one. Regarding Project Chrono and RoR, data swapping between the vehicle and the pilot is entrusted to a TCP-based network socket.

The closed-loop steering control is such that the lateral distance from the reference trajectory is measured ahead of the vehicle, which provides an implicit prediction component in the control response: this improves its stability in the presence of abrupt changes in the path curvature.

In addition, three significant manoeuvres are identified to highlight the peculiar features of each approach. The first one is a variant of the standardised double lane change, also known as elk test or moose test. The second one consists in a circular target trajectory that is travelled at constant and relatively high speed. The final trial is a slalom. Accordingly, the most significant results are reported in aggregate form and discussed in the following.

With respect to the double lane change manoeuvre, all the vehicle implementations describe a trajectory that is acceptably close to the target (Fig. 1.6). The most noticeable discrepancies can be observed in correspondence of the first realignment with the side lane: CarSim depicts a slightly wider and delayed trajectory than those of the other simulators. Ultimately, as demonstrated by the results reported in Table 1.3, there exists good agreement among all the models.

The circular path is travelled quite smoothly by all the models throughout the 30 s

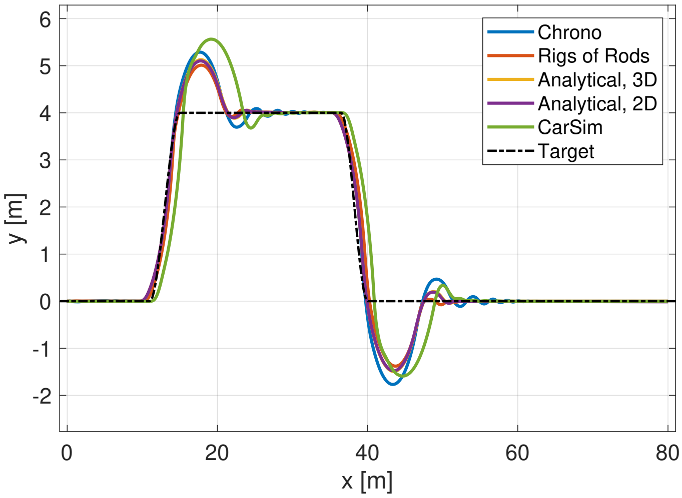

Figure 1.6: Resultant trajectories of the distinct vehicle implementations with respect to the double lane change manoeuvre. Notice that the curves corresponding to the two analytical models are essentially superposed.

of the test (Fig. 1.7). However, Table 1.4 reveals some drawbacks of the soft-body simulation. In fact, the results produced by Rigs of Rods are affected by a numerical issue which provokes physically-inexplicable accelerations while turning. In this scenario the problem is more apparent due to the constant curvature of the path; as a consequence, the cruise speed of the MSM-based model is lower than that of the other implementations. Nevertheless, this issue does not compromise the overall vehicle behaviour and it does not question the validity of the soft-body formulation oriented to vehicle simulation. Regarding CarSim results, peak yaw rates and peak lateral accelerations are higher than those recorded for the other simulators: this response is imputable to a sudden traction loss immediately after the start from standstill. Finally, as regards the displacement error from the reference path, little differences between the analytical models and the multibody models (i.e. Chrono and CarSim) can be appreciated; this result is due to a more prone-to-oscillation behaviour exhibited by the two multibody simulators.

Table 1.3: Double lane change manoeuvre: results of the simulations.

		Chrono		**Rigs of Rods**		**Analytical, 3D**		**Analytical, 2D**		**CarSim**	
Quantity	UoM	value	time [s]	value	time [s]	value	time [s]	value	time [s]	value	time [s]
Yaw max	deg	56.85	4.43	57.99	5.31	54.19	4.58	54.07	4.57	51.98	4.94
Yaw min	deg	-59.90	11.65	-58.28	13.04	-56.59	11.71	-56.53	11.69	-52.24	11.91
Yaw rate max	deg/s	49.97	13.65	40.20	7.82	44.07	13.65	44.10	13.62	45.11	12.23
Yaw rate min	deg/s	-49.98	11.42	-52.09	12.88	-44.00	11.48	-44.03	11.46	-45.25	5.26
Lat. acc. max	m/s^2	7.52	3.13	7.80	16.80	5.31	3.31	5.38	3.30	5.27	12.07
Lat. acc. min	m/s^2	-7.43	10.29	-6.46	8.29	-5.24	10.39	-5.36	10.37	-5.29	5.10
Speed err. mean	km/h	-0.47	—	-1.83	—	-0.62	—	-0.63	—	-0.48	—
Speed err. RMS	km/h	1.70	—	3.00	—	2.00	—	1.99	—	1.88	—
Displ. err. max	m	1.86	—	1.44	—	1.55	—	1.54	—	1.75	—
Displ. err. mean	m	0.26	—	0.22	—	0.20	—	0.20	—	0.39	—
Displ. err. RMS	m	0.54	—	0.44	—	0.44	—	0.44	—	0.70	—

Also the sinusoidal trajectory is described almost flawlessly by all the vehicles, except some imperfections caused by the aforementioned numerical issue that affects the soft-body simulator (Fig. 1.8). Finally, the remarks expressed for the previous tests are still valid and are useful to interpret the results reported in Table 1.5.

1.5.2 Remarks on computational time

A further index of performance is the computational time, i.e. the duration of a simulation. This value provides a measure of the efficiency of a formulation and supplies an indication of its *real-time readiness* with a view to model-based dynamic control implementations.

In order to give an indicator of the computational cost, the average duration of the double lane change test simulation for each piece of software is reported in Table 1.6. The target machine is equipped with an Intel(R) Core(TM) i7-4510U CPU @ 2 GHz. It is worth pointing out that there exist many dissimilarities between the simulators. The differences are not only related to the adopted mathematical formulation (the only aspect analysed in the comparison so far) but are also connected to the implementation of the simulators themselves. Absolutely, also the latter category can affect significantly the performance of the piece of software. More precisely, in the context of this

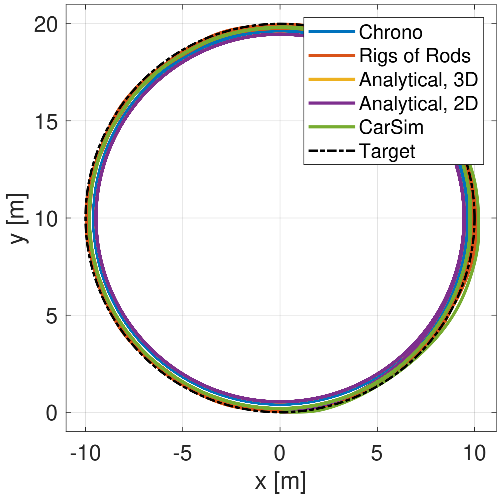

Figure 1.7: Resultant trajectories of the distinct vehicle implementations with respect to the circular-path manoeuvre. No substantial differences between the curves can be observed.

review, Chrono, RoR and CarSim are interfaced with the MATLAB/Simulink environment through a network socket. This is detrimental for the overall computational time because of the communication overhead. Moreover, Chrono and RoR physical simulations are executed in parallel with the graphical rendering. Further, both the analytical models are coupled with a variable-step solver and are executed within the MATLAB environment (neither MEX files nor code generation is exploited). Nevertheless, these results show that the effort needed to configure and properly customise the simulators to meet the real-time constraint is radically different and deeply rooted into the inherent modelling formulation adopted. Real-time readiness is a crucial feature since it permits to embed the vehicle model inside a real-time dynamics controller, thus empowering control validation and supporting model-based techniques.

Table 1.4: Circular-path manoeuvre: results of the simulations.

		Chrono		**Rigs of Rods**		**Analytical, 3D**		**Analytical, 2D**		**CarSim**	
Quantity	UoM	value	time [s]	value	time [s]	value	time [s]	value	time [s]	value	time [s]
Yaw max	deg	1290.03	30.00	996.98	29.89	1300.01	30.00	1301.09	30.00	1253.65	30.00
Yaw min	deg	-0.01	0.08	-0.04	0.37	-0.00	0.08	-0.00	0.01	-0.01	0.04
Yaw rate max	deg/s	45.27	4.18	57.06	2.73	45.43	29.99	45.46	25.91	64.12	2.10
Yaw rate min	deg/s	-0.03	0.08	-0.08	0.37	-0.00	0.08	-0.00	0.01	-3.27	0.48
Lat. acc. max	m/s^2	6.38	5.95	6.62	21.23	5.91	29.81	5.93	23.82	8.08	3.71
Lat. acc. min	m/s^2	-0.03	0.09	-6.44	26.59	-0.00	0.05	-0.00	0.07	-1.15	4.01
Speed err. mean	km/h	-0.96	—	-6.85	—	-1.07	—	-1.05	—	-1.23	—
Speed err. RMS	km/h	3.92	—	7.48	—	4.35	—	4.34	—	4.18	—
Displ. err. max	m	0.42	—	0.25	—	0.54	—	0.54	—	0.30	—
Displ. err. mean	m	0.38	—	0.10	—	0.51	—	0.51	—	0.18	—
Displ. err. RMS	m	0.39	—	0.13	—	0.52	—	0.52	—	0.19	—

1.6 Conclusion

In conclusion, the present analysis demonstrates that, despite the inherent dissimilarities between the formulations discussed herein, all the different techniques can be adopted to simulate with acceptable accuracy the dynamic response of a vehicle system. In addition, if the ultimate purpose of the simulation is the development of dynamic controls for, possibly, electric and hybrid vehicles, even the most essential representation, that is, the planar model, provides satisfactory performance in a wide range of conditions.

Regarding the mass-spring soft-body formulation, despite the venial limitations of the simulator that was adopted for the comparison, this technique is very powerful, and is indicated especially for the development of tyre models for manoeuvres on arbitrary and possibly rough terrain.

To sum up, the most suitable modelling technique for vehicle dynamics simulation and control development can be chosen by following the next guidelines and recommendations.

- Multibody is the most accurate and powerful formulation; if based essentially on rigid body dynamics, it is also numerically favourable to the point of being suitable even for real-time applications such as hardware-in-the-loop (HIL) or

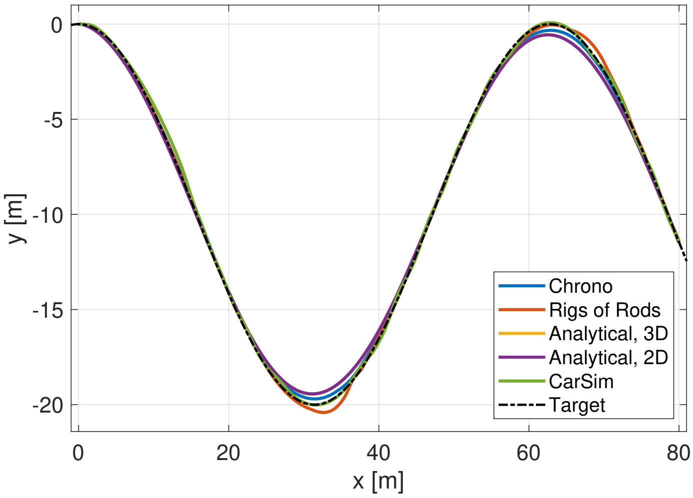

Figure 1.8: Resultant trajectories of the distinct vehicle implementations with respect to the slalom manoeuvre. Note that the curves corresponding to the two analytical models are essentially superposed.

human-in-the-loop simulations. However, it is generally too expensive for being the foundation of the internal model of implicit MPCs or state observers. As a matter of fact, multibody constitutes the mathematical core of the majority of high-fidelity vehicle simulators.

- For extremely faithful though computationally-taxing simulations, multibody can be coupled with a FEM formulation in order to describe systems made also of flexible components. As a consequence, this method is generally used to validate reduced models. A typical approach consists in simulating tyres by means of ANCF.

- Ultimately, a single rigid body model shares the fundamental equations of motion with the multibody technique, hence its mathematical basis is sound and unquestioned. This makes a single three-dimensional rigid body analytical model a useful tool for fast, lightweight and relatively accurate simulation of

Table 1.5: Slalom manoeuvre: results of the simulations.

		Chrono		**Rigs of Rods**		**Analytical, 3D**		**Analytical, 2D**		**CarSim**	
Quantity	UoM	value	time [s]	value	time [s]	value	time [s]	value	time [s]	value	time [s]
Yaw max	deg	46.23	7.65	44.52	9.99	43.70	7.84	43.69	7.83	47.80	7.72
Yaw min	deg	-47.10	3.25	-49.24	13.38	-43.91	3.65	-43.90	3.64	-62.33	2.92
Yaw rate max	deg/s	56.07	5.63	89.39	5.67	47.27	5.60	47.18	5.60	64.47	6.22
Yaw rate min	deg/s	-54.37	10.18	-70.39	12.48	-47.26	9.75	-47.25	9.73	-67.07	10.53
Lat. acc. max	m/s^2	11.98	5.35	8.75	7.43	7.41	5.51	7.40	5.55	8.00	6.20
Lat. acc. min	m/s^2	-9.42	9.44	-8.14	12.92	-7.41	9.66	-7.41	9.66	-8.38	10.82
Speed err. mean	km/h	-3.16	—	-9.19	—	-3.63	—	-3.61	—	-3.96	—
Speed err. RMS	km/h	8.02	—	11.69	—	9.01	—	9.00	—	8.59	—
Displ. err. max	m	0.33	—	0.57	—	0.59	—	0.59	—	0.42	—
Displ. err. mean	m	0.12	—	0.10	—	0.22	—	0.22	—	0.09	—
Displ. err. RMS	m	0.14	—	0.16	—	0.29	—	0.29	—	0.13	—

vehicles, provided that it is coupled with a reliable tyre model. It can also be used in the context of dynamic control development in case of non-planar motion of the vehicle.

- Torque allocation algorithm and similar control strategies can be effectively developed by taking advantage of a simple single rigid body planar model, provided that the vehicle motion is essentially flat. Generally, this representation constitutes the internal model of MPCs or state observers oriented to vehicle dynamics control.

- Mass-spring soft-body physics lends itself also to advanced automotive simulations, though attentive parameter fitting is needed. A very suitable application of this modelling technique consists in simulating deformable tyres over rough terrains by virtue of the favourable trade-off between accuracy and computational load. Real-time constraint can be easily met without renouncing appreciably to the quality of the results. Mass-spring formulation is also indicated for vehicle simulation in extreme scenarios. In addition, the inherently distributed contact model provided by the mass-spring model combined with proper collision detection algorithms may represent a powerful package for the simulation of a vehicle over pebbly, rocky or granular soils.

Table 1.6: Computing time for the tested simulators. Real-time (RT) factor lower than one means that the simulation runs faster than real time. See text for notes about measuring conditions (graphics, driver communication, . . .).

	Simulated time [s]	Real time [s]	RT factor
Chrono	22.17	141	6.4
RoR	24.65	274	11.1
Analyt. 3D	22.17	59	2.7
Analyt. 2D	22.17	17	0.8
CarSim	21.76	27	1.2

The general guidelines are integrated with additional information in Table 1.7.

Table 1.7: Guidelines for the choice of the formulation and the corresponding vehicle simulator. Note that the list of simulators is not complete.

Formulation	**Simulators**	**Accuracy**	**Real-time readiness**	**Applications**
Multibody based only on rigid-body mechanics	• Project Chrono [49] • CarSim [58] • Adams [63] • SIMPACK [64] • CarMaker [65] • MBDyn [66] • Bullet Physics [67] • Open Dynamics Engine [68]	High	Medium to high	• Design of vehicle subsystems [69] • Lower-order model validation [70, 71] • Dynamics control development and virtual validation [72, 73, 74] • Reference model for advanced MPCs or observers [75] • HIL simulation [76, 77] • HITL simulation [78] • Autonomous driving research [79, 80, 81]
Multibody (partly) based on deformable body mechanics (FEM)	• Project Chrono • Adams • SIMPACK • MBDyn	Very high	Low	• Lower-order model validation • Optimisation of vehicle components and subsystems [82] • Vehicle simulation with rough and granular terrain with FEM tyre models [83]
Single rigid body, three-dimensional	One's own implementation	Low to medium	Very high	• Dynamics control development [84] • Internal model of MPCs and observers
Single rigid body, planar	One's own implementation	Low	Very high	• Dynamics control development [85] • Internal model of MPCs and observers [86]
Mass-spring soft-body physics	• Rigs of Rods [42] • BeamNG.drive [43] • FTire (tyre simulation) [52]	Low to high	Medium to high	• Fast simulation of flexible components, especially tyres • Vehicle crash test simulation [43, 42] • Fast development of algorithms for extreme scenarios possibly over rough terrains [87] • Coupling of mass-spring tyre model with multibody vehicle model [88, 89]

Chapter 2

Energy-efficiency of multi-actuated electric vehicles

2.1 Introduction

The vehicle industry's continuous shift to electrification has resulted in an estimated 7.2 million electric vehicles being in circulation today, 2.1 million of which were sold in 2019 alone [1]. The significant cost of batteries and limited autonomy associated with electric vehicles has motivated the development of energy management systems that minimise power consumption across a range of vehicle operating conditions. Many proposed implementations of such systems have featured electrified actuators such as in-wheel motors (IWM), active tie-rods and force actuators in order to capture the benefits of actuation redundancies. For instance, electric vehicles with independent in-wheel or on-board motors allow for the asymmetrical distribution of driving and braking torques across each side of the vehicle, commonly referred to as torque vectoring (TV). The enhancements to vehicle handling and safety achievable through TV control are widely documented in the literature [90, 19, 91, 92, 93, 94], as is its influence on sources of significant power consumption such as tyre slip dissipations and losses in the electric drivetrain [95, 96]. A number of works have catered to the latter two aspects by proposing energy efficient control allocation strategies that incorporate electric motor efficiency [97, 98, 99, 100, 101, 102, 103] or minimise lateral, longitudinal tyre slips and tyre workload [104, 105, 106, 107]. In [25, 26], the authors present experiments demonstrating greater energy savings obtained from TV control imposing an appropriate reference understeer characteristic than an energy-efficient control allocation algorithm, albeit at the consequence of influencing handling behaviour.

Rear-wheel steering (RWS) control as a mechanism to improve vehicle handling and stability in lateral motions is discussed at length in the literature, both as a single actuation [108, 109] as well as integrated with yaw moment control [110, 111, 27]. With the exception of [27], these studies do not present any energy efficiency considerations. However, [112] shows significant energy savings in a cornering manoeuvre when rear-wheel steering angles are derived around minimisation of tyre slip power losses.

Active suspension (AS) control implemented via individual actuators or active anti-roll bars has been demonstrated in [113, 114, 115, 116, 117, 118] to improve vehicle ride quality, noise isolation and cornering response. From an energy efficiency viewpoint, [30, 119, 120] propose methods of reducing power consumption via the recovery of energy dissipations within the active suspension actuation system itself, but do not indicate subsequent implications to vehicle handling.

The handling authority of the three aforementioned actuation systems, individually and in tandem, is also covered in depth in [20, 121, 122], yet no energy consumption analysis is presented.

Therefore, there is a knowledge gap concerning the analysis of the energy-saving capabilities of a multiple actuation system comprising torque vectoring, rear-wheel steering and active suspension. In particular, the generation of an energy efficient reference understeer characteristic, as proposed in [25, 26], has yet to be tested for different cornering conditions such as velocity, adherence and longitudinal acceleration.

Accordingly, the points addressed by the present investigation:

- systematic evaluation of the energy saving potentialities deriving from the most established actuations that can be exploited on a fully electric vehicle, namely, torque vectoring, rear-wheel steering, active suspensions;

- assessment of the benefits of an active longitudinal torque distribution compared to a static allotment for a given active yaw moment;
- determination of the most efficient understeer characteristic based on the available actuations and for different test conditions involving speed, adherence and powertrain workload;
- definition of an optimal control allocation for achieving a desired understeer characteristic based on energy efficiency criteria.

2.2 Analytical background

The present study is mostly based on an extensive set of simulations. The approach is sustained by the fact that, in general, the analytical solution of the energy-efficient control allocation problem cannot be obtained effortlessly through elementary vehicle models. However, for some simple cases, an approximate analysis can be carried out. For instance, by exploiting a stationary single-track vehicle model as the one depicted in Fig. 2.1, the following equations of motion are obtained:

$$\begin{cases} ma_y = -C_f\alpha_f - C_r\alpha_r & \text{(2.1a)} \\ 0 = -C_f\alpha_f a_f + C_r\alpha_r a_r + M_z & \text{(2.1b)} \end{cases}$$

where C_f and C_r are the cornering stiffnesses of front and rear axles, α_f and α_r are the sideslip angles of the two axles, a_f and a_r are the distances between the centre of gravity and, respectively, front and rear axles, m is the total mass, a_y is the lateral acceleration and M_z is the active yaw moment. It is immediate to derive the expressions of the sideslip angles:

$$\alpha_f = -\frac{ma_y a_r}{C_f\left(a_f + a_r\right)} + \frac{M_z}{C_f\left(a_f + a_r\right)} \tag{2.2a}$$

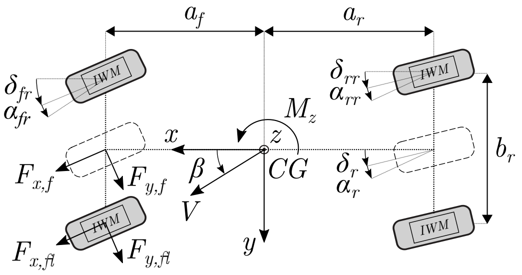

Figure 2.1: Vehicle schematic. A single-track vehicle model (indicated by dashed lines) is superposed to a schematic of a four-wheeled vehicle equipped with four in-wheel-motors.

$$\alpha_r = -\frac{m a_y a_f}{C_r\left(a_f + a_r\right)} - \frac{M_z}{C_r\left(a_f + a_r\right)} \tag{2.2b}$$

Accordingly, let the lateral tyre forces $F_{y,f}$ and $F_{y,r}$ of front and rear axles be

$$F_{y,f} = -C_f \alpha_f \tag{2.3a}$$

and

$$F_{y,r} = -C_r \alpha_r \tag{2.3b}$$

Also, let $v_{y,slip,f} = V\alpha_f$ and $v_{y,slip,r} = V\alpha_r$ be the lateral tyre slip speeds of front and rear axles, respectively. As a result, the lateral tyre slip power losses

$$P_{loss,\alpha} = -F_{y,f} v_{y,slip,f} - F_{y,r} v_{y,slip,r} = C_f V \alpha_f^2 + C_r V \alpha_r^2 \tag{2.4}$$

exhibit a minimum with respect to M_z, that is,

$$\frac{dP_{loss,\alpha}}{dM_z} = 0 \Longleftrightarrow M_z = \frac{m a_y \left[\frac{a_r}{C_f} - \frac{a_f}{C_r}\right]}{\frac{1}{C_f} + \frac{1}{C_r}} \tag{2.5}$$

It is also apparent that, according to the simplified model in (2.1), $P_{loss,\alpha}$ is independent of front and rear steering angles, δ_f and δ_r. Hence, it allows to conclude that the rear-wheel steering does not affect the tyre slip power losses, or it has a minor effect that cannot be observed with the proposed model.

To consider also the effects, if any, of δ_f and δ_r on tyre slip power losses, it is possible to resort to a nonlinear single-track vehicle model which is expressed as follows:

$$\begin{cases} -mrV\beta = F_x + C_f\alpha_f\delta_f + C_r\alpha_r\delta_r & \text{(2.6a)} \\ mrV = -C_f\alpha_f - C_r\alpha_r + k_dF_x\delta_f + (1-k_d)\,F_x\delta_r & \text{(2.6b)} \\ 0 = (-C_f\alpha_f + k_dF_x\delta_f)\,a_f - (-C_r\alpha_r + (1-k_d)\,F_x\delta_r)\,a_r + M_z & \text{(2.6c)} \\ \alpha_f = -\delta_f + \beta + \dfrac{ra_f}{V} & \text{(2.6d)} \\ \alpha_r = -\delta_r + \beta - \dfrac{ra_r}{V} & \text{(2.6e)} \end{cases}$$

in which β is the vehicle body sideslip angle, $r = a_y/V$ is the yaw rate and k_d is the longitudinal force distribution factor such that $F_{x,f} = k_dF_x$ and $F_{x,r} = (1-k_d)F_x$. (2.6a) is the longitudinal force balance with respect to the vehicle reference frame, (2.6b) is the lateral force balance and (2.6c) is the yaw moment balance. Also, the five relations are meaningful under the small-angle approximation of sideslip and steering angles.

Unless further simplifications are applied, the proposed nonlinear model does not lend itself to a closed-form analytical solution. Anyway, a numerical approach gives the results reported in Fig. 2.2, which are obtained for $a_y = 5$ m/s^2, $V = 100$ km/h, $M_z = 0$ Nm and realistic vehicle parameters. The figure displays the front (Fig. 2.2a) and rear (Fig. 2.2b) axles lateral tyre forces (see (2.3)) as well as the overall longitudinal force (Fig. 2.2c) and the total lateral tyre slip power losses (Fig. 2.2d) as functions of the rear wheel steering angle for three distinct values of k_d. Despite its briefness, the model reveals some interesting trends:

- Only the lateral forces of the driven axle show a dependence on δ_r.
- The total longitudinal force F_x exhibits a maximum that is biased towards the region of counter-phase δ_r, i.e. in the opposite (negative, in this case) direction of δ_f, regardless the longitudinal torque distribution.

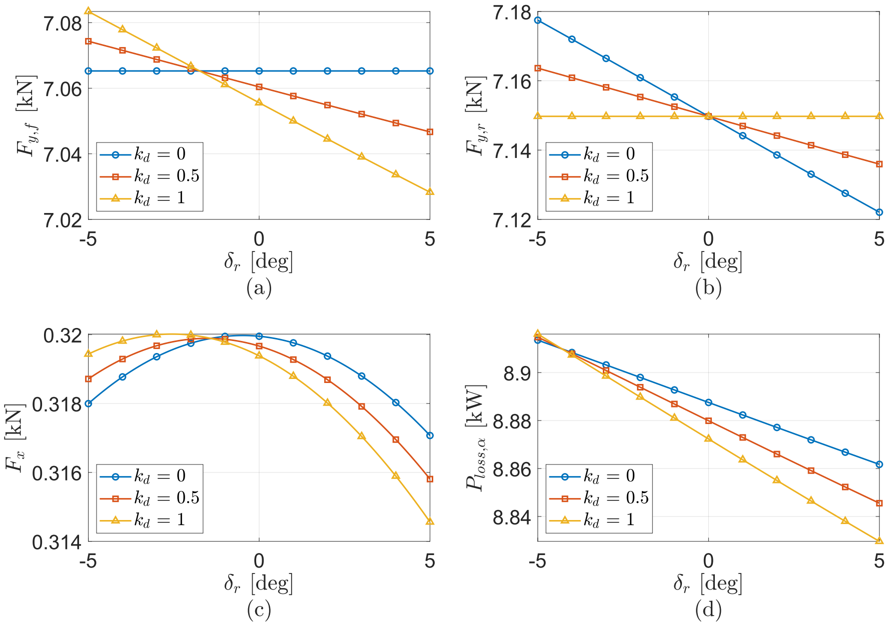

Figure 2.2: Effect of rear-wheel steering angle δ_r for different longitudinal force distributions. (a) Front axle side force. (b) Rear axle side force. (c) Total longitudinal force. (d) Total sideslip power losses.

- High values of in-phase δ_r, i.e. in the same (positive, in this case) direction as δ_f, correspond to the lowest values of F_x, which also translate into minimum longitudinal tyre slip power losses, regardless the longitudinal torque distribution.
- Front-wheel drive ($k_d = 1$) is predominantly the most energy-efficient solution in terms of longitudinal tyre slip power losses (directly proportional to F_x) and lateral tyre slip power losses. This finding is confirmed by [27].
- Regardless the longitudinal torque distribution, $P_{loss,\alpha}$ has a linear trend such that the more the rear-wheel is steered in phase, the more the lateral tyre slip power losses decrease.

A physical interpretation of these phenomena can be found by focusing on (2.6b) and (2.6c). If M_z is neglected, by rearranging their terms, the following expressions of the sideslip angles are derived:

$$\alpha_f = \frac{1}{C_f}\left(-ma_y\frac{a_r}{a_f+a_r}+k_d F_x \delta_f\right) \tag{2.7a}$$

$$\alpha_r = \frac{1}{C_r}\left(-ma_y\frac{a_f}{a_f+a_r}+(1-k_d)\,F_x \delta_r\right) \tag{2.7b}$$

where $a_y = rV$ is exploited. Let F_x be constant: the assumption is reasonable because the longitudinal force varies moderately in function of the small steering angles. If $k_d = 0$, α_f is constant for a given a_y, so it provides a constant contribution to the lateral tyre slip power losses. Conversely, α_r results in being a linear function of δ_r. Further, by virtue of small-angle approximation, it is reasonable to assume that

$$\left|-ma_y\frac{a_f}{a_f+a_r}\right| > |F_x\delta_r| \tag{2.8}$$

Hence, if $a_y > 0$, $\alpha_r < 0$: as δ_r is increased, α_r tends to approach zero, thus it determines a reduction of the lateral tyre slip power losses according to (2.4). A similar reasoning can be provided for $k_d = 1$. In this case, the rear-wheel steering angle has no effect on α_r, whereas α_f is a linear function of δ_f. By assuming

$$\left|-ma_y\frac{a_r}{a_f+a_r}\right| > |F_x\delta_f| \tag{2.9}$$

α_f approaches zero if δ_f is increased. In fact, to increase δ_f for a given a_y, it is possible to increase δ_r, as well. A proof of the last statement can be inferred by subtracting (2.6d) by (2.6e), which yields

$$\alpha_f - \alpha_r = -\delta_f + \delta_r + \frac{a_y\,(a_f+a_r)}{V^2} \tag{2.10}$$

and by plugging (2.7a) and (2.7b) into (2.10), thus obtaining

$$\delta_f = \frac{C_f}{F_x+C_f}\left[\delta_r + \frac{ma_y}{C_f}\left(\frac{a_r}{a_f+a_r}\right) - \frac{ma_y}{C_r}\left(\frac{a_f}{a_f+a_r}\right) + \frac{a_y\,(a_f+a_r)}{V^2}\right] \tag{2.11}$$

So far, the contributions of torque vectoring, rear-wheel steering and longitudinal force (namely, torque), distribution have been assessed from a predominantly analytical perspective. For the sake of completeness, it is worth observing that anti-roll moment distribution impose a more complex analytical analysis due to the need to adopt at least a planar vehicle model with four wheels (see Section 1.3.1), rather than a single-track one, and a nonlinear tyre model. This explains the omission of anti-roll moment distribution effect from the analytical inspection of the present section.

After all, the models described so far are based on a significant number of approximations: to dive into the deepest phenomena that permeate the vehicle system, a high-fidelity nonlinear model is an indispensable and precious tool.

2.3 Simulation environment

2.3.1 The high-fidelity vehicle model

The case study vehicle is fully electric (FEV) and is endowed with four in-wheel-motors: its main parameters are listed in Table 2.1 (see also Fig. 2.1 for the fundamental quantities). The vehicle is simulated with a high fidelity and experimentally validated simulation model, which is implemented by means of AVL VSM simulator. By way of example, experimental validation results in quasi-steady-state conditions for the baseline configuration of the demonstrator vehicle are reported in Fig. 2.3. Both the two-wheel-drive (2WD) and the four-wheel-drive (4WD) configurations are examined in order to assess the effects on energy-efficiency, if any, brought by the actuation of all wheels on the same vehicle: the former has a static distribution of the total torque that is completely biased towards the rear axle, whereas the latter is free to allocate the torque on the two axles according to an energy-efficiency criterion. Indeed, not only has the drivetrain layout effects on vehicle cornering response, but, typically, is also responsible for a reduction of the overall powertrain power losses. Essentially, the additional degree-of-freedom allows the single motors of a vehicle side to work in a more efficient region for a given velocity and total side torque demand. As a result, the 4WD architecture with independent drives lends itself to an off-line optimisation which provides the most efficient total lateral torque distribution between the two motors of

Table 2.1: Main vehicle parameters.

Description	Symbol	Value	Unit
Front semi-wheelbase	a_f	1.47	m
Rear semi-wheelbase	a_r	1.46	m
Front track width	b_f	1.66	m
Rear track width	b_r	1.66	m
Center of gravity height	h_{CG}	0.63	m
Wheel radius	R	0.37	m
Total mass	m	2843	kg
Roll mass moment of inertia	J_x	550	kg m^2
Yaw mass moment of inertia	J_z	5291	kg m^2

the same side. Therefore, let the subscript $i = f, r$ designate the front (f) or rear (r) axle, and let $j = l, r$ specify the left-hand (l) or right-hand (r) side. The minimisation, which is performed for each working point $\left(\Omega_j, T_{el,req,j}\right)$, can be described by

$$f_{T,opt,j} = \min_{f_{T,j}} \left(\hat{P}_{loss,el,fj} \left(\Omega_j, f_{T,j} T_{el,req,j}\right) + \hat{P}_{loss,el,rj} \left(\Omega_j, \left[1 - f_{T,j}\right] T_{el,req,j}\right) \right) \tag{2.12}$$

where $f_{T,j}$ is the front-to-total motor torque distribution coefficient, $f_{T,opt,j}$ is the corresponding optimised value, Ω_j is the average rotational motor (and wheel) velocity of j side, $T_{el,req,j}$ is the overall j side motor torque request and $\hat{P}_{loss,el,ij}$ is the power loss of the individual ij powertrain. Thus, for the given powertrains, the process provides the map in Fig. 2.4, in case of motoring. A similar map is derived for the regenerative region. Fundamentally, up to about 1000 RPM, the distribution coefficient is zero at low side torque requests, 0.5 elsewhere. Moreover, at high velocities the map becomes more erratic. It is worth noting that the aforementioned optimisation, owing to its algebraic nature, does not account for dynamic effects like the tyre slips induced by a sudden engagement of the front wheel.

Regarding the powertrains considered in this study, the power losses for the single

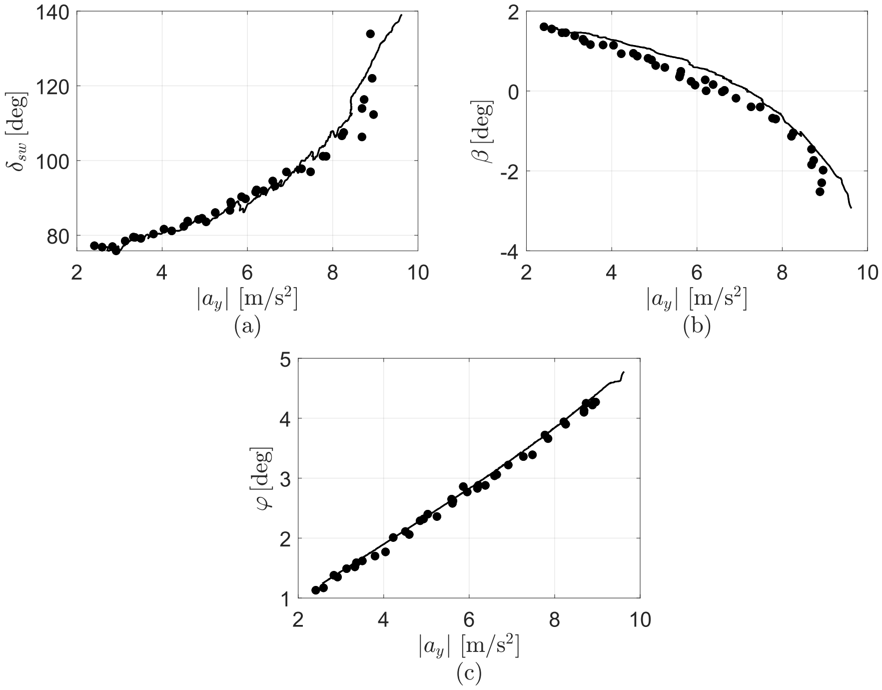

Figure 2.3: Validation of the vehicle model on 40 m radius skidpad manoeuvre. Experimental data (dots) versus model (continuous line) as functions of a_y. (a) Steering wheel angle δ_{sw}. (b) Sideslip angle β. (c) Roll angle φ.

ij powertrain, $\hat{P}_{loss,el,ij}$, are represented in Fig. 2.5 as a function of the motor velocity and of its torque. In addition to the powertrain power losses, the tyre slip power losses have a significant weight among the loss entries of a vehicle. Let $v_{x,slip,ij}$ and $v_{y,slip,ij}$ be, respectively, the longitudinal and lateral tyre slip speeds of the ij wheel with respect to the wheel reference frame. Similarly, let $F_{x,ij}$ and $F_{y,ij}$ be the longitudinal and lateral tyre forces. The tyre slip power losses can be divided into longitudinal,

$$P_{loss,\sigma} = -(v_{x,slip,fl}F_{x,fl} + v_{x,slip,fr}F_{x,fr} + v_{x,slip,rl}F_{x,rl} + v_{x,slip,rr}F_{x,rr}) \tag{2.13}$$

and lateral tyre slip power losses,

$$P_{loss,\alpha} = -(v_{y,slip,fl}F_{y,fl} + v_{y,slip,fr}F_{y,fr} + v_{y,slip,rl}F_{y,rl} + v_{y,slip,rr}F_{y,rr}) \tag{2.14}$$

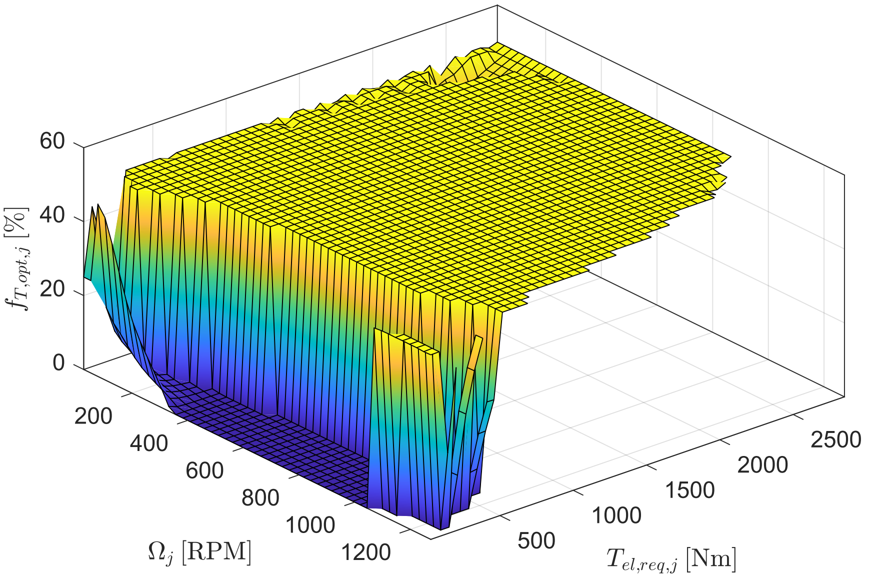

Figure 2.4: Optimal front-total motor torque distribution $f_{T,opt,j}$, in motoring conditions, as a function of the average rotational motor velocity Ω_j and of the overall j side motor torque request $T_{el,req,j}$.

Specifically,

$$v_{x,slip,ij} = v_{x,ij} - \Omega_{ij} R \tag{2.15}$$

$$v_{y,slip,ij} = v_{x,ij} \tan \alpha_{ij} \tag{2.16}$$

where $v_{x,ij}$ is the longitudinal component of wheel hub speed with respect to the wheel frame, ω_{ij} is the wheel rotational velocity, R is its radius and α_{ij} is the wheel sideslip angle.

An example of the contribution of the three fundamental power losses terms as a function of the lateral acceleration a_y is shown in Fig. 2.6. Evidently, both the total powertrain power losses and the longitudinal tyre slip power losses manifest a similar behaviour, that is, a monotonically increasing trend with a gentle slope up to about 7

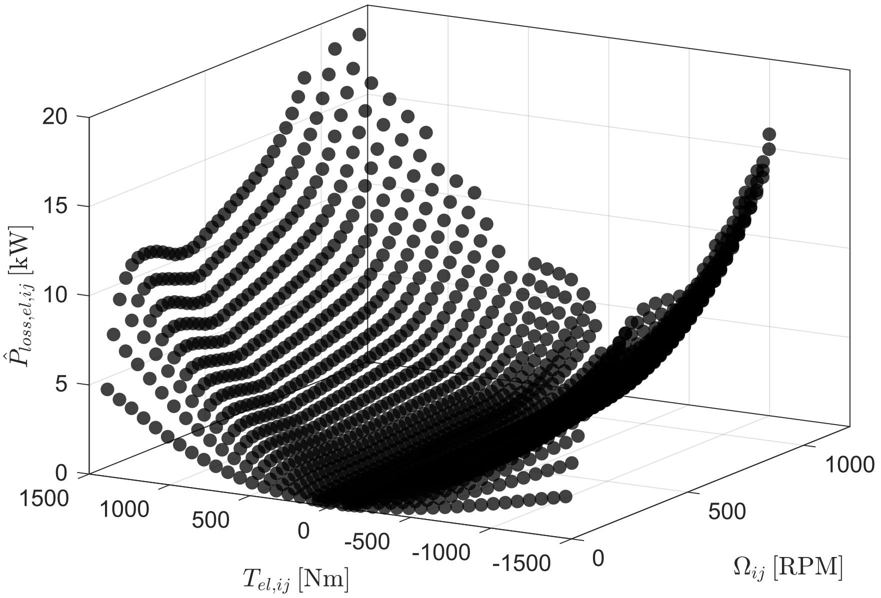

Figure 2.5: Powertrain power losses for the single ij powertrain.

m/s^2, albeit the latter have a significantly lower magnitude. It is worth pointing out that the sudden increase of the two curves that can be noticed above 7 m/s^2 witnesses the approach to the lateral cornering limit of the vehicle. As regards the lateral tyre slip power losses, the related curve exhibits a significant increase throughout the domain which reflects the expected increment of the overall lateral force needed to balance the growing centrifugal action.

Moving on to the factual implementation of the active system, the desired active yaw moment M_z is obtained via torque vectoring by manipulating the torque requests $T_{el,ij}$ to each single motor according to the following equations:

$$T_{el,fl} = f_{T,opt,l}\left(\frac{T_{el,req}}{2} - \frac{2R}{b_f + b_r}M_z\right) \tag{2.17a}$$

$$T_{el,fr} = f_{T,opt,r}\left(\frac{T_{el,req}}{2} + \frac{2R}{b_f + b_r}M_z\right) \tag{2.17b}$$

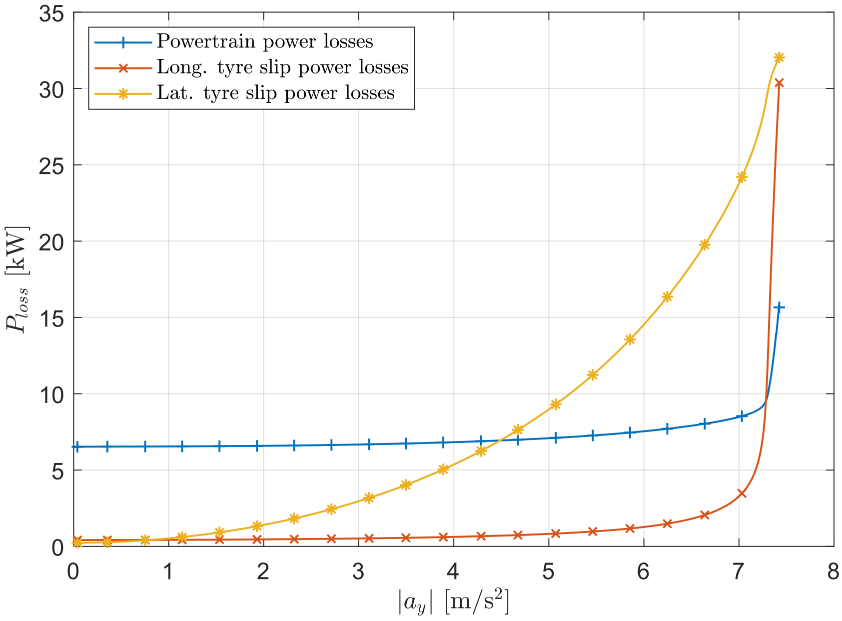

Figure 2.6: Example of the fundamental power loss entries during a typical ramp steer as a function of the lateral acceleration.

$$T_{el,rl} = \left(1 - f_{T,opt,l}\right)\left(\frac{T_{el,req}}{2} - \frac{2R}{b_f + b_r}M_z\right) \tag{2.17c}$$

$$T_{el,rr} = \left(1 - f_{T,opt,r}\right)\left(\frac{T_{el,req}}{2} + \frac{2R}{b_f + b_r}M_z\right) \tag{2.17d}$$

in which $T_{el,req} = \sum_{i,j} T_{el,ij}$ is the total motor torque request, R is the wheel radius and b_i is the vehicle track. Hence, the four relationships ensure the fulfilment of the overall torque demand and active yaw moment.

Furthermore, the total anti-roll moment provided by the active suspensions is computed as

$$M_{AR,Act,Tot} = wma_y\left[h_{CG} - h_{roll}\right] \tag{2.18}$$

in which w is a scaling coefficient that is tuned according to the desired roll angle characteristic, m is the vehicle mass, a_y is the lateral acceleration, h_{CG} is the height from the ground of the centre of gravity in static conditions and h_{roll} is the height from the ground of the average roll centre. Consequently, front and rear contributions are, respectively,

$$M_{AR,Act,f} = f M_{AR,Act,Tot} \tag{2.19}$$

and

$$M_{AR,Act,r} = [1-f]\, M_{AR,Act,Tot} \tag{2.20}$$

being f the front-to-total anti-roll moment distribution coefficient. The corresponding vertical forces, applied to each wheel centre, due to the active suspensions are

$$F_{il} = -\frac{M_{AR,Act,i}}{b_i} \tag{2.21a}$$

$$F_{ir} = +\frac{M_{AR,Act,i}}{b_i} \tag{2.21b}$$

Finally, as regards the rear-wheel steering, the same angle δ_r is applied to both rear wheels. The resultant Ackermann violation is negligible because the explored angles are relatively small. After all, a strict implementation of such architecture would impose also a variable geometry of the front-steering, which could be achieved through active tie rods: however this goes beyond the objectives of this study.

2.3.2 Simulation campaign

The simulation campaign is entirely based on a set of ramp steer manoeuvres: each test consists in a steering wheel angle ramp applied at a rate of 5 deg/s, while the vehicle travels at a given constant speed, and for given values of adherence and longitudinal acceleration (see below). Precisely, the inspected speeds V are 50, 100 and 120 km/h; the grip levels $\mu_{\%}$ are 70% and 100%, i.e. full adherence; the longitudinal accelerations a_x are 0 and 1.5 m/s^2. The ramp steer manoeuvre is chosen because it allows to explore uniformly the whole range of lateral accelerations. As concerns a_x, strictly speaking, this is not an actual acceleration, but it corresponds to an external action that is applied in the form of a longitudinal barycentric force with magnitude $F_{ext} = m a_x$, where m

Table 2.2: Explored parameters for the fundamental quantities related to the three active systems, i.e. direct yaw moment M_z, rear-wheel steering angle δ_r and front-to-total anti-roll moment distribution f.

	Min	Max	Unit	No. of pts
M_z	-2	2	kNm	9
δ_r	-2	2	deg	11
f	0.2	0.8	-	6

is the total vehicle mass. Within the context of this analysis, it is called *acceleration* because, ultimately, this is the quantity of interest and from power consumption viewpoint the inertial force ma_x acts like an external force with the same magnitude. The clarification is needed because the reader may question about the fact that constant longitudinal accelerations are performed at constant speed. Again, a_x is considered as the acceleration that, multiplied by the total vehicle mass, produces an external force with the same magnitude as the longitudinal inertial action. This approach allows to probe the effect of an additional workload, equivalent to the inertial one that arises in the presence of an actual longitudinal acceleration, without introducing secondary transient effects which would alter the substantial quasi-steady-state nature of the ramp steer manoeuvre itself.

Additionally, the ramp steer manoeuvre is performed for all possible combinations of the parameters indicated in Table 2.2, which correspond to the quantities directly modulated by the three actuation systems, i.e. direct yaw moment M_z, rear-wheel steering angle δ_r and front-to-total anti-roll moment distribution f.

Therefore, by considering $9 \cdot 11 \cdot 6 = 594$ (see Table 2.2) combinations of parameters, 2 drivetrains (2WD and 4WD) and $3 \cdot 3 \cdot 2 = 12$ test conditions (concerning V, $\mu_{\%}$ and a_x), the total number of simulations performed is $594 \cdot 2 \cdot 12 = 14256$.

Algorithm 1: data filter

```
1  **for** each triple ($M_z$, $\delta_r$, $f$)
2      **for** $k$ from 1 to no. of samples – 1
3          $k_{\delta,init}$ = first $k$ s.t. $|\delta_{sw,k}| > |\delta_{sw,thr}|$
4          $k_{V,init} = k$ s.t. $V_k = \max V$;
5          $k_{P,init}$ = first $k$ s.t. $P_{batt,k+1} - P_{batt,k} < \Delta P_{init,thr}$
6          $k_{init} = \max\left(k_{sw,init}, k_{V,init}, k_{P,init}\right)$
7          **for** $k$ from $k_{init}$ to no. samples – 1
8              $k_{a_y,end}$ = first $k$ s.t. $\left|a_{y,k}\right| > c \max |a_y|$
9              $k_{P,end}$ = first $k$ s.t. $P_{batt,k+1} - P_{batt,k} < \Delta P_{end,thr}$
10             $k_{end} = \min\left(k_{a_y,end}, k_{P,end}\right)$
11         **end**
12     **end**
13     $\widetilde{a}_y = \left[a_{y,k_{init}}, a_{y,k_{init}+1}, \dots, a_{y,k_{end}-1}, a_{y,k_{end}}\right]$
14     $\widetilde{\delta}_{sw} = \left[\delta_{sw,k_{init}}, \delta_{sw,k_{init}+1}, \dots, \delta_{sw,k_{end}-1}, \delta_{sw,k_{end}}\right]$
15     $\widetilde{P}_{batt} = \left[P_{batt,k_{init}}, P_{batt,k_{init}+1}, \dots, P_{batt,k_{end}-1}, P_{batt,k_{end}}\right]$
16 **end**
```

2.4 Post-processing methodology

2.4.1 Data filter design

Doubtless, the trustworthiness of the analysis of such a quantity of raw data strongly depends on the reliability and robustness of the post-processing.

The first stage consists in selecting the significant portion of each curve relating the steering wheel angle δ_{sw} to the lateral acceleration a_y: this function is commonly referred to as *understeer characteristic*. This procedure can be summarised by means of Algorithm 1. Essentially, the algorithm is in charge to detect the two events that delimit the meaningful part of each simulation performed for the triple (M_z, δ_r, f). Let k be the index that identifies the k-th sample of a given signal. As stated at line 6, k_{init}, that is, the index that marks the beginning of the significant part, is defined as the maximum of three indices, namely,

a. $k_{\delta,init}$, ticking where the steering wheel rotation starts, or, in other words, where the steering wheel angle δ_{sw} exceeds the threshold $\delta_{sw,thr}$;

b. $k_{V,init}$, labelling where the vehicle reaches the reference speed of the manoeuvre that is, in fact, the peak value;

c. $k_{P,init}$, indicating, if any, the attainment of a battery power usage plateau following the transient needed to reach the reference speed. This value occurs where the power variation is lower than the threshold $\Delta P_{init,thr} > 0$ for the first time.

Similarly to the determination of the starting point, the research of the last significant sample relies on the detection of a pair of meaningful occurrences, namely,

a. the first time the lateral acceleration exceeds c times its maximum value, where $0 \leq c \leq 1$; the event, which corresponds to the index $k_{a_y,end}$, marks the beginning of the region where data are not reliable due to the excessive slips.

b. the first apparent power drop, attesting extreme tyre spinning and motor torque saturation. The phenomenon, indicated by $k_{P,end}$, occurs where the battery power variation is lower than the threshold $\Delta P_{end,thr} < 0$ for the first time.

Thus, the terminal index k_{end} is the minimum of $k_{a_y,end}$ and $k_{P,end}$. Finally, as stated at lines 13-15, the raw signals are trimmed based on the two indices in order to obtain the three filtered vectors $\widetilde{a}_y$, $\widetilde{\delta}_{sw}$ and $\widetilde{P}_{batt}$, which store the significant values of, longitudinal acceleration (a_y), steering wheel angle (δ_{sw}) and battery power usage (P_{batt}), respectively. Therefore, for each combination of direct yaw moment M_z, rear-wheel steering angle δ_r and front-to-total anti-roll moment distribution f, a three-dimensional understeer characteristic is obtained, where the third dimension is represented by the battery power consumption. Henceforth, a three-dimensional understeer characteristic in $a_y\delta_{sw}P_{batt}$-space will be referred to as *extended understeer characteristic*.

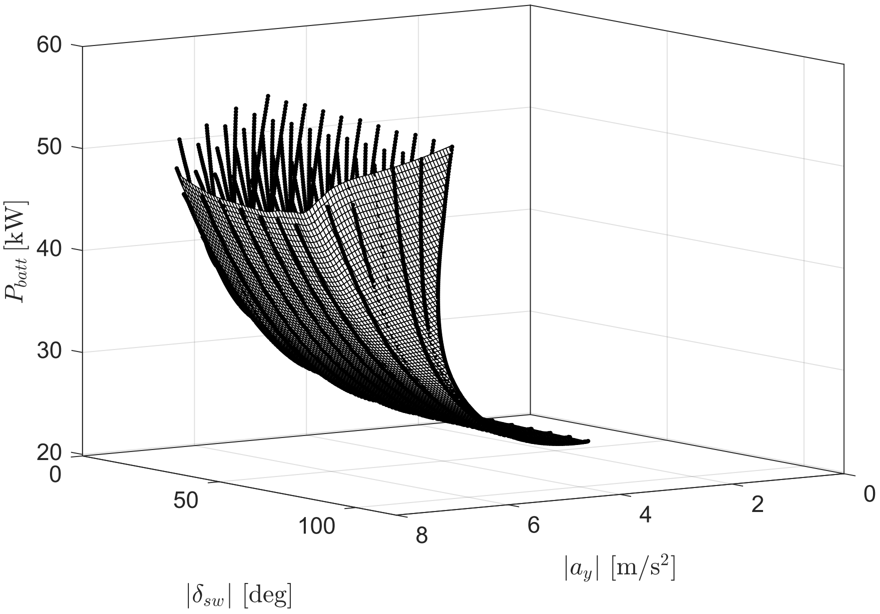

Figure 2.7: Example of minimum power envelope, that is, the mesh that touches the curves manifesting the lowest power usage.

2.4.2 Extraction of the minimum power envelope

Generally, for a multi-actuated vehicle, it is possible to achieve the same working point (a_y, δ_{sw}) through different blends of the available actuations: what differentiate them is the corresponding power usage. Therefore, the *minimum power envelope*, $P_{batt,min}(a_y, \delta_{sw})$, is the continuous surface that accommodates the points that show the lowest power consumption for each factually achievable working point related to a given combination of actuations. An example of the aforementioned surface is displayed in Fig. 2.7. By virtue of its continuous nature, the minimum power envelope provides the best approximation of the lowest battery power usage achievable, through a given set of actuations, in each working point of $a_y\delta_{sw}$-plane.

The extraction of the minimum power envelope translates to Algorithm 2. As suggested by the pseudocode, the procedure is based first on a data binning algorithm

Algorithm 2: extraction of the minimum power envelope

```
1  Repartition of the domain $a_y\delta_{sw}$ into $\hat{u}$ sub-grids
2  for $u$ from 1 to $\hat{u}$
3      for $v$ from 1 to no. of bins in sub-grid $i$
4          $P_{batt,min,uv} = \min \widetilde{P}_{batt,uv}$
5      end
6  end
7  $\widetilde{S} = \left\{ (a_y, \delta_{sw}, P_{batt}) \ : P_{batt} \text{ is in } \widetilde{P}_{batt,min} \right\}$
8  Fitting of points in $\widetilde{S}$ to obtain $P_{batt,min}\,(a_y, \delta_{sw})$
```

(lines 1-7) and then on a fitting of the selected points (line 8). More precisely, the domain $a_y\delta_{sw}$ is partitioned in, possibly, more than one grid. The presence of multiple grids with distinct resolutions allows to compensate for the reduction of density of points that typically appears as the lateral acceleration increases. Indeed, the size of the tiles that constitute each grid is crucial since it acts as the fundamental parameter of the binning-like filter. Thus, for a given bin v belonging to the sub-grid u, the point $(a_y, \delta_{sw}, P_{batt})$ that exhibits the lowest battery power usage $P_{batt,min,uv}$ is selected from the set $\widetilde{P}_{batt,uv}$, which is the set of all power values belonging to partition uv. The set of all the points picked in such a way is $\widetilde{S}$. In fact, $\widetilde{P}_{batt,min}$ is the set of the lowest power values of each partition uv. The actual MATLAB function that performs the extraction of $\widetilde{S}$ is in Appendix A. Subsequently, a fitting is performed on the points in $\widetilde{S}$: the function so obtained depicts the minimum power envelope, that is, the function that establishes the relationship between a_y, δ_{sw} and the lowest battery power. Specifically, the fitting algorithm adopted for this study relies on a biharmonic interpolation because this method shows remarkable smoothing properties.

2.5 Simulation results

2.5.1 Relative distribution of minimum power

In the context of the present analysis, a *carpet* is a colour map that displays the battery power distribution of a given minimum power envelope in terms of power increase, for each value of lateral acceleration, relative to the minimum power used along the so-called *energy-efficient understeer characteristic*. The energy-efficient understeer characteristic, sometimes also referred to as *optimal* understeer characteristic, is the curve that allows to achieve the lowest battery power consumption for each value of lateral acceleration. Accordingly, each point of a carpet, i.e. the battery power increase $P_{batt,inc}$, is computed as follows:

$$P_{batt,inc}\left(a_y,\delta_{sw}\right)=\left(\frac{P_{batt,min}\left(a_y,\delta_{sw}\right)-P_{batt,opt}\left(a_y\right)}{P_{batt,opt}\left(a_y\right)}\right)\cdot 100 \qquad (2.22)$$

where $P_{batt,min}$ is the power provided by a given minimum power envelope, whereas $P_{batt,opt}$ is the battery power fetched on the same minimum power envelope along the optimal understeer characteristic.

A significant example of collection of carpets is reported in Fig. 2.8. In order to allow the direct comparison between the different cases, the same power increase range (0-30%) is adopted in all instances, though this may provide essentially uniform maps where $P_{batt,inc}$ is relatively small throughout the region. However, this minor drawback does not compromise the effectiveness of the representation. In addition to the carpets themselves, three understeer characteristics are shown for each combination of actuations.

1. The black line is the so-called *neutral steering characteristic*; this is independent of the actuation and is computed as

$$\delta_{sw}=k_{sw}\arctan\left(\frac{\left(a_f+a_r\right)a_y}{V^2}\right) \qquad (2.23)$$

   in which $k_{sw}\approx 18$ deg is the steering wheel gain with respect to the average front-wheel steering angle. As its name may suggest, the curve depicts the working points of a neutral steering vehicle.

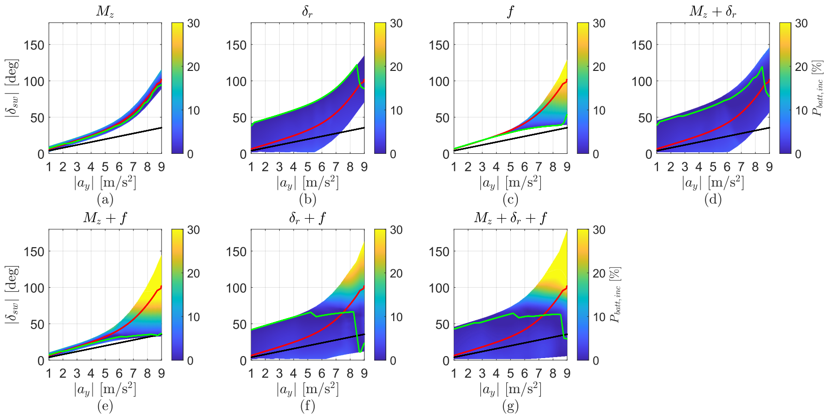

Figure 2.8: Example of carpets for the 2WD drivetrain in case $V = 100$ km/h, $\mu_{\%} = 100\%$ and $a_x = 0$ m/s^2.

2. *The baseline understeer characteristic* (or, more briefly, baseline) is the red curve in each subplot, which is independent of the specific actuations. Indeed, the baseline is obtained for the base values of the fundamental parameters of the active systems, i.e. $M_z = 0$, $\delta_r = 0$ and $f = f_{pass}$, where $f_{pass} = 0.67$. This configuration is referred to as *baseline set-up*. For the sake of clarity, 0.67 (i.e. the f applied by the active suspensions) is the same front-to-total anti-roll moment distribution as the one provided by the passive anti-roll bars. In case of single actuations, the *extended* baseline belongs to the minimum power envelope, whereas this is generally false with respect to multiple actuations.

3. Finally, the green curves that unwind across the colour maps are the *energy-efficient understeer characteristics* (as defined above) provided by the distinct combinations of actuations. It is worth mentioning that, within the context of this analysis, the optimal understeer characteristics are extracted from the bundle of discrete curves produced by each set of simulations. Consequently, the most efficient understeer characteristics, being the results of the concatenation of portions of distinct curves, may exhibit erratic trends. Hence, a moving average filter is applied to these curves to smooth the transitions. Of course, it

is reasonable to expect smoother shifts as the quantisation due to the parameter discretisation decreases.

Fig. 2.8 is a collection of the seven plots provided by all possible sets of actuations; these are ideally sorted from the commonest (torque vectoring) to the least common (triple actuation) combination of active systems. On the top of each sub-figure, the abuse of notation indicates the corresponding set of actuations: M_z for direct yaw moment (TV), δ_r for rear-wheel steering, and f for anti-roll moment distribution. Furthermore, it is worth clarifying that the absence of front-to-total anti-roll moment distribution implies that anti-roll moment compensation via active suspension is still available, though f is fixed and equal to f_{pass}.

The analysis of the relative power increase distribution reveals some significant trends which repeat as the test conditions change. Further, some of them confirm what can be roughly predicted through the simple models proposed in Section 2.2.

Fig. 2.8a shows that, in case of torque vectoring, the most efficient curve is generally close to the baseline, and is mainly below it. Not only is the behaviour partly suggested by (2.5), but also it finds a visual justification in the W-shaped cross section of the minimum power envelope [21] as depicted in Fig. 2.9. The behaviour mirrors the fact that torque vectoring can allow tyres to operate in a more favourable region but the increase of direct yaw moment magnitude impacts considerably on the powertrain usage. As a result, power usage increase can exceed 10% on the borders of the carpet.

Fig. 2.8b immediately stands out for the wide area covered by the carpet, which is characterised by very gentle lateral slopes, as proved by the essentially uniform colour distribution. The high-fidelity nonlinear model adopted for the simulation campaign discloses that, in case of rear-wheel steering as a single actuation, the optimal understeer characteristic is such that relatively high values of in-phase rear-wheel steering angle offer the lowest battery power utilisation. For the sake of clarity, a rear angle is in-phase if it has the same orientation as the front one. This result confirms the deficiency of the linear model presented in (2.1), but is consistent with the sight on the phenomenon provided by the nonlinear model expressed by (2.6).

Essentially, Fig. 2.8c reveals that, if the trailing part of the green curve is neglected, the active distribution of the anti-roll moment generates an optimal understeer charac-

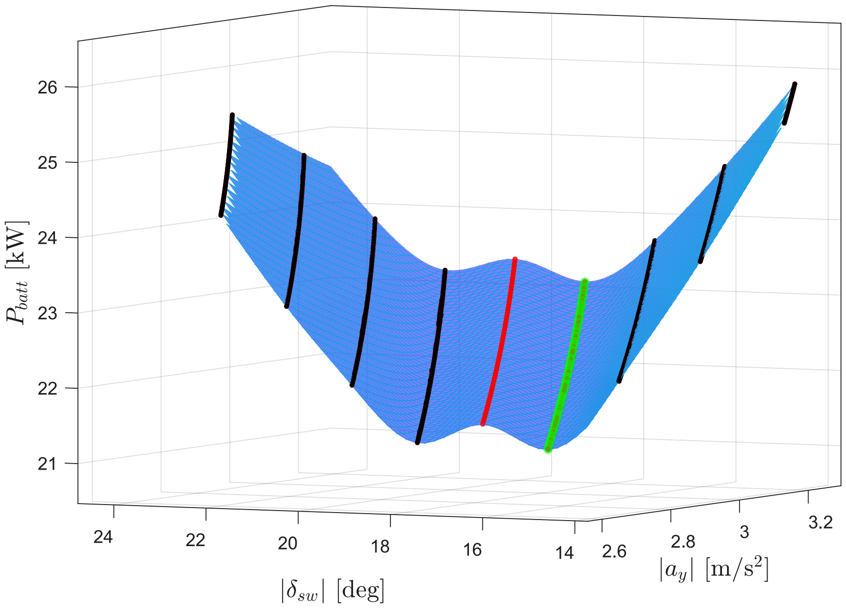

Figure 2.9: W-shaped cross section of the minimum power envelope with respect active yaw moment as a single actuation. Minimum power envelope (in blue), Discrete understeer characteristics (in black), baseline (in red) and optimal understeer characteristic (in green).

teristic that is always as close as possible to the neutral steering line. In fact, this trend mirrors the attempt of the active suspensions to minimise the tyre slip power losses, which are minimal, indeed, when the vehicle follows faithfully the direction imposed by the steering wheel. Moreover, at high-lateral accelerations, power usage increase relative to the optimal power profile can reach 30%. Additionally, that fact that up to ~5 m/s^2 the carpet surface coincides with a single curve (the baseline) is a proof of the poor authority of anti-roll moment distribution in case of moderate lateral load shifts.

It is easy to realise that the combinations of actuations yield carpets and energy-efficient understeer characteristics which are blends of those obtained by means of the single actuations. As a matter of fact, the dominant contribution up to medium values of lateral accelerations is the one of the rear-wheel steering, if present, whereas the effect of active suspensions is more pronounced at higher a_y. In fact, in Fig. 2.8d, Fig. 2.8f and Fig. 2.8g the green line starts very close to the upper border and then it progressively drifts to the middle region or even to the lower bound as in Fig. 2.8f.

Finally, in Fig. 2.8e it is interesting to observe the clear contributions of the two active systems: torque vectoring prevails at low lateral accelerations and, the more the lateral accelerations become significant, the more anti-roll moment distribution via active suspensions acquires authority.

So far, the analysis of carpets has been conducted by focusing on a specific test ($V = 100$ km/h, $\mu_{\%} = 100\%$ and $a_x = 0$ m/s^2) and drivetrain (2WD). This approach is sustained by the fact that the fundamental trends persist also as the test conditions and drivetrain architecture vary. To show this, some additional carpets are reported in Appendix B. To be precise, there exist some noteworthy deviations from the general behaviours, which deserve further comments. Firstly, on respect of those sets of actuations including δ_r (i.e. δ_r, $M_z + \delta_r$, $\delta_r + f$ and $M_z + \delta_r + f$), the presence of longitudinal acceleration $a_x = 1.5$ m/s^2 at 50 km/h determines the fact that, at low-to-medium lateral accelerations, counter-phase rear-wheel steering is more energy-efficient. The behaviour can be observed in Fig. B.2 and B.4. As a result, the optimal understeer characteristics exhibit abrupt transitions from the lower bound to the upper bound of the carpet. Secondly, in the presence of $a_x = 1.5$ m/s^2, the optimal understeer characteristic generated by f on its own tends to stay closer to the baseline: this is the case of Fig. B.2, B.4 and Fig. B.6. However, this trend is observable only in case of 2WD architecture.

2.5.2 Relative profile of minimum power along the energy-efficient understeer characteristic

A more in-depth analysis of the contributions of the different actuations in terms of energy saving is provided by comparing the minimum power profiles of each combination of actuations along the respective energy-efficient understeer characteristics. More specifically, in this section, $P_{batt,opt}$ (see Section 2.5.1 for its definition) of a given set of actuations is expressed in terms of power increase ($P_{batt,inc}$) relative to a reference power profile $P_{batt,ref}$, namely

$$P_{batt,inc}\left(a_y\right) = \left(\frac{P_{batt,opt}\left(a_y\right) - P_{batt,ref}\left(a_y\right)}{P_{batt,ref}\left(a_y\right)}\right) \cdot 100 \tag{2.24}$$

Unless otherwise noted, $P_{batt,ref}$ coincides with $P_{batt,opt}$ of the most over-actuated configuration, i.e. the 4WD vehicle endowed with triple actuation. In fact, this set-up is expected to be capable to ensure the lowest battery power usage.

Only two testing conditions are examined in detail since they are sufficient to convey the fundamental findings. Precisely, the first set of results concerns the experiment for $V = 100$ km/h, $\mu_{\%} = 100\%$ and null longitudinal acceleration. The second collection descends from the test that differs from the previous one only because $a_x = 1.5$ m/s^2.

Fig. 2.10 shows the curves related to the single actuations, the baseline set-ups and the triple actuations ($M_z + \delta_r + f$). By construction, for a given drivetrain, the baseline marks the upper bound of the region in which the other curves can be, whilst $M_z + \delta_r + f$ delimits the lower bound of the area in question. As can be seen, for the current case, the homologous curves of the 2WD and the 4WD are essentially superposed throughout the domain. The predominant overlap is justified by the fact that, for the present working conditions, the actuation of a single axle is a more efficient solution. In other words, the superposition is due to the fact that, actually, the 4WD vehicle (that is, the vehicle with active longitudinal torque distribution on each side) is behaving like the 2WD (that is, the vehicle with fixed longitudinal torque distribution $f_{T,j} = 0$ on both sides) because the actuation of a single axle is more energy efficient. However, in the presence of torque vectoring as a single actuation as well as in conjunction with the other two active systems, the engagement of the front axle occurs, giving rise to a singular behaviour. Truly, immediately after the activation of the front wheels and for a limited range of lateral accelerations, the 2WD is temporarily slightly more efficient than the 4WD counterpart. Albeit this phenomenon may look as an error at a first glance, it finds a sound explanation in the algebraic nature of the optimisation described by (2.12): this relationship does not account for the transient effects such as the additional tyre slips induced by the abrupt engagement of the 4WD, which may alter, for a very short time, the quasi-steady-state

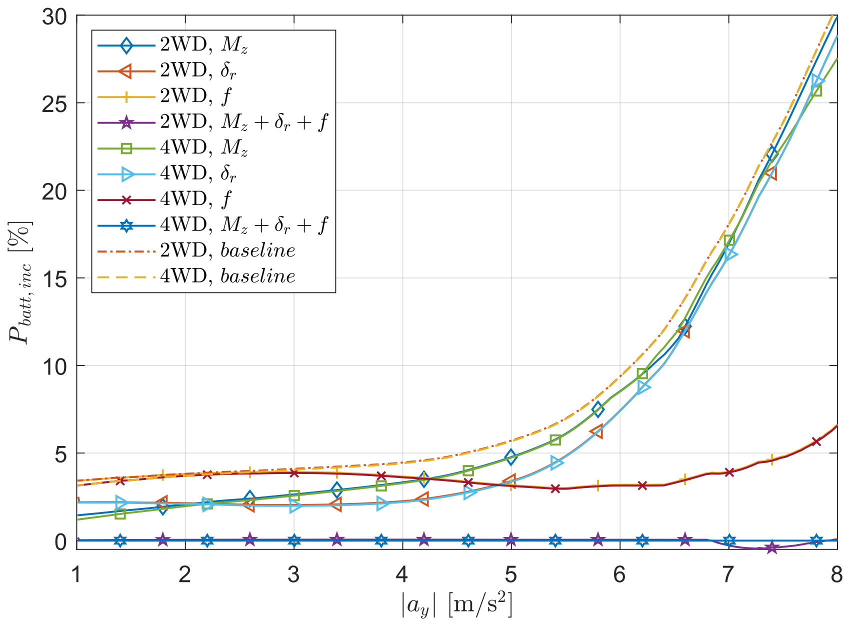

Figure 2.10: Relative profile of minimum power along the energy-efficient understeer characteristic. Single actuations. $V = 100$ km/h, $\mu_{\%} = 100\%$ and $a_x = 0$ m/s^2.

essence of the ramp steer. To clarify, the occurrence exists at about 6.2 m/s^2 in case of pure torque vectoring and at about 6.9 m/s^2 if the three actuations are available.

Anyway, Fig. 2.10 reports some clear trends: torque vectoring and, mostly, rear-wheel steering are beneficial up to medium lateral accelerations, whereas the active roll-moment distribution, by virtue of its almost flat tendency, becomes significantly more efficient than the other two systems at higher lateral accelerations. After all, by observing the Fig. 2.8c, it is easy to notice that, at low lateral accelerations, the active suspensions do not give any advantage relative to the baseline. Also, at high a_y, the advantages of the torque vectoring and rear-wheel steering relative to the baselines become almost negligible.

In Fig. 2.11 the baselines and the curves concerning the triple-actuated configurations are displayed again as terms of comparison. Also, the figure shows the curves

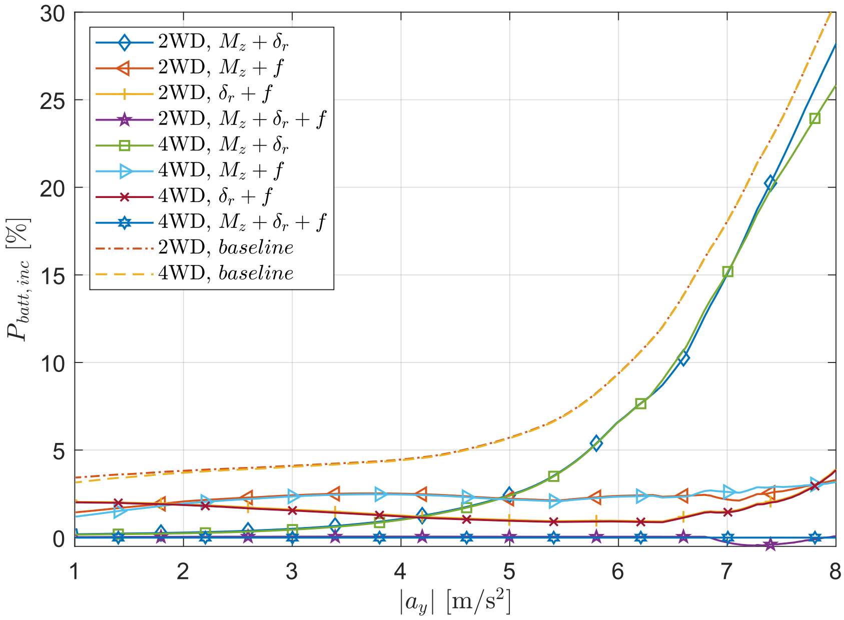

Figure 2.11: Relative profile of minimum power along the energy-efficient understeer characteristic. Multiple actuations. $V = 100$ km/h, $\mu_{\%} = 100\%$ and $a_x = 0$ m/s^2.

related to the combinations of two actuators. What stated for the previous figure is still valid: as a matter of fact, the trends reported in Fig. 2.11 can be easily inferred by superposing the elementary tendencies of the single actuations. Namely, TV in conjunction with RWS results in being the most beneficial double actuation up to ~4 m/s^2, but then it is overwhelmed by the combinations exploiting the active suspensions. Furthermore, the pair $\delta_r + f$ is generally more efficient than $M_z + f$.

The results described so far are presented in a concise fashion in Fig. 2.12. The average battery power increase $\bar{P}_{batt,inc}$ is displayed in the form of bar plots for distinct bands of lateral accelerations, namely 1-3 m/s^2 (low a_y), 3-5 m/s^2 (mid a_y), 5-7 m/s^2 (high a_y), and 1-7 m/s^2 (whole). The reference power profile belongs to the most over-actuated configuration (4WD, $M_z + \delta_r + f$). It is interesting to notice that, if the entire a_y range is considered, the combinations of actuations are sorted in descending

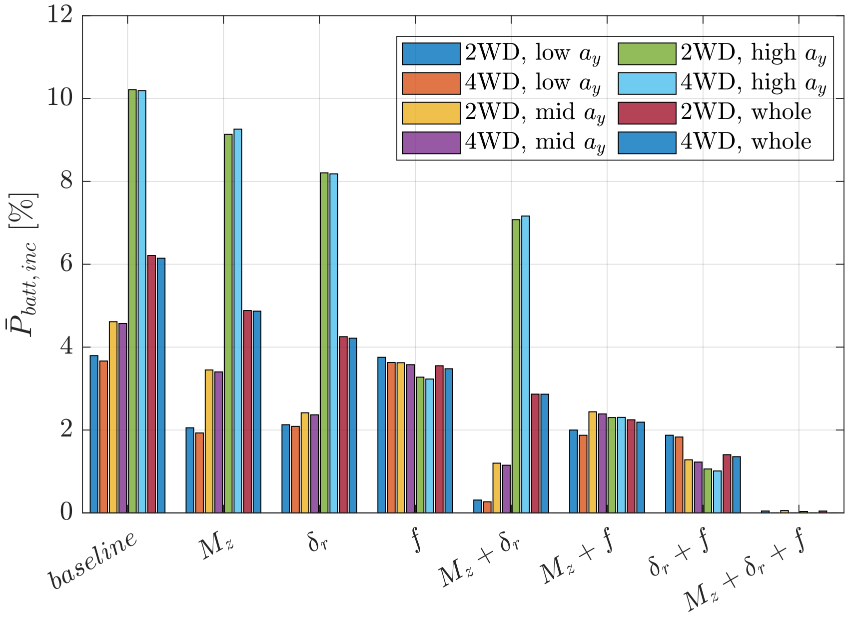

Figure 2.12: Average power increase, relative to the power of the 4WD set-up with $M_z + \delta_r + f$, for distinct bands of lateral acceleration, namely 1-3 m/s^2 (low a_y), 3-5 m/s^2 (mid a_y), 5-7 m/s^2 (high a_y), and 1-7 m/s^2 (whole). $V = 100$ km/h, $\mu_{\%} = 100\%$ and $a_x = 0$ m/s^2.

order in terms of average battery power increase. Moreover, the cumulative perspective given by the histograms reveals that, generally, the 4WD is moderately more efficient than the 2WD at low and mid lateral accelerations, but at high lateral accelerations the situation may reverse owing to the front axle engagement effect described previously.

An alternative viewpoint on the same results is provided by Fig. 2.13, which displays the average battery power increase relative to the power consumption of the 2WD baseline set-up. In other words, $P_{batt,ref}$ in (2.24) is the power profile of the 2WD baseline set-up. Of course, this is the least effective configuration in terms of power usage reduction, hence $\bar{P}_{batt,inc}$ is always negative. The figure in question testifies once again the substantial power reduction achievable at high lateral accelerations through

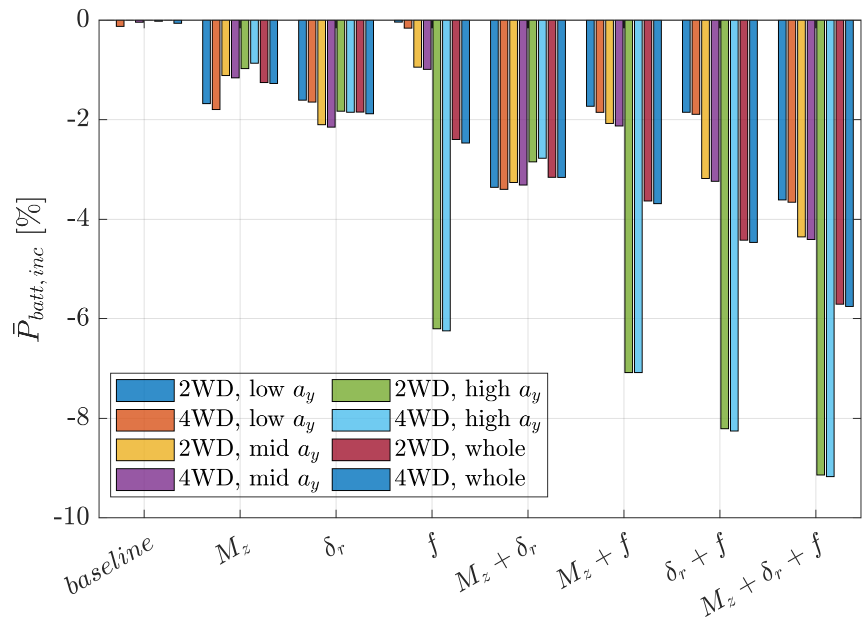

Figure 2.13: Average power increase, relative to the power of the 2WD baseline set-up, for distinct bands of lateral acceleration, namely 1-3 m/s^2 (low a_y), 3-5 m/s^2 (mid a_y), 5-7 m/s^2 (high a_y), and 1-7 m/s^2 (whole). $V = 100$ km/h, $\mu_{\%} = 100\%$ and $a_x = 0$ m/s^2.

f: the decrease always exceed 6%, and reaches ~9% for $M_z + \delta_r + f$. Moreover, on average, M_z and δ_r can ensure similar power reductions (~1.8%) within the low range, but then, in the mid range, power reduction of δ_r (about 2%) is approximately twice that of M_z. Therefore, based on this, it is possible to state that, in normal driving conditions, rear-wheel steering is the most energy-efficient single actuation.

The second set of results, which is condensed in Fig. 2.14 and 2.15, is obtained in the presence of longitudinal acceleration $a_x = 1.5$ m/s^2 (see Section 2.3.2 for the meaning of a_x in this context). Above all, the additional load required to perform the manoeuvre translates to a very net separation between the 2WD and 4WD lines. This confirms that at higher torque demands it is considerably more indicated to deliver the

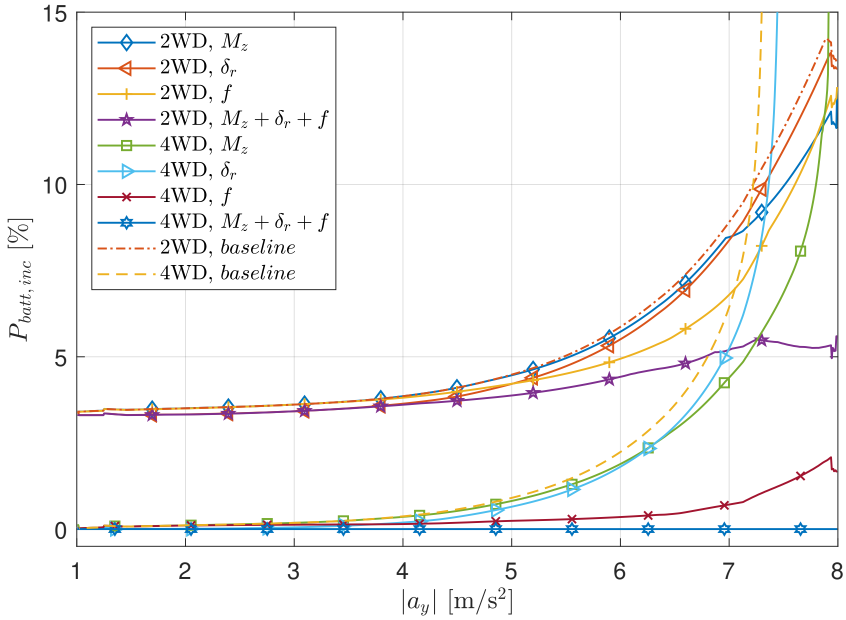

Figure 2.14: Relative profile of minimum power along the energy-efficient understeer characteristic. Single actuations. $V = 100$ km/h, $\mu_{\%} = 100\%$ and $a_x = 1.5$ m/s^2.

torque also to the front motors. In fact, in the present conditions, the rule-based strategy in (2.12) for allocating the torque between the two motors of the same side permits to reduce power used of 3% relative to that of the 2WD counterpart. By focusing on the single actuations in Fig. 2.14, it is noticeable that, though the curves still exhibit the same features highlighted in the absence of longitudinal acceleration, at low lateral accelerations the gap between the lines of the same drivetrain is significantly smaller to the extent that power saving capabilities of the actuations are essentially negligible. Moreover, anti-roll moment distribution via active suspensions still guarantees significant advantages at high lateral accelerations, especially in conjunction with the 4WD architecture.

Fig. 2.15 depicts also the lines concerning the pairs of actuations. Again, the key to the reading given for the homologous lines in case of zero a_x is still valid for

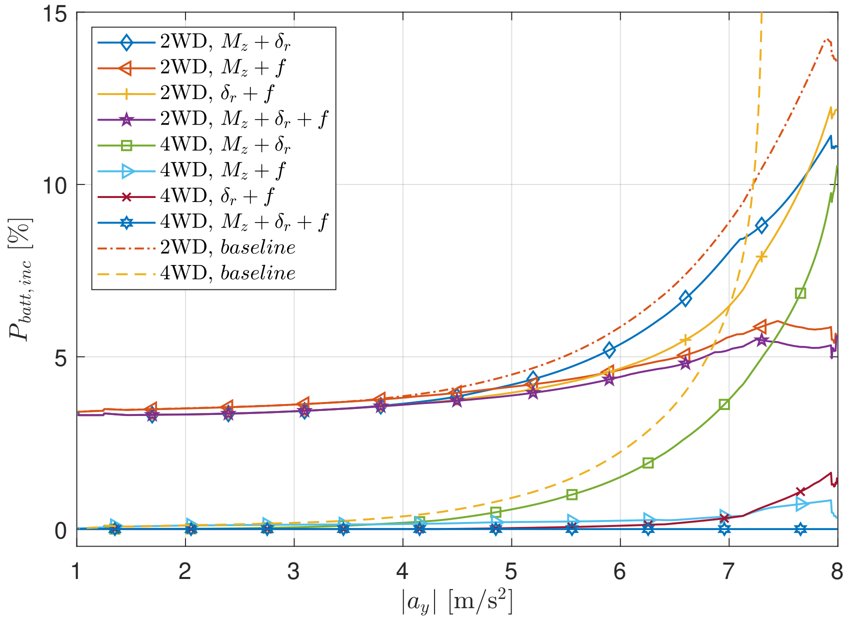

Figure 2.15: Relative profile of minimum power along the energy-efficient understeer characteristic. Multiple actuations. $V = 100$ km/h, $\mu_{\%} = 100\%$ and $a_x = 1.5$ m/s^2.

the 4WD, whereas further considerations are needed for to the 2WD. Indeed, if the active longitudinal torque distribution is missing, the pair $\delta_r + f$ becomes notably less favourable then the couple $M_z + f$ while approaching the lateral acceleration limit.

Additionally, summary bar plots are reported in Fig. 2.16. The histograms confirm the clear decoupling between the battery power consumptions as the longitudinal torque distribution strategy changes. In fact, for each lateral acceleration band, the bar related to the 2WD is higher than the one of the 4WD, which translates to a higher average power usage for the 2WD layout.

Fig. 2.17 provides an alternative perspective on the same results: the average power increment is relative to the power usage of the 2WD baseline set-up. Only in the presence of f as a single or combined actuation power saving relative to the 2WD baseline consumption can exceed 5%.

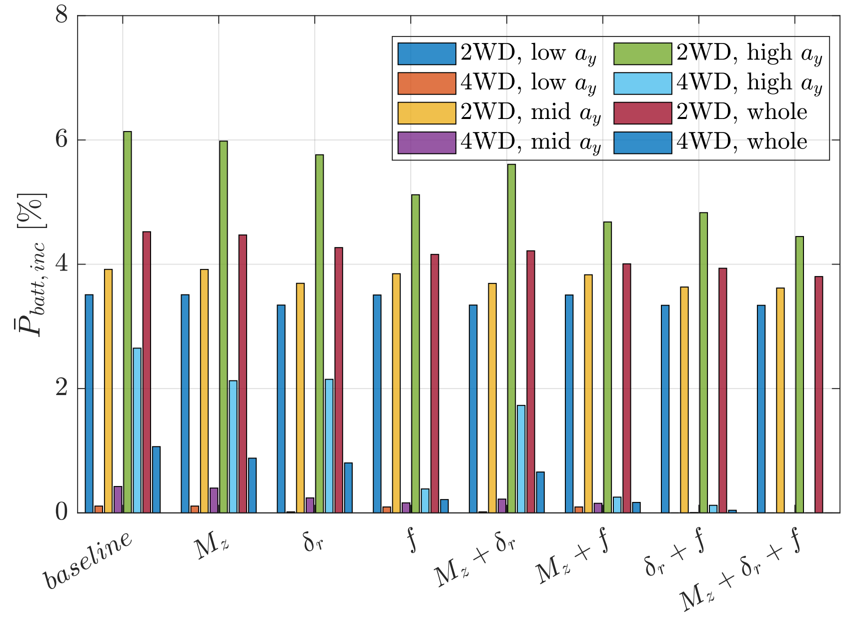

Figure 2.16: Average power increase, relative to the power of the 4WD set-up with $M_z + \delta_r + f$, for distinct bands of lateral acceleration, namely 1-3 m/s^2 (low a_y), 3-5 m/s^2 (mid a_y), 5-7 m/s^2 (high a_y), and 1-7 m/s^2 (whole). $V = 100$ km/h, $\mu_{\%} = 100\%$ and $a_x = 1.5$ m/s^2.

Finally, a selection of figures related to other test conditions is presented in Appendix C. Key findings are still valid to interpret the additional plots. However there are some peculiar features that require additional comments. Indeed, at 50 km/h the minimum power envelope given by M_z as a single actuation has a U-shaped cross-section rather than the W-shaped one observed at higher speed, and at low lateral accelerations the most efficient understeer characteristic coincides with the baseline. This is consistent with the trends in Fig. C.1 and C.5, where also M_z curves branch out from the baselines. Of course, because of the limited effect of active suspensions at low a_y values, the same trend is displayed by $M_z + f$ in Fig. C.2 and C.6. Furthermore, it is worth stressing that the bump that can be observed at medium lateral accelerations in

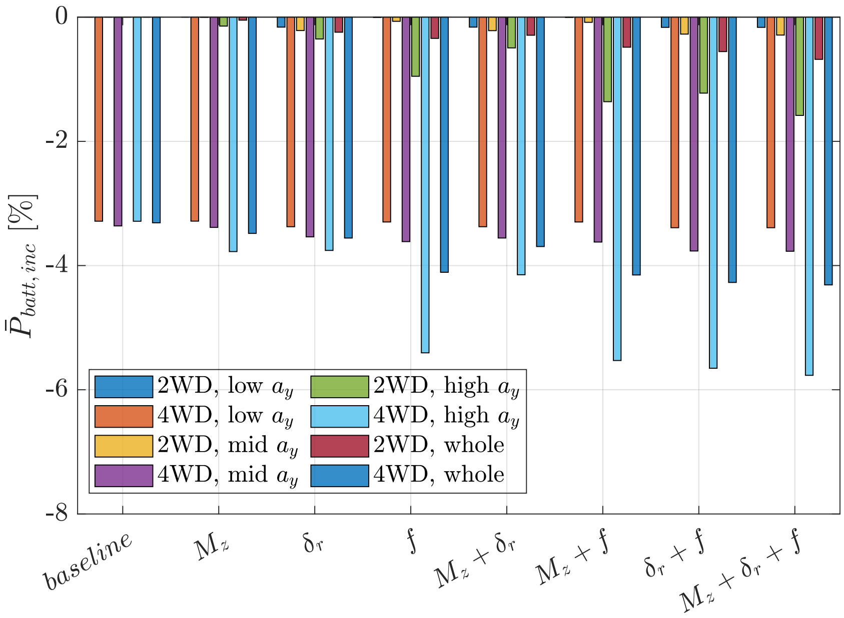

Figure 2.17: Average power increase, relative to the power of the 2WD baseline set-up, for distinct bands of lateral acceleration, namely 1-3 m/s^2 (low a_y), 3-5 m/s^2 (mid a_y), 5-7 m/s^2 (high a_y), and 1-7 m/s^2 (whole). $V = 100$ km/h, $\mu_{\%} = 100\%$ and $a_x = 1.5$ m/s^2.

the aforementioned figures is essentially due to a discontinuity in the energy-efficient curves of $M_z + \delta_r + f$, which affects the other curves in relative terms. Finally, if $V = 50$ km/h and $a_x = 1.5$ m/s^2, the reduction of power used by 4WD vehicle is approximately 6% relative to the one of the 2WD counterpart (see Fig. C.3, C.4, C.7 and C.8).

2.5.3 Relative profile of minimum power along arbitrary understeer characteristics

Special attention has been devoted so far to the optimal understeer characteristics. However, as already highlighted, the most energy-efficient curve may show an erratic behaviour which may be unacceptable from the drivability viewpoint or even hardly achievable in practice. These considerations set the scene for the analysis presented below. In particular, the power consumption is assessed along a selection of understeer characteristics which are more likely to be attained in the real world than some optimal understeer characteristics. The four curves that are adopted for the following analysis are depicted in Fig. 2.18. Precisely, curve (i) is the baseline of the 2WD set-up in case $V = 100$ km/h, $\mu_{\%} = 100\%$ and $a_x = 0$ m/s^2. Curve (ii) is chosen as an example of characteristic providing a lower level of understeer, compared to (i). Curve (iv) is the baseline of the 2WD set-up in case $V = 100$ km/h, $\mu_{\%} = 100\%$ and $a_x = 1.5$ m/s^2. Curve (iii) is picked as an example of characteristic giving a higher level of understeer, compared to (iv).

Therefore, the ultimate purpose of the current analysis is evaluating the minimum power consumption in connection with a given control allocation for achieving a desired cornering response which is not potentially the most energy efficient across the whole range of lateral accelerations. In particular, battery power is expressed in terms of battery power increase ($P_{batt,inc}$) according to the equation

$$P_{batt,inc}\left(a_y\right) = \left(\frac{P_{batt,min}\left(a_y\right) - P_{batt,ref}\left(a_y\right)}{P_{batt,ref}\left(a_y\right)}\right) \cdot 100 \tag{2.25}$$

where $P_{batt,min}$ is the power provided by the minimum power envelope of a given combination of actuations along the selected arbitrary understeer characteristic, and $P_{batt,ref}$ is a reference power profile.

Owing to the arbitrary nature of the selected curves, these may not lie entirely within the bounds of a given minimum power envelope, thus incomplete power profiles may be retrieved. This is the case of the narrow envelopes typically produced by M_z and by f as single as well as combined actuations. This observation explains the omission of the related partial profiles from the following figures.

Fig. 2.19 shows the battery power increase along curve (ii) of Fig. 2.18 in case $V = 100$ km/h, $\mu_{\%} = 100\%$ and $a_x = 0$ m/s^2. $P_{batt,ref}$ is equal to the $P_{batt,opt}$ (see Section 2.5.1 for its definition) provided by the 4WD set-up with $M_z + \delta_r + f$. Because of the choice of the reference curve, all the lines are greater than zero throughout the domain. As can be seen, once more the profiles produced by the two drivetrains

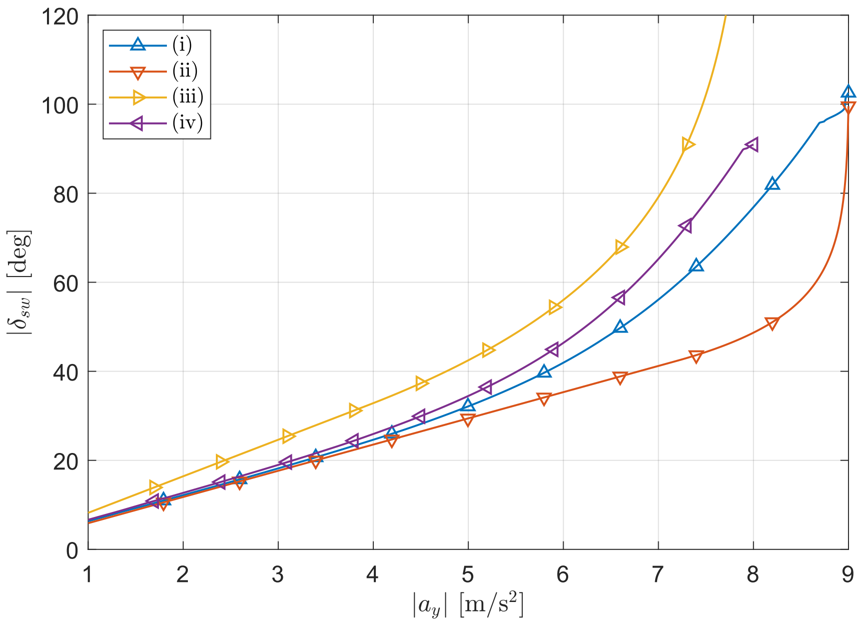

Figure 2.18: Curves along which the minimum battery power is fetched. Specifically, (i) is the 2WD baseline described in case of zero longitudinal acceleration; (ii) is the selected curve with a lower level of understeer than the baseline; (iii) is the selected curve with a higher level of understeer than the baseline; (iv) is the 2WD baseline in the presence of longitudinal acceleration equal to 1.5 m/s^2.

are essentially overlapped on the whole range of a_y, which is the same behaviour observed in Fig. 2.10 and Fig. 2.11. The negligible effect of the active suspensions at low lateral accelerations translates to the fact that the lines concerning $\delta_r + f$ detach from the curves related to δ_r as a single actuation. For the same reason, $M_z + \delta_r$ curves branch out from $M_z + \delta_r + f$ lines. It is interesting to rediscover that, compared to the other actuations, the active distribution of the anti-roll moment is considerably more advantageous at medium-to-high lateral accelerations. Moreover, the figure demonstrates that by describing the selected arbitrary curve, the triple combination of actuations brings a power consumption increase that is confined within ~2%.

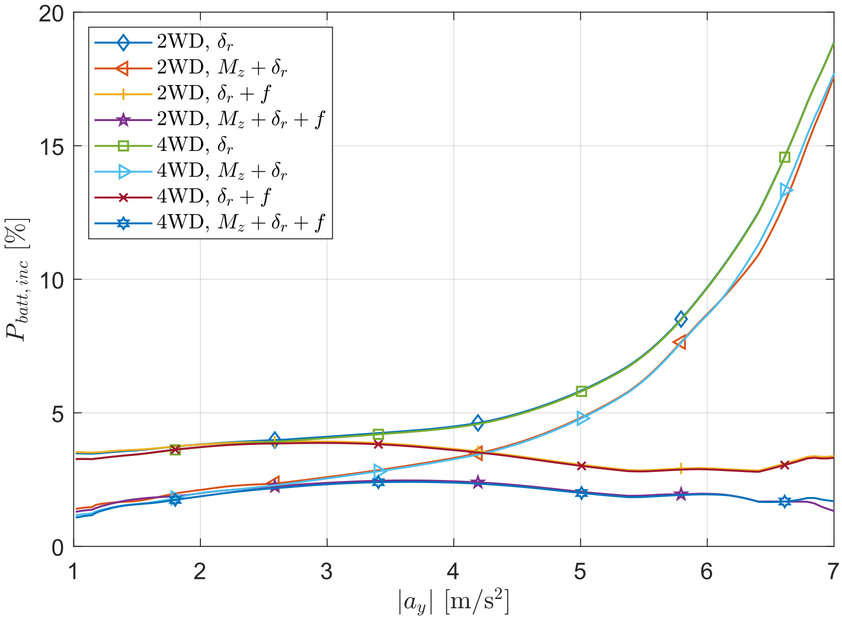

Figure 2.19: Relative profile of minimum power along understeer characteristic (ii) depicted in Fig. 2.18. $V = 100$ km/h, $\mu_{\%} = 100\%$ and $a_x = 0$ m/s^2. Incomplete curves are omitted.

Fig. 2.20 aims to highlight the effects of the positive longitudinal acceleration across curve (iii) of Fig. 2.18 in case $V = 100$ km/h, $\mu_{\%} = 100\%$ and $a_x = 1.5$ m/s^2. Again, $P_{batt,ref}$ coincides with the $P_{batt,opt}$ given by the 4WD set-up with $M_z + \delta_r + f$. In this figure it is possible to notice the same separation of the 2WD and 4WD curves that characterised Fig. 2.14 and Fig. 2.15. Furthermore, the trends discussed previously are still present. However, as can be seen clearly, the power consumption increase is almost negligible in the presence of 4WD layout and f. Also, the power increase is always greater than 3% if only the rear axle is driven.

Further considerations can be given by examining the average battery power increase across curve (i) of Fig. 2.18 in case $V = 100$ km/h, $\mu_{\%} = 100\%$ and $a_x = 0$ m/s^2. At this purpose, Fig. 2.21a depicts the mean power increase of the different

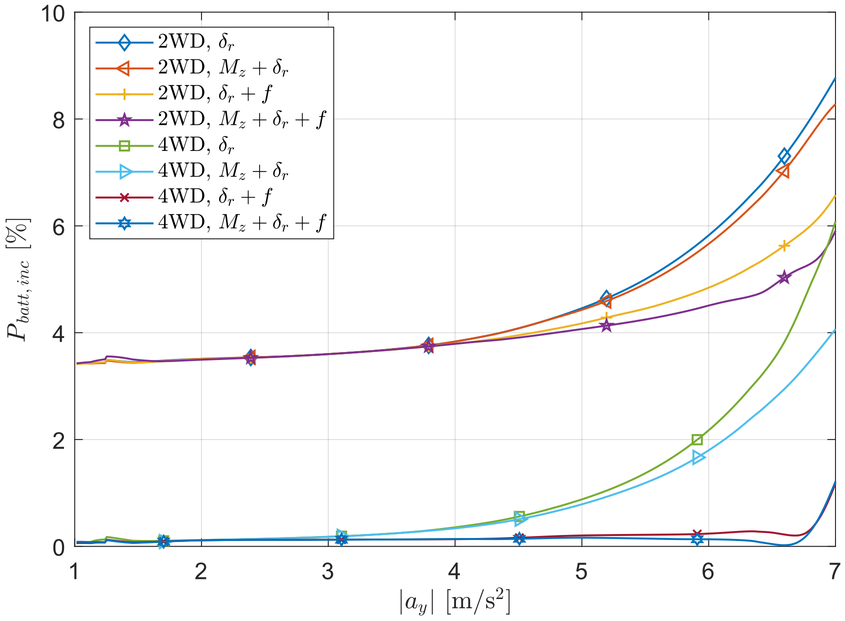

Figure 2.20: Relative profile of minimum power along understeer characteristic (iii) depicted in Fig. 2.18. $V = 100$ km/h, $\mu_{\%} = 100\%$ and $a_x = 1.5$ m/s^2. Incomplete curves are omitted.

combinations of actuations relative to their respective $P_{batt,opt}$. Whereas, Fig. 2.21b displays the mean power increase relative to the power of the baseline set-up with the architecture in question.

Firstly, consider Fig. 2.21a. As a matter of fact, this figure provides an aggregate perspective of the same piece of information supplied by the so-called carpets described in Section 2.5.1. Thus, the main findings can be summarised as follows:

- Generally, with the exclusion of M_z, f and $M_z + f$, the average power increase is around 2% for all a_y bands.

- The average power increase with respect to M_z approaches 2% at low lateral acceleration and is around 1% elsewhere.

- As a product of the marginal authority of active suspensions in the presence of limited lateral accelerations, the average power increase related to f is essentially zero in the range 1-3 m/s^2 and about 1% between 3 and 5 m/s^2; however, at higher lateral accelerations, the actuation manifests a substantial increase that exceeds 6%. The trend confirms the remarkable energy-saving potentialities of active suspensions while describing the energy-efficient understeer characteristic in place of the baseline.

- The average power increase with respect to $M_z + f$ is clearly influenced by M_z at low lateral accelerations and by f at high a_y values.

Secondly, consider Fig. 2.21b. Clearly, in case of single actuations, the set of extended understeer characteristics constitutes a surface (rather than a volume); therefore, power increase along (i) must be null for M_z, δ_r and f. And, owing to the substantial coincidence of cornering response of 2WD and 4WD (which was observed in Section 2.5.2), the average power increment must be zero for both drivetrain layouts. Conversely, multiple actuations, by virtue of a proper control allocation, allow the vehicle to describe the same understeer characteristic while reducing the power usage. Hence, the figure reveals that, among the double actuations, $M_z + \delta_r$ prevails in term of energy-efficiency at low-to-medium lateral accelerations. Moreover, there exists a great authority of $\delta_r + f$ at high lateral accelerations, providing an average power reduction of ~6.5%. Conversely, power saving potentialities of $M_z + f$ are rather limited in this scenario. Finally, in case of triple actuation, the average power decrease even approaches 8% in the band 5-7 m/s^2, which is considerable.

A similar analysis can be performed in case $V = 100$ km/h, $\mu_{\%} = 100\%$ and $a_x = 1.5$ m/s^2. Hence, Fig. 2.22 collects the average power increase along curve (iv) of Fig. 2.18. Reference power profiles are analogous to those related to Fig. 2.21.

As can be observed in Fig. 2.22a, $\bar{P}_{batt,inc}$ is generally bounded within 0.5%. The only exceptions are represented by f and $M_z + f$. This demonstrates that, also in case of longitudinal acceleration equal to 1.5 m/s^2, f alone or in conjunction with TV perform significantly better as long as the vehicle cornering response is altered.

In conclusion, consider Fig. 2.22b. Firstly, note that there exists a marginal average power reduction also in case of single actuations in tandem with 4WD because curve (iv) is provided by the 2WD set-up, and this understeer characteristic is slightly different from that of the 4WD counterpart. Secondly, in respect of $M_z + \delta_r$ and $M_z + f$, only 4WD can provide some minor benefits in the range 5-7 m/s^2. Finally, likewise in the absence of longitudinal acceleration, energy-saving potentialities of the pair $\delta_r + f$ are reaffirmed at high lateral accelerations; for an even stronger reason, $\delta_r + f$ is effective if supported by TV as demonstrated by the histograms with respect to $M_z + \delta_r + f$.

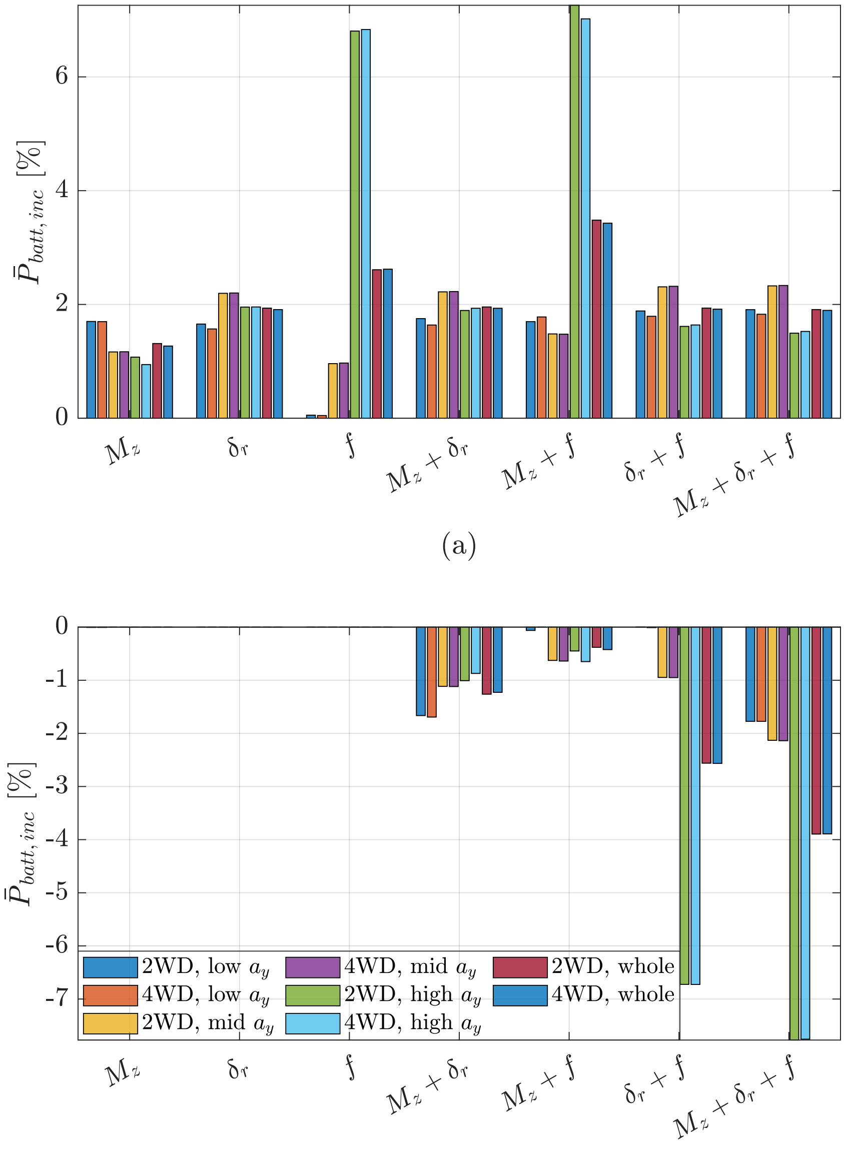

(a)

(b)

Figure 2.21: Average power increase across curve (i) of Fig. 2.18 for distinct lateral acceleration bands. Ranges are 1-3 m/s^2 (low a_y), 3-5 m/s^2 (mid a_y), 5-7 m/s^2 (high a_y), and 1-7 m/s^2 (whole). $V = 100$ km/h, $\mu_{\%} = 100\%$ and $a_x = 0$ m/s^2. In (a) the average power increase of each combination of actuations is relative to the respective $P_{batt,opt}$. In (b) the average power increase is relative to the power of the baseline set-up with the architecture in question.

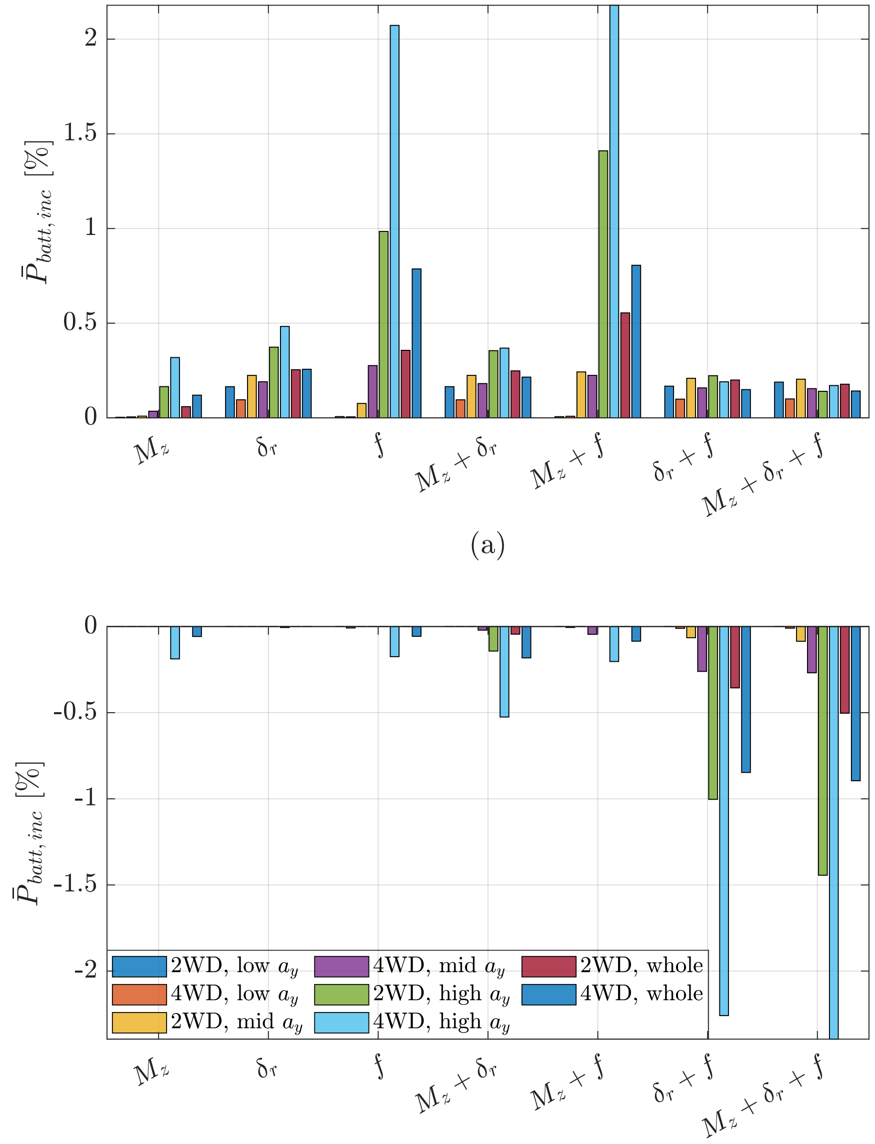

(a)

(b)

Figure 2.22: Average power increase across curve (iv) of Fig. 2.18 for distinct lateral acceleration bands. Ranges are 1-3 m/s^2 (low a_y), 3-5 m/s^2 (mid a_y), 5-7 m/s^2 (high a_y), and 1-7 m/s^2 (whole). $V = 100$ km/h, $\mu_{\%} = 100\%$ and $a_x = 1.5$ m/s^2. In (a) the average power increase of each combination of actuations is relative to the respective $P_{batt,opt}$. In (b) the average power increase is relative to the power of the baseline set-up with the architecture in question.

2.6 Conclusion

In conclusion, each single or combined actuation exhibits persistent and recurrent trends which can be summarised as follows.

- Energy-efficient understeer characteristics produced by the single actuations exhibit clear trends:

    1. with respect to torque vectoring, the optimal curve is generally close to the baseline throughout the domain. The tendency testifies that the introduction of an direct yaw moment via TV brings tyre slip power losses reduction on the one hand, but it imposes a higher workload to the powertrains. Overall, torque vectoring as a single actuation exhibits a minimum in terms of power consumption for relatively mild direct yaw moment values and becomes very inefficient as M_z values grow. This translates to the fact that torque vectoring enforces a choice between energy-efficiency enhancement and cornering response shaping.
    2. in respect to rear-wheel steering, the energy efficient understeer characteristic is essentially located in the high end of $a_y\delta_{sw}$-plane, which corresponds to in-phase steering. In fact, this feature is viable to reduce the tyre slip power losses;
    3. with respect to anti-roll moment distribution, the energy efficient understeer characteristic is essentially located in the low end of $a_y\delta_{sw}$-plane, which corresponds to a less understeering than the baseline behaviour. This trends is such that it puts the tyres in a better operating condition.

- Anti-roll moment distribution via active suspensions is ineffective up to mid lateral accelerations because of the limited load shift, but it is significantly beneficial at medium-to-high lateral accelerations. Its advantages are typically higher that those offered by rear-wheel steering and torque vectoring as single actuations. With respect to the anti-roll moment distribution, there exists a wide region in the $a_y\delta_{sw}$-plane, located below the baseline, that ensures power usage reduction relative to the base understeer characteristic. Hence, the presence of such an extensive area makes possible to shape at will the vehicle cornering response while decreasing the power usage thanks to the better operating condition of tyres and powertrains. In other words, it is feasible to increase the degree of sportiness and enhance the energy saving at the same time.

- In normal driving conditions, i.e. up to medium lateral accelerations and in case of negligible longitudinal accelerations, torque vectoring and, even more, rear-wheel steering on their own can be exploited factually for energy saving purposes, providing power saving relative to the power of the baseline configuration up to ~3%; at higher lateral accelerations, their performance degrades significantly, to the point that even along the energy-efficient understeer characteristic power usage reduction is very limited.

- Based also on the previous point, when it comes to double actuations, $M_z + \delta_r$ can supply significant power saving (up to ~4% relative to the power of the baseline set-up) at low-to-mid lateral accelerations, whilst $M_z + f$ and $\delta_r + f$ generally outperform the former by virtue of the substantial contribution of active front-to-total anti-roll moment distribution.

- In the presence of longitudinal acceleration, there exists a net separation between 2WD and 4WD power consumptions. In fact, by taking advantage of a 4WD architecture in conjunction with a proper front-to-total motor torque distribution strategy, battery power usage can be reduced from ~3% to ~6% (depending mainly on vehicle speed) relative to the 2WD counterpart.

- Multiple actuations can be utilised factually to decrease the power consumption while describing arbitrary understeer characteristics. Along the baseline curve and in the absence of longitudinal acceleration, the combination $M_z + \delta_r$ can provide, on average over the whole lateral acceleration range, more than 1% of battery power decrease relative to the power used by the baseline set-up. Similarly, the power usage decrease can reach ~2.5% on a vehicle equipped with δ_r and f. Interestingly, $M_z + f$ displays a marginal power saving authority in this scenario. Analogous trends, though with much lower average power saving, can be observed in the presence of the additional workload enforced by the longitudinal acceleration.

Chapter 3

Energy-efficient torque vectoring and anti-roll moment control

3.1 Introduction

Torque vectoring (TV) is a control strategy characterised by individual driving and braking wheel torque allocation. In the last decades, the technique has gained great interest thanks to the growing spread of electric vehicles with independent powertrains, which lend themselves specially to this control programme.

The benefits provided by TV are multiple. Firstly, it allows to shape vehicle cornering response via reference yaw rate tracking, thus manipulating the relationship between lateral acceleration and steering wheel angle. Secondly, TV provides enhanced performance in extreme transient conditions in terms of yaw rate stabilisation and sideslip angle restriction, also thanks to the high torque bandwidth of the electric drives. Thirdly, torque vectoring can be useful to increase the overall energy-efficiency of the vehicle through longitudinal and lateral tyre slip power losses minimisation.

The aforementioned assets uncovered by individual wheel torque modulation have been widely inspected in the literature and several dynamic controls based on TV have been proposed in the years. [123] presented a single input single output (SISO) direct yaw moment control to enhance the safety and handling qualities of an electric vehicle with independent powertrains. Tyre slip minimisation while fulfilling the stability constraints is addressed by [124] through a fast model predictive torque control for distributed drive electric vehicles. [125] described a robust linear quadratic regulator (RLQR) for improving the direct yaw moment control. Some authors proposed also powerful strategies based on linear [39, 38] and nonlinear [126, 127] model predictive controls (MPC and NMPC, respectively) which aim to stabilise the vehicle and restrain the sideslip angle also at the limit of handling. [37] proposed an LQR-based torque vectoring control that strives to optimise the energy-efficiency by including the powertrain power losses in the cost function. Energy-efficient torque allocation is addressed also by [22, 23, 24, 128]. Within the framework of energy-efficient control allocation, [21, 26, 25] demonstrated that remarkable energy-saving benefits can be derived via TV control by imposing the tracking of a properly shaped understeer characteristic, i.e the so-called energy-efficient understeer characteristic extensively discussed in Chapter 2.

Parallelly to TV, active suspension (AS) control represents a powerful and versatile technique for modern passenger cars. AS can be utilised for controlling the motion of the sprung mass induced by longitudinal and lateral acceleration or by road irregularities both for dynamic and comfort purposes. Actually, as put in evidence in the previous chapter, AS also allows the distribution of anti-roll moment between the front and rear axles. Indeed, in cornering, by increasing the anti-roll moment contribution and, consequently, the lateral load transfer within the axle, the lateral axle force tends to decrease for a given sideslip angle. Therefore, by adjusting the anti-roll moment allotment between the two axles, it is possible to influence the degree of understeer of the vehicle. By way of example, the increase of the anti-roll moment on the front axle and/or a decrease on the rear axle result into increased understeer; vice versa, increased anti-roll moment distribution towards the rear axle reduces understeer. The effect can be exploited for yaw rate tracking and sideslip angle limitation, likewise to TV, provided that the lateral load transfer is appreciable. In fact, as observed also in Chapter 2, anti-roll moment distribution is essentially ineffective at low lateral accelerations.

Similarly to torque vectoring, dynamic controls based on active suspensions for yaw moment tracking and handling improvement cover a notable slice of literature [20, 115, 129, 118, 130, 116]. A remarkable example is [116], in which the authors presented a linearised feedback-feedforward anti-roll moment distribution strategy for yaw rate tracking based on a proportional-integral (PI) and H_∞ controller.

However, in contrast with TV, the control of roll-moment distribution via active suspensions has been explored scarcely from an energy-efficiency viewpoint and the available studies are limited to the energy recovery capabilities offered by the suspension actuators as presented by [30]. However, as shown in Chapter 2, front-to-total anti-roll moment distribution can influence positively the energy-efficiency of a vehicle since it can mitigate significantly the tyre slip power losses and so the total power usage.

Moreover, integrated TV and active suspension control can improve the cornering response and energy efficiency compared to the independent control of the actuators. In fact, literature hosts an exiguous number of works on controllers based on torque allocation in tandem with active anti-roll moment distribution, albeit not for energy-saving purposes. One of the few examples is [122], which proposed a concurrent actuation of active aerodynamics, active rear steering, torque vectoring, and hydraulically interconnected suspensions. However there is no integration of the controllers and the advanced hydraulic layout of the suspensions is in fact a passive system. [129] presented a strategy in which there are distinct feedback controllers for imposing the desired direct yaw moment and reference front-to-total anti-roll moment distribution; both contributions are based on the same reference yaw rate. [131] proposed a set of distinct controllers for active suspensions, direct yaw moment and active front-wheel steering that are integrated in a single framework. Other studies presented simplified models to determine the active front and rear anti-roll moment contributions. For instance, [132] describes a simplified model, in which the lateral tyre force is a linear function of the sideslip angle, to compute the anti-roll moments required to track the reference yaw rate; dissipative brakes intervene if the active suspensions contribution is not enough. Conversely, an empirical approach is adopted in [133]: front and rear anti-roll moments are so that their difference is directly proportional to the one between the front and rear sideslip angles.

Definitely, to the best knowledge of the author, there exists a literature gap regarding the integrated and optimal model based control of wheel torque and anti-roll moment distribution. A fortiori, no research presents the aforementioned strategies for vehicle handling and stability enhancement together with energy consumption minimisation. Therefore, the novelty of the present study consists in the development of an integrated energy-efficient nonlinear model predictive control to manage both the wheel torque allocation and the anti-roll moment distribution. To make this possible, the internal model includes the roll dynamics and a reduced Pacejka's tyre model that exhibits a nonlinear dependence of the lateral force on the vertical load. Furthermore, the case study vehicle is equipped with four in-wheel-motors (IWM) and active suspension actuators: its main parameters are listed in Table 2.1. The controller capabilities are assessed by making use of a high-fidelity and experimentally validated simulation model.

3.2 Internal model equations

The internal model adopted for this analysis has 8 degrees of freedom. Essentially, it is the planar model derived in Section 1.3.1 with the addition of wheel and roll dynamics. Specifically, the following equations are included.

- Longitudinal force balance

$$ma_x = \sum_{i,j} F_{x,ij} \cos(\delta_{ij}) - \sum_{i,j} F_{y,ij} \sin(\delta_{ij}) - F_{drag} \tag{3.1}$$

- Lateral force balance

$$ma_y = \sum_{i,j} F_{x,ij} \sin(\delta_{ij}) + \sum_{i,j} F_{y,ij} \cos(\delta_{ij}) \tag{3.2}$$

- Yaw moment balance

$$\begin{aligned}J_z\ddot{\psi} =& a_f\left[F_{x,fl}\sin\left(\delta_{fl}\right)+F_{y,fl}\cos\left(\delta_{fl}\right)\right]+a_f\left[F_{x,fr}\sin\left(\delta_{fr}\right)+F_{y,fr}\cos\left(\delta_{fr}\right)\right]\\ &-a_r\left[F_{x,rl}\sin\left(\delta_{rl}\right)+F_{y,rl}\cos\left(\delta_{rl}\right)\right]-a_r\left[F_{x,rr}\sin\left(\delta_{rr}\right)+F_{y,rr}\cos\left(\delta_{rr}\right)\right]\\ &-\frac{b_f}{2}\left[F_{x,fl}\cos\left(\delta_{fl}\right)-F_{y,fl}\sin\left(\delta_{fl}\right)\right]+\frac{b_f}{2}\left[F_{x,fr}\cos\left(\delta_{fr}\right)-F_{y,fr}\sin\left(\delta_{fr}\right)\right]\\ &-\frac{b_r}{2}\left[F_{x,rl}\cos\left(\delta_{rl}\right)-F_{y,rl}\sin\left(\delta_{rl}\right)\right]+\frac{b_r}{2}\left[F_{x,rr}\cos\left(\delta_{rr}\right)-F_{y,rr}\sin\left(\delta_{rr}\right)\right]\end{aligned} \tag{3.3}$$

- Roll moment balance

$$\begin{aligned}&J_x\ddot{\varphi}=ma_y\left[h_{\mathrm{CG}}-h_{\mathrm{roll}}\right]\cos\left(\varphi\right)+mg\left[h_{\mathrm{CG}}-h_{\mathrm{roll}}\right]\sin\left(\varphi\right)\\ &-M_{AR,PS,f}-M_{AR,PS,r}-M_{AR,PD,f}-M_{AR,PD,r}-M_{AR,Act,f}-M_{AR,Act,r}\end{aligned} \tag{3.4}$$

- ij wheel moment balance, where the subscript $i=f,r$ designates the front or rear axle, whereas $j=l,r$ specifies the left-hand or right-hand side,

$$J_{w,ij}\dot{\Omega}_{ij}=T_{ij}-F_{x,ij}R-M_{y,ij} \tag{3.5}$$

in which m is the vehicle mass; V is the speed magnitude of the centre of mass; β is the sideslip angle; ψ is the yaw angle; F_{drag} is the aerodynamic drag force, namely

$$F_{drag}=\frac{1}{2}\rho_{air}AC_d\left(V\cos\left(\beta\right)\right)^2 \tag{3.6}$$

where ρ_{air} is the air density, A is the vehicle frontal cross-section and C_d is the drag coefficient; $F_{x,ij}$ and $F_{y,ij}$ are, respectively, the longitudinal and lateral tyre forces of the ij wheel expressed in the wheel reference frame; δ_{ij} is the steering angle of the ij wheel (comprehensive of the relative toe angle); J_z is the yaw mass moment of inertia of the vehicle; a_f and a_r are the longitudinal distances, respectively, of the front and rear axles from the centre of gravity; b_f and b_r are the front and rear tracks; φ is the roll angle; J_x is the roll mass moment of inertia; h_{CG} is the height from the ground of the centre of gravity in static conditions; h_{roll} is the roll axis height from the ground at a longitudinal distance corresponding to the centre of gravity; g is the gravitational acceleration; $M_{AR,PS,f}$ and $M_{AR,PS,r}$ are, respectively, front and rear passive anti-roll

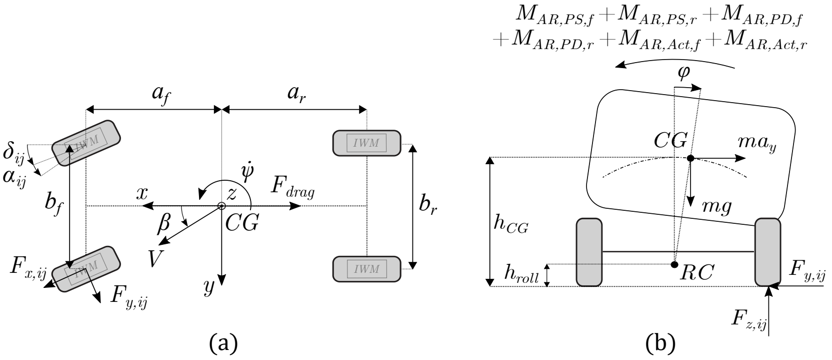

(a) (b)

Figure 3.1: Vehicle model schematic. (a) Top view. (b) Rear view.

moment contributions due to the passive springs and to the anti-roll bars; $M_{AR,PD,f}$ and $M_{AR,PD,r}$ are, respectively, front and rear passive anti-roll moment contributions due to the passive damping components; $M_{AR,Act,f}$ and $M_{AR,Act,r}$ are, respectively, front and rear active anti-roll moment contributions; Ω_{ij} is the rotational velocity of the ij wheel (which is the same as the motor speed in the considered direct drive IWMs); $J_{w,ij}$ is the wheel moment of inertia; T_{ij} is the wheel torque; R is the wheel radius; $M_{y,ij}$ is the rolling resistance torque, namely

$$M_{y,ij} = F_{z,ij}\left[k_0 + k_1(\Omega_{ij}R)^2\right]R \tag{3.7}$$

in which k_0 and k_1 are coefficients and $F_{z,ij}$ is the vertical load. The fundamental quantities and sign conventions are displayed in Fig. 3.1. Additionally, in braking conditions, wheel torque is split between the electric motors (T_{el}) and the dissipative system (T_{bk}) so that, for ij wheel,

$$T_{ij} = T_{el,ij} + T_{bk,ij} \tag{3.8}$$

Within the internal model, for each vehicle corner, the brake blending formulation prioritises regenerative braking over friction braking through the following smooth saturation, which approximates $T_{el,ij} = \max(T_{ij}, T_{el,min,ij})$, and is suitable for the numerical implementation:

$$T_{el,ij} = \frac{T_{ij} - T_{el,min,ij}}{1 + e^{-w_{ss}(T_{ij} - T_{el,min,ij})}} + T_{el,min,ij} \tag{3.9}$$

where $T_{el,min,ij} \leq 0$ is the minimum electric motor torque, and w_{ss} is a positive coefficient that defines the desired degree of smoothness. In a first approximation, the passive anti-roll moment contributions can be calculated as linearised functions of the roll angle and roll rate; precisely,

$$M_{AR,PS,i} = k_{s,i}\varphi \tag{3.10a}$$

$$M_{AR,PD,i} = k_{d,i}\dot{\varphi} \tag{3.10b}$$

where $k_{s,i}$ and $k_{d,i}$ are the stiffness and damping coefficients, respectively, of the i axle. Furthermore, the active anti-roll contributions are expressed as

$$M_{AR,Act,f} = fM_{AR,Act,Tot} \tag{3.11a}$$

$$M_{AR,Act,r} = [1-f]\,M_{AR,Act,Tot} \tag{3.11b}$$

where $f \in [0,1]$ is the front-to-total anti-roll moment distribution coefficient and $M_{AR,Act,Tot}$ is the total anti-roll moment contribution, which can be expressed as a function of the lateral acceleration a_y as

$$M_{AR,Act,Tot} = wma_y\,[h_{CG} - h_{roll}] \tag{3.12}$$

where w is a scaling coefficient that is tuned according to the desired roll angle characteristic. Note that the same approach was adopted in Chapter 2. Moreover, the longitudinal and lateral accelerations of the centre of mass are, respectively

$$a_x = \dot{V}\cos(\beta) - V\dot{\beta}\sin(\beta) - V\dot{\psi}\sin(\beta) \tag{3.13}$$

and

$$a_y = \dot{V}\sin(\beta) + V\dot{\beta}\cos(\beta) + V\dot{\psi}\cos(\beta) \tag{3.14}$$

Furthermore, the velocities of the wheel hubs, expressed in the wheel reference frame, are computed as follows. Longitudinal components are

$$v_{x,fl} = \cos\left(\delta_{fl}\right)\left[V\cos(\beta) - \frac{b_f}{2}\dot{\psi}\right] + \sin\left(\delta_{fl}\right)\left[V\sin(\beta) + a_f\dot{\psi}\right] \tag{3.15}$$

$$v_{x,fr} = \cos\left(\delta_{fr}\right)\left[V\cos\left(\beta\right) + \frac{b_f}{2}\dot{\psi}\right] + \sin\left(\delta_{fr}\right)\left[V\sin\left(\beta\right) + a_f\dot{\psi}\right] \tag{3.16}$$

$$v_{x,rl} = \cos\left(\delta_{rl}\right)\left[V\cos\left(\beta\right) - \frac{b_r}{2}\dot{\psi}\right] + \sin\left(\delta_{rl}\right)\left[V\sin\left(\beta\right) - a_r\dot{\psi}\right] \tag{3.17}$$

$$v_{x,rr} = \cos\left(\delta_{rr}\right)\left[V\cos\left(\beta\right) + \frac{b_r}{2}\dot{\psi}\right] + \sin\left(\delta_{rr}\right)\left[V\sin\left(\beta\right) - a_r\dot{\psi}\right] \tag{3.18}$$

Whereas, side components are

$$v_{y,fl} = -\sin\left(\delta_{fl}\right)\left[V\cos\left(\beta\right) - \frac{b_f}{2}\dot{\psi}\right] + \cos\left(\delta_{fl}\right)\left[V\sin\left(\beta\right) + a_f\dot{\psi}\right] \tag{3.19}$$

$$v_{y,fr} = -\sin\left(\delta_{fr}\right)\left[V\cos\left(\beta\right) + \frac{b_f}{2}\dot{\psi}\right] + \cos\left(\delta_{fr}\right)\left[V\sin\left(\beta\right) + a_f\dot{\psi}\right] \tag{3.20}$$

$$v_{y,rl} = -\sin\left(\delta_{rl}\right)\left[V\cos\left(\beta\right) - \frac{b_r}{2}\dot{\psi}\right] + \cos\left(\delta_{rl}\right)\left[V\sin\left(\beta\right) - a_r\dot{\psi}\right] \tag{3.21}$$

$$v_{y,rr} = -\sin\left(\delta_{rr}\right)\left[V\cos\left(\beta\right) + \frac{b_r}{2}\dot{\psi}\right] + \cos\left(\delta_{rr}\right)\left[V\sin\left(\beta\right) - a_r\dot{\psi}\right] \tag{3.22}$$

Consequently, the longitudinal and lateral slip velocities of the wheels are, respectively,

$$v_{x,slip,ij} = v_{x,ij} - \Omega_{ij}R \tag{3.23}$$

$$v_{y,slip,ij} = v_{y,ij} \tag{3.24}$$

and the longitudinal slip ratio and lateral slip angle are defined, respectively, as

$$\sigma_{ij} = -\frac{v_{x,slip,ij}}{v_{x,ij}} \tag{3.25}$$

$$\alpha_{ij} = \operatorname{atan}\left(\frac{v_{y,slip,ij}}{\left|v_{x,ij}\right|}\right) \tag{3.26}$$

Hence, according to the Pacejka's Magic Formula (MF) adopted for this work, the longitudinal friction coefficient $\mu_{x,ij}$ due to the interaction between ij tyre and the soil is

$$\mu_{x,ij} = D_x \sin\left(C_x \arctan\left(B_x s_{ij}\right)\right) \tag{3.27}$$

and the lateral friction coefficient is

$$\mu_{y,ij} = D_y \sin\left(C_y \arctan\left(B_y s_{ij}\right)\right) \tag{3.28}$$

where the coefficient D_y varies linearly with respect to the vertical load $F_{z,ij}$ according to the equation

$$D_y = d_1 F_{z,ij} + d_2 \tag{3.29}$$

This feature is essential for the purpose of active suspensions control since it allows to catch the nonlinear dependence of the lateral force on the vertical load. The behaviour is depicted in Fig. 3.2 for the full MF tyre model and the fitted reduced one. In addition, s_{ij} is the combined theoretical slip of ij tyre, namely

$$s_{ij} = \sqrt{s_{x,ij}^2 + s_{y,ij}^2} \tag{3.30}$$

in which

$$s_{x,ij} = \frac{\sigma_{ij}}{1+\sigma_{ij}} \tag{3.31}$$

$$s_{y,ij} = -\frac{\tan\left(\alpha_{ij}\right)}{1+\sigma_{ij}} \tag{3.32}$$

Consequently, the longitudinal and lateral tyre forces are, respectively,

$$F_{x,ij} = \frac{s_{x,ij}}{s_{ij}} \mu_{x,ij} F_{z,ij} \tag{3.33}$$

and

$$F_{y,ij} = \frac{s_{y,ij}}{s_{ij}} \mu_{y,ij} F_{z,ij} \tag{3.34}$$

Moreover, by indicating the wheelbase $l = a_f + a_r$, the vertical loads applied to the wheels can be expressed as follows:

$$F_{z,fl} = \frac{1}{2} mg \frac{a_r}{l} - \Delta F_z^x - \Delta F_{z,f}^y \tag{3.35}$$

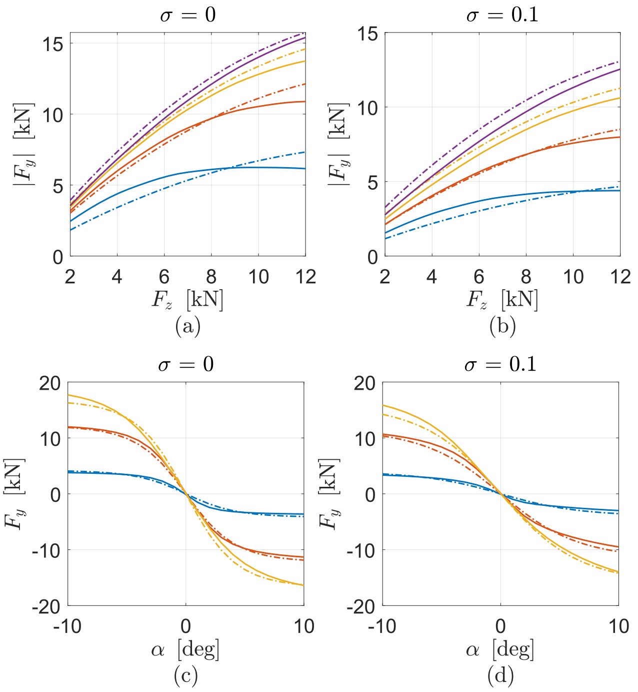

Figure 3.2: Simplified tyre model (dash-dotted lines) and reference full MF model (solid lines). (a) and (b): lateral tyre force as a function of vertical load for two values of longitudinal slip ratio, 0 and 0.1. The four couples of curves correspond to slip angles equal to 2 deg (blue), 4 deg (red), 6 deg (yellow), and 8 deg (purple). (c) and (d): lateral tyre force as a function of slip angle for two values of longitudinal slip ratio, 0 and 0.1, and three vertical loads, 2 kN (blue), 7 kN (red), and 12 kN (yellow).

$$F_{z,fr} = \frac{1}{2}mg\frac{a_r}{l} - \Delta F_z^x + \Delta F_{z,f}^y \tag{3.36}$$

$$F_{z,rl} = \frac{1}{2}mg\frac{a_f}{l} + \Delta F_z^x - \Delta F_{z,r}^y \tag{3.37}$$

$$F_{z,rr} = \frac{1}{2}mg\frac{a_f}{l} + \Delta F_z^x + \Delta F_{z,r}^y \tag{3.38}$$

Further, the longitudinal load shift is:

$$\Delta F_z^x = \frac{1}{2} m a_x \frac{h_{CG}}{l} \tag{3.39}$$

and the transversal load shifts for the two axles are:

$$\Delta F_{z,i}^y = \frac{m a_y \left[l - a_i\right] h_{roll}}{l b_i} + \frac{M_{AR,i}}{b_i} \tag{3.40}$$

For clarity, $M_{AR,i}$ includes both the passive and active contributions.

In the NMPC implementation, (3.1)-(3.40) are re-arranged in the general form

$$\dot{x}(t) = h\left(t, x(t), u(t)\right) \tag{3.41}$$

where x is the state vector, that is to say

$$x = \left[V, \beta, \dot{\psi}, \dot{\varphi}, \varphi, \Omega_{fl}, \Omega_{fr}, \Omega_{rl}, \Omega_{rr}\right] \tag{3.42}$$

t is time; and $u(t)$ is the control input vector, namely

$$u = \left[T_{fl}, T_{fr}, T_{rl}, T_{rr}, f, z_\sigma, z_{\alpha_f}, z_{\alpha_r}, z_T\right] \tag{3.43}$$

where z_σ, z_{α_f}, z_{α_r} and z_T are slack variables, namely, quantities that can be controlled in order to implement constraints with adaptive bounds, which are generally referred to as *soft constraints*.

The presented internal vehicle dynamics model is validated against a high-fidelity vehicle model (the same one adopted for the simulation campaign of Chapter 2), which is implemented by means of AVL VSM simulator. The detailed model was in turn experimentally validated (see also Fig. 2.3). Moreover, the accuracy of the internal model and of the high-fidelity one is assessed on a 40 m radius skidpad manoeuvre (Fig. 3.3) and on a transient steering manoeuvre (Fig. 3.4). The tests give evidence of a good agreement between the experimental data and the simulators both in steady-state and transient conditions.

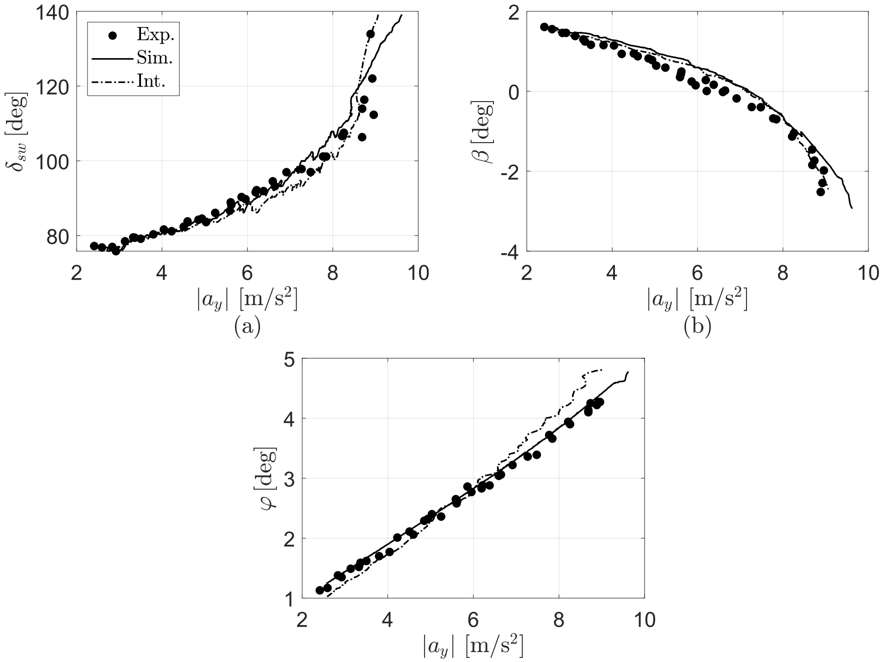

(a)

(b)

(c)

Figure 3.3: Understeer characteristic, sideslip angle and roll angle as functions of lateral acceleration (a_y) during a 40 m radius skidpad manoeuvre. The dots correspond to the experimental results, the solid lines to the high-fidelity simulator, and the dash-dotted lines to the internal model.

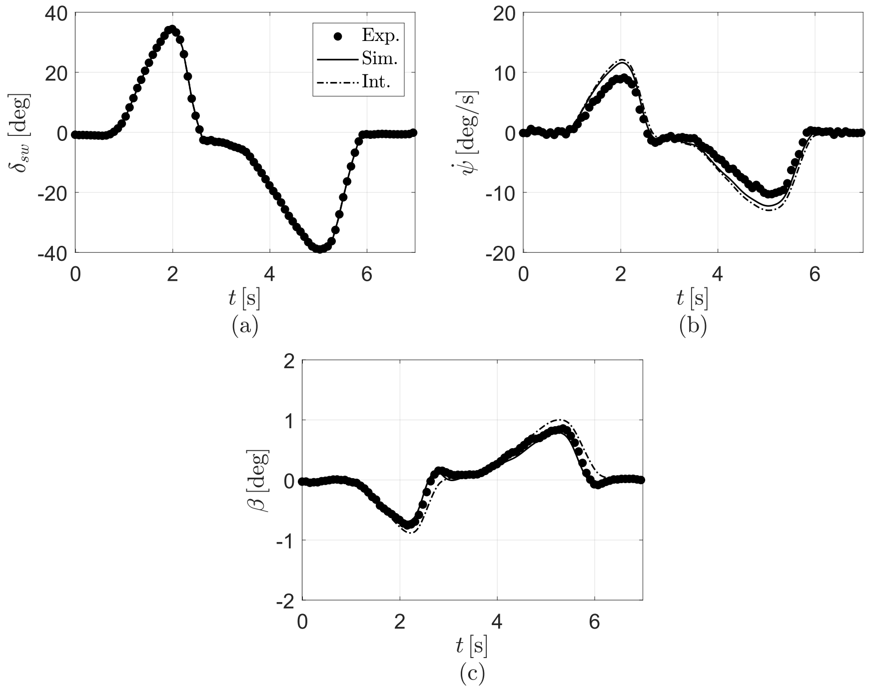

(a) (b)

(c)

Figure 3.4: Time profiles of steering wheel angle, yaw rate and sideslip angle during a transient steering manoeuvre at a vehicle speed of approximately 100 km/h. The dots correspond to the experimental results, the solid lines to the high-fidelity simulator, and the dash-dotted lines to the internal model.

3.3 Optimal control problem formulation

Given the leading role of energy efficiency, a fundamental term of the cost function is the sum of the mechanical and electrical power losses. Specifically, the total losses that the electric vehicle (EV) exhibits at each time instant of the prediction horizon can be indicated by means of the following expression:

$$P_{loss}(t) = P_{loss,\sigma}(t) + P_{loss,\alpha}(t) + P_{loss,el}(t) \tag{3.44}$$

Specifically:

- $P_{loss,\sigma}$ are the power losses due to the longitudinal tyre slips,

$$P_{loss,\sigma}(t) = \sum_{i,j} -v_{x,slip,ij}(t)\, F_{x,ij}(t) \tag{3.45}$$

- $P_{loss,\alpha}$ are the power losses due to the lateral tyre slips,

$$P_{loss,\alpha}(t) = \sum_{i,j} -v_{y,slip,ij}(t)\, F_{y,ij}(t) \tag{3.46}$$

- $P_{loss,el}$ are the power losses of the electric powertrains,

$$P_{loss,el}(t) = \sum_{i,j} \hat{P}_{loss,el,ij}\left(T_{el,ij}(t), \Omega_{ij}(t)\right) \tag{3.47}$$

  where $\hat{P}_{loss,el,ij}(t)$ are the power losses related to the single ij unit, which are expressed through a polynomial of degree 5 on both axes

$$\hat{P}_{loss,el,ij}\left(T_{el,ij}, \Omega_{ij}\right) = \sum_{m=0}^{5} \left(\sum_{n=0}^{5} p_{m,n} T_{el,ij}^{n} \right) \Omega_{ij}^{m} \tag{3.48}$$

  in which $p_{m,n}$ indicates the coefficient of the polynomial. The polynomial fitting that approximates the experimental powertrain power losses, which is displayed in Fig. 3.5, is characterised by R-squared equal to 0.982.

Moreover, the cost function includes a term for tracking the reference yaw rate $\dot{\psi}_{ref}$, that is

$$\Delta\dot{\psi} = \left|\dot{\psi} - \dot{\psi}_{ref}\right| \tag{3.49}$$

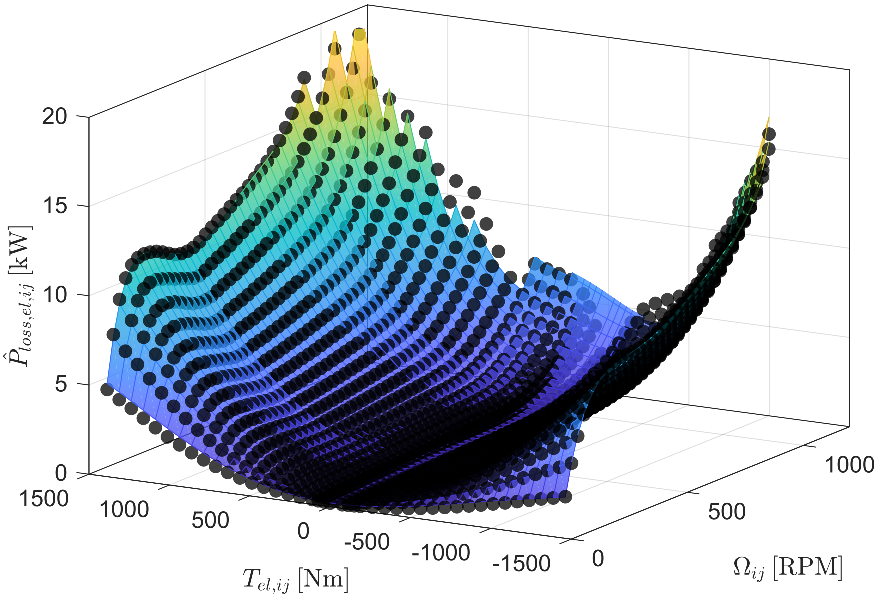

Figure 3.5: Polynomial fitting of the measured powertrain power losses. Dots correspond to experimental data, whereas the mesh is the polynomial fitting

By way of example, in Fig. 3.6 some curves of $\dot{\psi}_{ref}$ are depicted for different vehicle speeds. Additionally, terms for tracking the most efficient front-to-total motor torque distribution for each side of the vehicle are included in the cost function. Specifically, let $f_{T,j}$ be the coefficient for the j side. The terms to be minimised are

$$\Delta f_{T,l} = \left| f_{T,l} - \hat{f}_{T,opt,l} \right| \tag{3.50a}$$

and

$$\Delta f_{T,r} = \left| f_{T,r} - \hat{f}_{T,opt,r} \right| \tag{3.50b}$$

Specifically, $\hat{f}_{T,opt,j}$ is a computationally-efficient approximation of the quantity expressed by (2.12). Indeed, the online application makes use of an approximated solution of $f_{T,opt,j}$ consisting on a set of hyperbolic tangents, as described by [100],

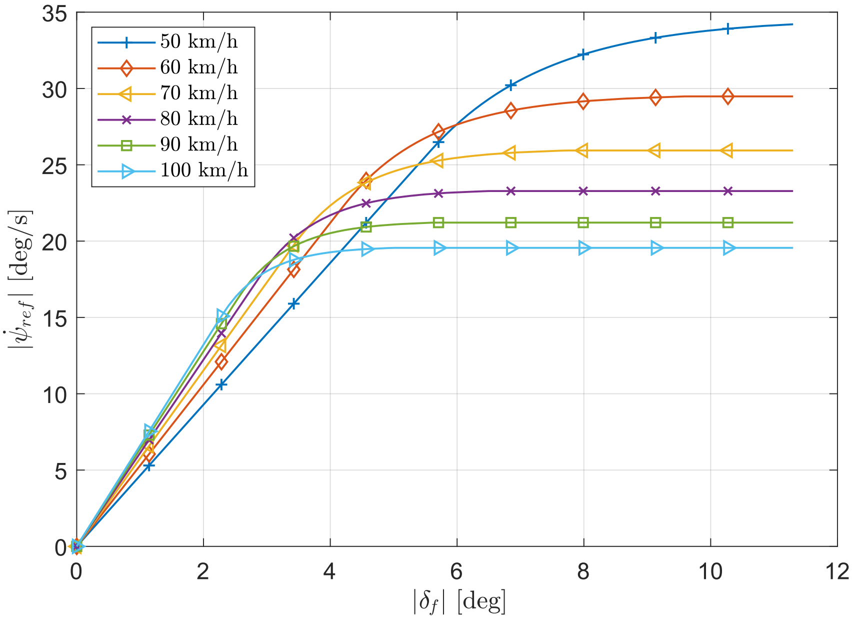

Figure 3.6: Example of reference yaw rate curves as functions of the average front steering angle δ_f for different speed levels, full adherence and zero longitudinal acceleration.

with the form

$$\hat{f}_{T,opt,j} = \zeta_2 + 0.5\,(\zeta_3 - \zeta_2)\tanh\left(\zeta_4\left(T_{el,req,j} - \zeta_1\right)\right) \tag{3.51}$$

where the parameters ζ_1, ζ_2, ζ_3 and ζ_4 depend on the average motor velocity of j side, and $T_{el,req,j}$ is the overall j side motor torque request. An additional term within the objective function is useful to fulfil the overall torque request at the vehicle level, set by a higher level drivability and brake controller. It is defined as follows

$$\Delta T_{req} = \left|\sum_{i,j} T_{ij} - T_{req}\right| \tag{3.52}$$

and T_{req} is the total torque request of the driver, which is a function of the accelerator and brake pedal positions and of the vehicle speed. In order to smooth the control action of f, a further term is in charge to keep the anti-roll moment distribution in the neighbourhood of its base value f_{pass}. Therefore,

$$\Delta f = |f - f_{pass}| \tag{3.53}$$

Moreover, the penalisation of rear axle sideslip angle displacement from the origin is entrusted to the following term, which facilitates vehicle stabilisation during extreme transients:

$$\alpha_r = \left| \frac{1}{2} (\alpha_{rl} + \alpha_{rr}) \right| \tag{3.54}$$

Finally, the four slack variables, z_σ, $z_{\alpha_f}, z_{\alpha_r}$ and z_T, appear also as cost terms because their displacement from the origin needs to be penalised.

Accordingly, the cost function is expressed in the form

$$\begin{aligned} J(x_0, u, p) = \int_0^{T_h} \Big|\Big| \big[& P_{loss}(t), \Delta\dot{\psi}(t), \Delta f_{T,l}(t), \Delta f_{T,r}(t), \Delta T_{req}(t), \Delta f(t), \\ & \alpha_r(t), z_\sigma(t), z_{\alpha_f}(t), z_{\alpha_r}(t), z_T(t) \big] \Big|\Big|_S^2 dt + w_e \Delta\dot{\psi}(T_h) \end{aligned} \tag{3.55}$$

where $x_0 = x(0)$, T_h is the prediction horizon, S is a strictly positive definite scaling matrix for weighting the cost terms and w_e is the weight of the final cost related to the yaw rate error. As can be seen, J depends also on a vector p of parameters that are constant throughout the prediction horizon; precisely,

$$\begin{aligned} p = \big[& \delta_{fl}, \dots, \delta_{rr}, a_x, a_y, \lambda, w, T_{el,min,fl}, \dots, T_{el,min,rr}, \\ & T_{el,max,fl}, \dots, T_{el,max,rr}, M_{AR,Act,max,f}, M_{AR,Act,max,r}, \\ & f_{min}, f_{max}, \sigma_{min}, \sigma_{max}, \alpha_{min,f}, \alpha_{min,r}, \alpha_{max,f}, \alpha_{max,r} \big] \end{aligned} \tag{3.56}$$

in which λ is the front-to-total coefficient for allocating the braking torque according to the low-level electronic brake-force distribution (EBD) signal, and the subscripts '*min*' and '*max*' indicate the minimum and maximum values of the variable. Besides, an important observation concerns the accelerations a_x and a_y. In fact, these quantities are updated over the prediction horizon in (3.1) and (3.2) according to (3.13) and (3.14), whereas they are constant in (3.4), (3.12) and (3.40): this is a simplification dictated by the implicit form of the problem. In practice, the assumption contributes to make the controller more robust at an expense of a negligible loss of accuracy, provided that the prediction horizon is short compared to the vehicle dynamics bandwidth. This sustains the presence of the accelerations in p.

Therefore, the optimal control problem can be formulated in the following form:

$$\min_{u} J(x_0, u, p) \tag{3.57}$$

subject to

$$\begin{aligned}
i.&\quad \dot{x}(t) = h(t, x(t), u(t)), \quad x(0) = x_0 \\
ii.&\quad T_{el,min,ij} + T_{bk,min,ij} \leq T_{ij}(t) \leq T_{el,max,ij} \\
iii.&\quad T_{fl}(t) + T_{fr}(t) \leq \lambda T_{req}(t) \\
iv.&\quad T_{fl}(t)\, T_{rl}(t) + z_T(t) \geq 0 \\
v.&\quad T_{fr}(t)\, T_{rr}(t) + z_T(t) \geq 0 \\
vi.&\quad \left[T_{fl}(t) + T_{fr}(t)\right]\left[T_{rl}(t) + T_{rr}(t)\right] + z_T(t) \geq 0 \\
vii.&\quad f_{min} \leq f(t) \leq f_{max} \\
viii.&\quad \left|M_{AR,Act,i}(t)\right| \leq M_{AR,Act,max,i} \\
ix.&\quad \sigma_{min} - z_\sigma(t) \leq \sigma_{ij}(t) \leq \sigma_{max} + z_\sigma(t) \\
x.&\quad \alpha_{min,i} - z_{\alpha_i}(t) \leq \alpha_{ij}(t) \leq \alpha_{max,i} + z_{\alpha_i}(t) \\
xi.&\quad z_\sigma(t) \geq 0 \\
xii.&\quad z_{\alpha_i}(t) \geq 0 \\
xiii.&\quad z_T(t) \geq 0
\end{aligned}$$

The constraints *ii-vi*) act on the torques: *ii*) sets the upper and lower bounds for each wheel torque, *iii*) imposes the braking torque distribution limits based on λ, which is set to 1 in case of overall motoring to make the constraint ineffective, *iv*) and *v*) help the solver to converge to a solution characterised by concordant torques of the same side, and *vi*), similarly, guides the optimisation so that the overall torques of the two axles have the same sign. The constraint *vii*) limits the range of f, *viii*) defines the maximum absolute values of the active anti-roll moments, *ix*) and *x*) bound, respectively, the

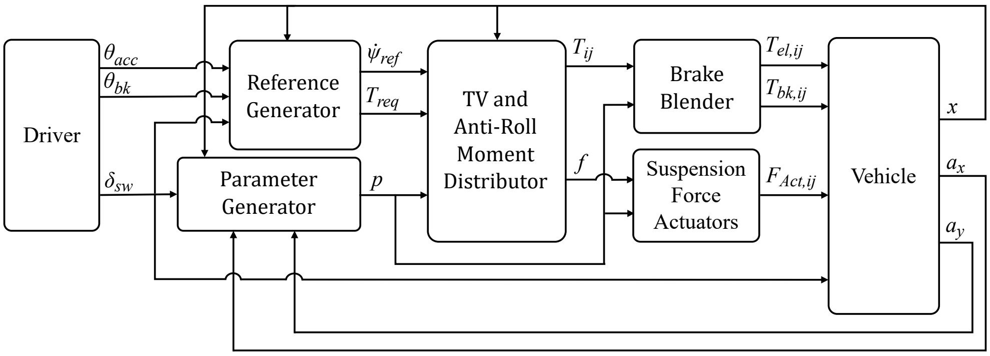

Figure 3.7: Simplified schematic of the simulation environment.

longitudinal slip ratios and the slip angles in a soft fashion. Finally, *xi-xiii*) impose the positivity of the slack variables. It is worth pointing out that the choice to adopt a reduced number of slack variables compared to the number of constraints aims to restrain the number of control variables and thus the computational load.

3.4 Controller implementation and virtual assessment

The optimal control formulation is implemented via ACADO toolkit [134], which offers a powerful interface for NMPC development. The controller so obtained is then connected to AVL VSM vehicle model within a MATLAB/Simulink environment.

The simulation environment, which is depicted in Fig. 3.7, is made of the following components:

- A virtual driver, which is in charge to generate the accelerator and brake pedal inputs (θ_{acc} and θ_{bk}, respectively), as well as the steering wheel angle request δ_{sw}.

- A reference generator, i.e., the block that supplies the the yaw rate reference $\dot{\psi}_{ref}$ and the total torque request T_{ref} based on driver inputs and measured or estimated vehicle states.

- In parallel to the reference generator, a parameter generator computes and collects the fundamental quantities needed by the control allocator and returns the vector of parameters p.

- A TV and anti-roll moment distributor, holding the NMPC-based strategy that provides the optimal wheel torque request T_{ij} and the best front-to-total anti-roll moment distribution demand f.
- A brake blender to split the wheel torque request between the electric motors and the dissipative brakes.
- Suspension force actuators, which are in charge to convert front and rear anti-roll moment requests into active suspension forces $F_{Act,ij}$ for the four corners.
- Finally, the vehicle block receives torque and force inputs as well as the steering wheel angle imposed by the driver and returns the states x and the chassis acceleration components a_x and a_y. For clarity, the vehicle model inside the block is the high-fidelity one, mentioned in Section 3.2 and validated against experimental data as depicted in Fig. 3.3-3.4.

The proposed controller implementation lends itself to a number of different settings. For instance, it is possible to configure the controller to contemplate an arbitrary number of in-wheel motors, and the torque vectoring can be assisted, if necessary, by active anti-roll moment contribution either with fixed or with variable f. Therefore, four distinct vehicle configurations are considered in the following, of which the last two rely on the NMPC controller:

- Active roll angle compensation through active suspension control with fixed front-to-total anti-roll moment distribution ratio $f_{pass} = 0.67$, zero direct yaw moment, i.e. the total wheel torque is the same on the left and right wheels; and front-to-total wheel torque distribution within each vehicle side according to the fixed ratio $f_{T,pass} = 0.5$. The configuration is referred to as $f_{pass} + f_{T,pass}$.
- Active roll angle compensation with fixed $f_{pass} = 0.67$, zero direct yaw moment, and variable front-to-total wheel torque distribution according to a variable

ratio, $f_{T,act}$, defined in the look-up table function obtained through (2.12). This arrangement is designated as $f_{pass} + f_{T,act}$.

- Active roll angle compensation with fixed distribution (f_{pass}) equal to 0.67 and NMPC-based torque vectoring (TV). This set-up is indicated as $f_{pass} + \mathrm{TV}$.
- Active roll angle compensation with NMPC-based active anti-roll moment distribution and torque vectoring, which is referred to as $f_{act} + \mathrm{TV}$.

It is worth stressing that all the four arrangements are equipped with active suspensions for roll moment compensation purposes, but only the fourth layout has the active distribution of the anti-roll moment.

For the sake of comparison fairness, both the aforementioned NMPC-based configurations ($f_{pass} + \mathrm{TV}$ and $f_{act} + \mathrm{TV}$) are characterised by the same weights of the cost function terms. Specifically, all the terms in (3.55) are active in order to allow the vehicle to track the yaw rate and the total torque request while trying to limit the slips and the overall losses. Table 3.1 summarises the fundamental settings of the controller: these, as well as the weights of the cost terms were chosen based on author's experience. In particular, the sampling time Δt_c, equal to 20 ms, and the number of optimisation steps across the prediction horizon, equal to 15, turned out after extensive simulations to be a good compromise between control performance and computational effort. Also, it is worth mentioning that a maximum number of 10 solver iterations N_{iter} is allocated in all cases to ensure the local minimum is achieved, though it was verified that even a single iteration secures systematically the convergence to a result that is very close to the local optimum. Moreover, a relatively short integration time step Δt_{int} is useful to ensure the numerical stability of the internal model without conditioning appreciably the computational time. Finally, the adopted quadratic programming solver is qpOASES3 [135]. Further settings concerning the selected algorithms are listed in Table 3.2.

Accordingly, two significant manoeuvres are performed to assess the dynamic as well as energy-saving qualities of the proposed strategy. The simulation results are presented in the following.

Table 3.1: Fundamental settings of the controller.

Symbol	Value	Description
Δt_c	20ms	Controller sampling time
Δt_{int}	0.5ms	Integration time step
N	15	Number of optimisation steps
N_{iter}	10	Maximum number of solver iterations

Table 3.2: Selected algorithms.

Description	Algorithm
Hessian approximation	Gauss-Newton
Discretization type	Multiple shooting
Integrator type	Implicit Runge-Kutta of order 4

3.4.1 Ramp steer manoeuvre

The steady-state manoeuvre consists in a steering wheel angle ramp at a rate of 5 deg/s. The speed is essentially constant and equal to ~100 km/h. A selection of plots relative to the present test is reported in Fig. 3.8 - 3.10.

First of all, it is worth pointing out that the cornering response of $f_{pass} + f_{T,pass}$ and $f_{pass} + f_{T,act}$, owing to the lack of yaw moment actuation, is the result of the vehicle hardware set-up, namely, suspensions, mass distribution and tyres.

Fig. 3.8a demonstrates that the two configurations that rely on TV are tracking the same understeer characteristic, which is rather different from that of the other two vehicle configurations: the reference yaw rate tracked by the NMPC-based set-ups is such that it extends the linear region and makes the vehicle understeer less, which is essentially a sport-oriented feature. The control actions of $f_{pass} + \text{TV}$ and $f_{act} + \text{TV}$ (Fig. 3.8d and Fig. 3.9a-d) reveal two distinct ways to interpret the same manoeuvre, despite the substantial overlap of cornering responses of the two configurations. Indeed, simulation results show that, in the presence of f_{act} and for a wide range

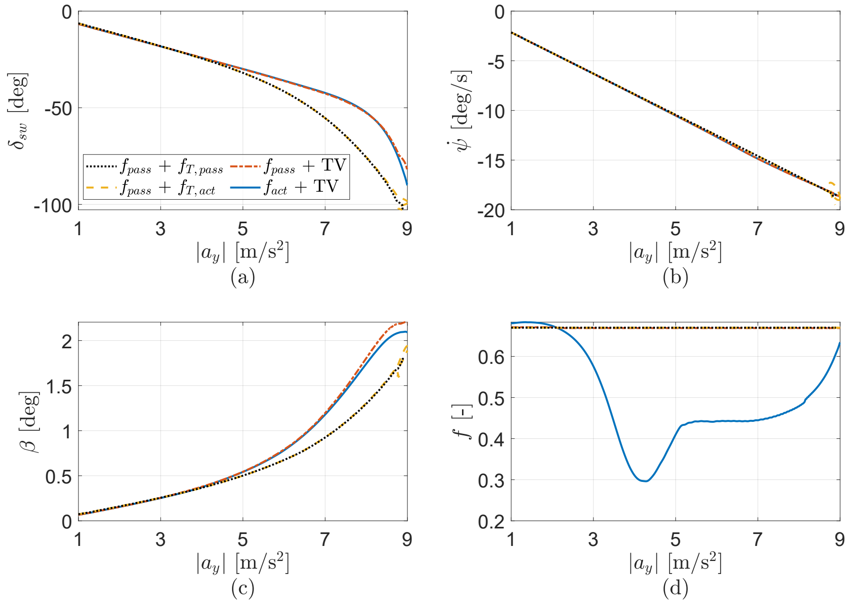

Figure 3.8: Ramp step steer manoeuvre: (a) steering-wheel angle, (b) yaw rate, (c) sideslip angle, (d) front-to-total anti-roll moment distribution coefficient.

of lateral accelerations, it is more profitable to make the vehicle understeer less by reducing the front anti-roll moment distribution (Fig. 3.8d). This action allows to mitigate the magnitude of the electric torques and alleviate their overall yaw moment contribution (Fig. 3.9a-d). As a result, the four electric motors are always in traction when combined with f_{act}, whereas, if the lateral acceleration exceeds ~5 m/s^2, the fixed anti-roll moment distribution of $f_{pass}+\text{TV}$ has the consequence of compelling the inner motors to operate in regeneration. A very interesting consequence is that, at high lateral acceleration, the selected sport-oriented reference yaw rate, despite the desired cornering response, yields a significant P_{loss} increase with respect to $f_{pass}+\text{TV}$, which is the highest among all the configuration. After all, it is well-known from the literature ([21, 26, 25]) and from the extensive analysis presented in Chapter 2 that the introduction of a direct yaw moment through wheel torque allocation has typically the

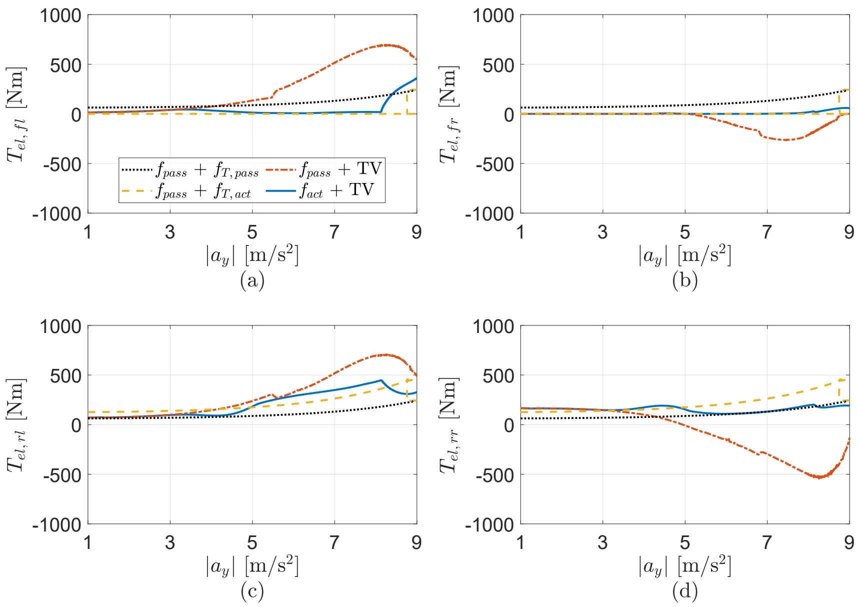

Figure 3.9: Ramp step steer manoeuvre: electric motor torque of the (a) front-left corner, (b) front-right corner, (c) rear-left corner, (d) rear-right corner.

consequence of moving the powertrains away from the optimal operating region, so TV is a favourable solution in terms of energy-efficiency as long as the tyre slip power losses reduction, yield by TV, is greater than the additional power consumption due to TV itself. On the contrary, the active anti-roll moment distribution also has significant advantages in terms of energy-efficiency while describing the same sporty understeer characteristic because it allows to shape the cornering response while restraining the torque vectoring contribution. The behaviour finds a sound evidence in Fig. 2.8e, which displays the presence of a whole region suitable for reducing the battery power usage and hence the power losses relative to the baseline set-up.

The battery power usage P_{batt} (Fig. 3.10a) mirrors, on the one hand, the more composed and milder utilisation of the powertrain resulting from the variable f and, on the other hand, testifies a more severe actuation of the motors if f is fixed. Eventually,

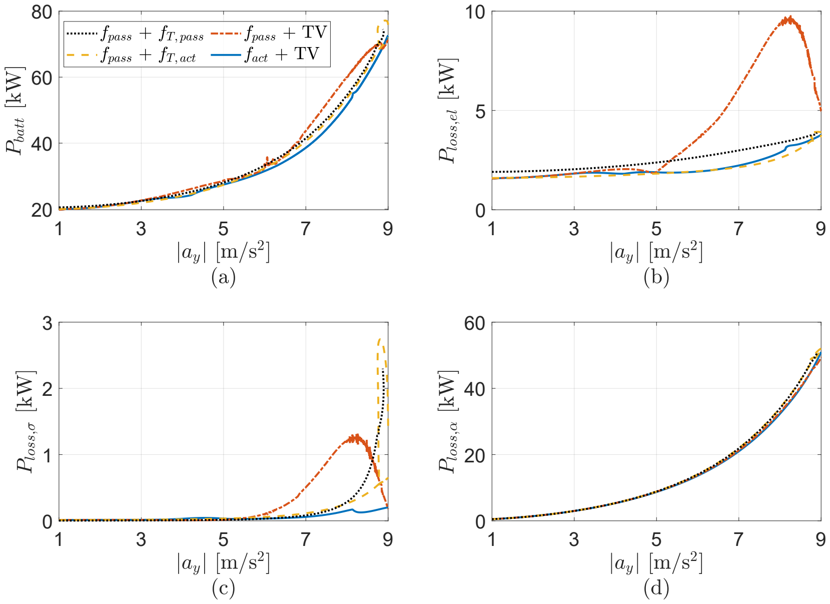

Figure 3.10: Ramp step steer manoeuvre: (a) battery power, (b) electric motor power losses, (c) longitudinal tyre slip power losses, (d) lateral tyre slip power losses.

at about 4 m/s^2, that is, where the lateral load transfer starts becoming notable, the active anti-roll moment distribution begins offering remarkable benefits in terms of consumption reduction. This also translates into significantly lower powertrain power losses (Fig. 3.10b) and mitigated longitudinal tyre slip power losses (Fig. 3.10c) with respect to the configuration $f_{act}+\text{TV}$ above 5 m/s^2. For the sake of completeness, the lateral tyre slip power losses are reported in Fig. 3.10d: as the lateral acceleration grows, $P_{loss,\alpha}$ reduction provided by the NMPC strategy becomes higher.

In summary, above the medium lateral accelerations, the active anti-roll moment allotment can support effectively torque vectoring for the sake of active yaw moment generation, thus contributing to energy saving and to vehicle stabilisation.

Table 3.3 encloses some performance indices that help to confirm the main findings or to deepen the analysis. Before proceeding, the definitions of the relevant indices are

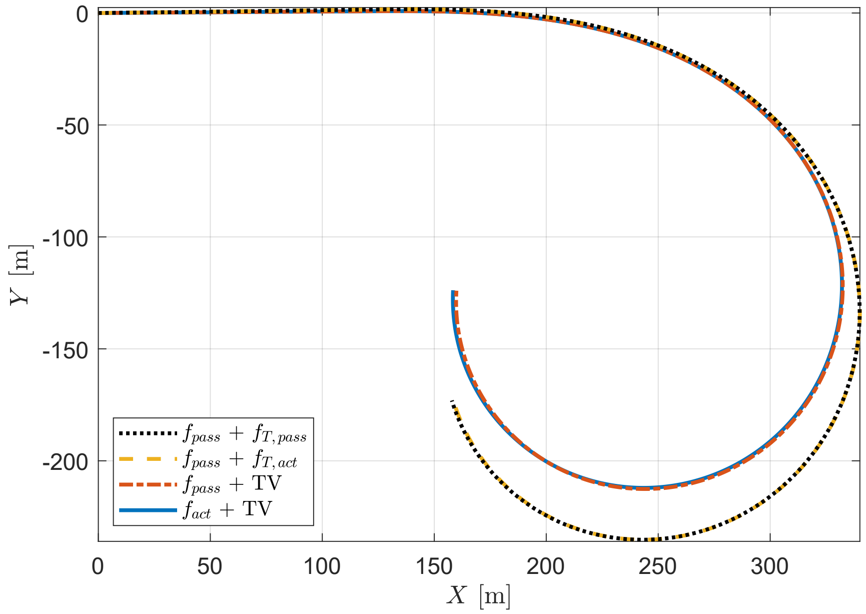

Figure 3.11: Ramp step steer manoeuvre: trajectories.

given below.

- $\overline{D}_{M_z}$ is the average value of $|T_{fr} + T_{rr} - T_{fl} - T_{rl}|$ for the points in the range 1-8 m/s^2 of lateral accelerations; this is an indication of the magnitude of the direct yaw moment contribution produced by the wheel torque allocation.
- $\overline{D}_f$ is the mean of $|f - f_{pass}|$ over the range 1-8 m/s^2 of lateral accelerations, which gives a measure of the average deviation from base value of the front-to-total anti-roll moment distribution.
- $\overline{P}_{loss}$ is the average total loss, which is computed for three distinct bands of lateral acceleration, namely 1-3 m/s^2, 3-6 m/s^2 and 3-8 m/s^2.

In order to highlight the effects on total power losses connected to the adopted reference understeer characteristic, the same indicators are depicted for the two NMPC-based set-ups also in case a reference understeer characteristic very similar to

Table 3.3: Performance indicators for the four vehicle configurations during the ramp steer manoeuvre.

	$\overline{D}_{M_z}$ [Nm]	$\overline{D}_f$ [-]		$\overline{P}_{loss}$ [kW]	
a_y [m/s^2]	1-8	1-8	1-3	3-6	6-8
$f_{pass} + f_{T,pass}$	0	0.00	3.49	10.37	26.97
$f_{pass} + f_{T,act}$	0	0.00	3.17	9.88	26.22
$f_{pass} + \mathrm{TV}$	719	0.00	3.21	9.70	30.76
$f_{act} + \mathrm{TV}$	122	0.19	3.21	9.27	25.64
$f_{pass} + \mathrm{TV}^\dagger$	131	0.00	3.07	10.08	25.87
$f_{act} + \mathrm{TV}^\dagger$	180	0.09	3.07	9.80	25.62

†Using a reference yaw rate close to the one of the vehicle configurations without TV

the baseline is selected. The two relevant cases are referred to as $f_{pass} + \mathrm{TV}^\dagger$ and $f_{act} + \mathrm{TV}^\dagger$. This reveals that also the configuration relying on TV with fixed anti-roll distribution brings a significant reduction of power losses at high lateral accelerations while adopting a yaw rate reference that produces a cornering response similar to those of $f_{pass} + f_{T,pass}$ and $f_{pass} + f_{T,act}$.

The average power losses confirm that at high lateral accelerations the sport-oriented reference understeer characteristic is appreciably detrimental from an energy-saving viewpoint with respect to $f_{pass} + \mathrm{TV}$. Indeed, the intense TV control action applied by this set-up to follow the reference yaw rate impacts conspicuously on the powertrain power losses. As a result, at high a_y, the average power usage and power losses are higher than those exhibited by the two configurations without TV. Conversely, the effectiveness and versatility of the active anti-roll moment allocation in combination with torque vectoring are once again remarked. This double actuation not only permits at will shaping of the vehicle cornering response, but also, starting from mid lateral accelerations, allows to reduce appreciably the average power losses relative to those of all the other vehicle set-ups.

A further observation concerns the average power losses at low lateral accelerations. In this region, where the tyre slip power losses are negligible, there exists a substantial similarity between the configurations $f_{pass}+f_{T,act}$, $f_{pass}+\mathrm{TV}$ and $f_{act}+\mathrm{TV}$: this aspect testifies the action of the NMPC controller aimed to establish the optimal front-to-total torque distribution within each side as realised by $f_{pass}+f_{T,act}$.

By focusing on $\overline{D}_{M_z}$, the index confirms the severe direct yaw moment injection with respect to $f_{pass}+\mathrm{TV}$ while describing the sporty understeer characteristic, whilst $f_{act}+\mathrm{TV}$ exhibits a milder $\overline{D}_{M_z}$ regardless the chosen reference curve.

Finally, Fig. 3.11 depicts the trajectories described by the four vehicles while performing the ramp steer manoeuvre. The sport-oriented understeer characteristic provides higher $\dot{\psi}$ for a given δ_{sw} compared to the baseline. As a result, the trajectories produced by the two set-ups with TV have smaller curvature radii compared to those of the other two configurations.

3.4.2 Double step steer manoeuvre

The transient manoeuvre consists in a rapid sequence of steering wheel strokes while maintaining a constant accelerator pedal position equal to 20% of its maximum travel. The starting speed is ~105 km/h. Evidently, this is an extreme scenario that aims to prove the control performance in terms of vehicle dynamic response as well as the numerical robustness of the controller itself. It is worth observing that, despite the fixed pedal request, based on the adopted weighing matrix S (the same as the one utilised for the ramp steer manoeuvre), the controller is free to cut the torque request in favour of reference yaw rate tracking and power losses minimisation.

Fig. 3.12 - 3.15 gather the most significant plots resulting from the manoeuvre, and the most relevant performance metrics are collected in Table 3.4. In addition to the indicators adopted for the ramp steer test, the following indices are provided:

- $\Delta\dot{\psi}_{RMS}$ is the root mean square (RMS) of the yaw rate error, that is, a measure of the tracking capability of the controller. The metric is given also for $f_{pass}+f_{T,pass}$ and $f_{pass}+f_{T,act}$, regardless the lack of a yaw rate tracking control action, by considering the same reference as the one of the two set-ups with TV.
- $|\beta_{max}|$, i.e. the peak absolute value of the vehicle body sideslip angle, providing

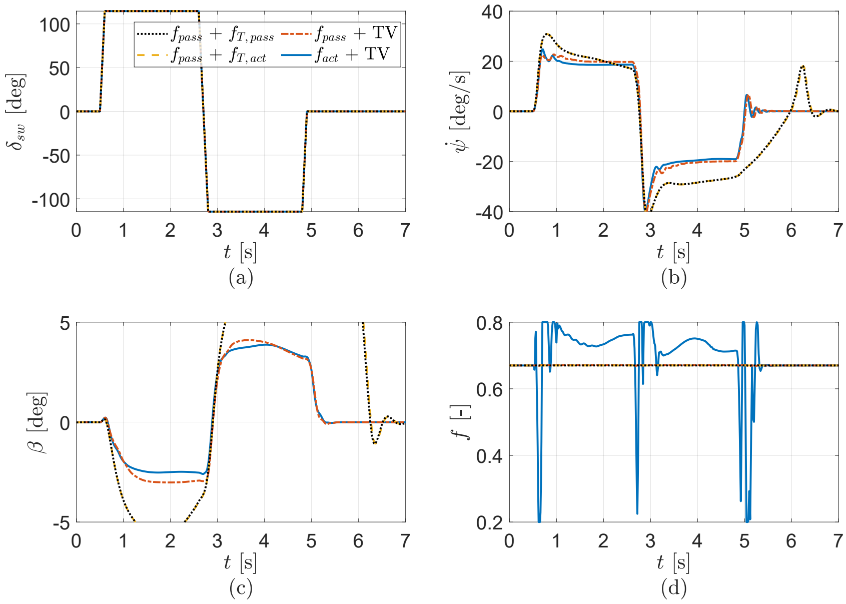

(a) (b)

(c) (d)

Figure 3.12: Double step steer steer manoeuvre: (a) steering-wheel angle, (b) yaw rate, (c) sideslip angle, (d) front-to-total anti-roll moment distribution coefficient.

a measure of vehicle stability.

- $\Delta F^{y}_{z,RMS}$, defined as the RMS of $F_{z,fl} + F_{z,rl} - F_{z,fr} - F_{z,rr}$, indicates the intensity of the lateral load transfer and supplies a measure of vehicle rollover tendency.
- $\overline{D}_{cut}$, namely, $T_{req} - (T_{fl} + T_{fr} + T_{rl} + T_{rr})$, which measures the intensity of total wheel torque reduction, compared to the overall torque request, to foster yaw rate tracking and power losses minimisation.
- V_{fin}, that is, the final vehicle speed, which represents a measure of the kinetic energy variation.

Note that for the multiple step steer manoeuvre, all the metrics are computed across the whole later acceleration range.

Table 3.4: Performance indicators for the four vehicle configurations during the multiple step steer manoeuvre.

	$\Delta\dot{\psi}_{RMS}$ [deg/s]	$\lvert\beta_{max}\rvert$ [deg]	$\Delta F^{y}_{z,RMS}$ [kN]	$\overline{D}_{M_z}$ [Nm]	$\overline{D}_{cut}$ [Nm]	$\overline{D}_{f}$ [-]	V_{fin} [km/h]	$\overline{P}_{loss}$ [kW]
$f_{pass}+f_{T,pass}$	10.46	18.37	24.95	307	433	0.00	83.3	133,84
$f_{pass}+f_{T,act}$	10.51	18.50	24.96	308	432	0.00	83.0	134,43
$f_{pass}+\text{TV}$	5.14	4.11	22.18	1333	731	0.00	101.6	78,99
$f_{act}+\text{TV}$	4.71	3.87	21.81	1231	491	0.09	106.4	75,78

Fig. 3.12a illustrates the aggressive steering wheel angle profile imposed by the driver: each stroke has a rate greater than 500 deg/s.

The yaw rate curves are depicted in Fig. 3.12b. Both the NMPC-based configurations ensure stable yaw rate tracking with limited overshoot after the steering angle transients, which also translates into significantly restrained sideslip angles (Fig. 3.12c). Conversely, $f_{pass}+f_{T,pass}$ and $f_{pass}+f_{T,act}$ exhibit much more erratic yaw rate profiles and delays relative to the steering angle in recovering the condition of zero yaw rate and zero sideslip angle, especially after the second steering stroke. In fact, the peak absolute value of sideslip angle is ~4 deg for the TV-based configurations, whereas it reaches ~18 deg in the absence of the control action.

The front-to-total anti-roll moment distribution (Fig. 3.12d) related to $f_{act}+\text{TV}$ manifests pronounced peaks after the steering angle transients for mitigating the yaw rate oscillations. Elsewhere, f is generally biased towards the front axle to enhance understeer attitude and so vehicle stability.

Further remarks concern the lateral load transfer. Indeed, $\Delta F^{y}_{z,RMS}$ testifies a severe side load shift imposed by the manoeuvre. However, only the active control intervention allows to avert both inner wheels from lifting following the second steering angle transient, thus reducing rollover risk. In fact, with respect to $f_{pass}+\text{TV}$ and $f_{act}+\text{TV}$, only the front inner wheel detaches from ground, whilst both $f_{pass}+f_{T,pass}$ and $f_{pass}+f_{T,act}$ exhibit a dangerous lift of both inner wheels, as demonstrated by Fig. 3.13. In addition, vain spin of inner wheels of $f_{pass}+f_{T,pass}$ and $f_{pass}+f_{T,act}$

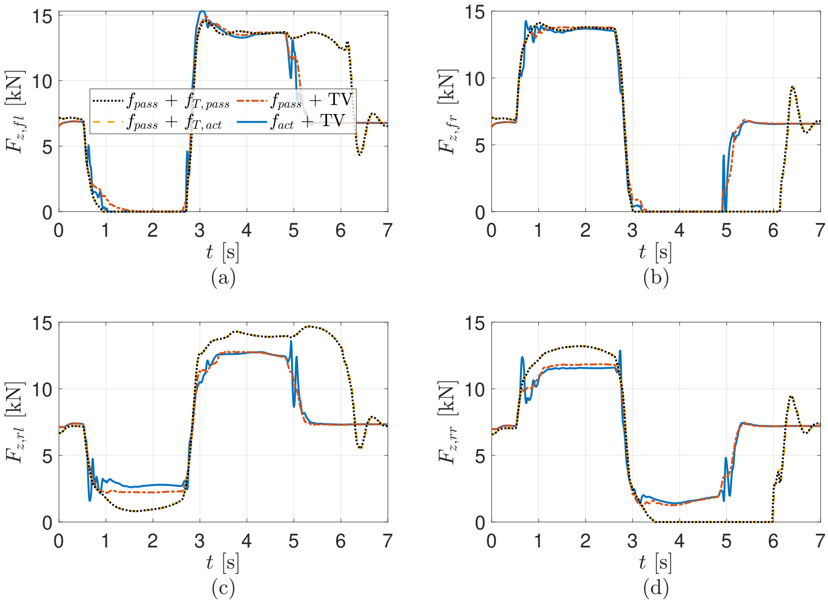

(a) (b) (c) (d)

Figure 3.13: Double step steer steer manoeuvre: vertical loads of the (a) front-left corner, (b) front-right corner, (c) rear-left corner, (d) rear-right corner.

determines the corresponding motor torque saturation, which explains the non-zero values of $\overline{D}_{M_z}$ and $\overline{D}_{cut}$ also in the absence of TV. In other words, the yaw moment related to $f_{pass} + f_{T,pass}$ and $f_{pass} + f_{T,act}$ as well as the total torque reduction can be regarded as an uncontrolled side effect produced by the extreme operating condition of the inner motors. As a confirmation of what stated, the electric motor torques are displayed in Fig. 3.14a-d. Evidently, the NMPC-based configurations exhibit similar trends of the electric motor torques; moreover, the disappearance of $T_{el,fr}$ and $T_{el,rr}$ following the second steering wheel stroke can be observed clearly for $f_{pass} + f_{T,pass}$ and $f_{pass} + f_{T,act}$.

Furthermore, for the sake of completeness, also the battery power usage (Fig. 3.15a) and the power losses (Fig. 3.15b-d) are presented. In this manoeuvre the NMPC provide remarkable power loss reduction. In fact, the average power losses with respect

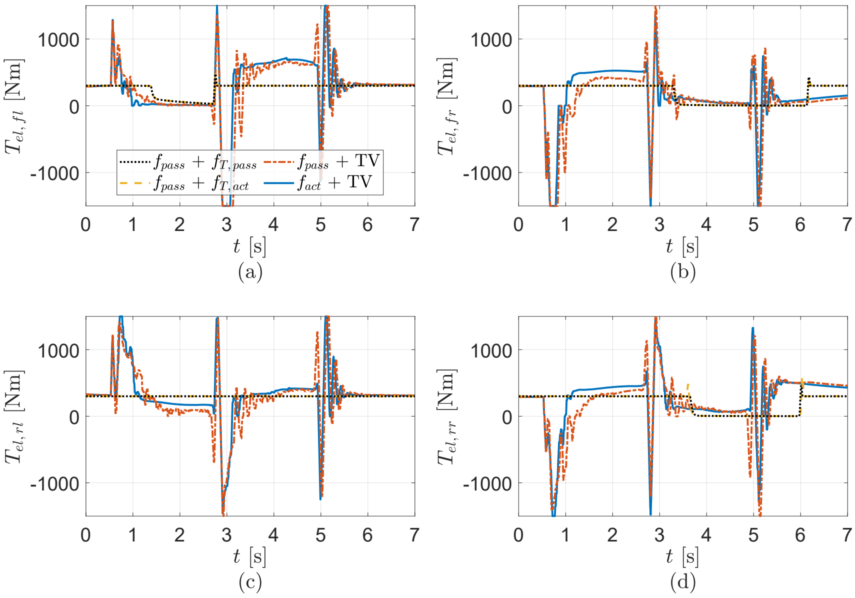

Figure 3.14: Double step steer steer manoeuvre: electric motor torque of the (a) front-left corner, (b) front-right corner, (c) rear-left corner, (d) rear-right corner.

to $f_{pass} + \mathrm{TV}$ and $f_{act} + \mathrm{TV}$ are ~50 kW lower than those characterising $f_{pass} + f_{T,pass}$ and $f_{pass} + f_{T,act}$. Moreover, the benefits provided by the front-to-total anti-roll moment distribution translate also into ~4% of average total power loss decrease relative to $\overline{P}_{loss}$ of $f_{pass} + \mathrm{TV}$, notwithstanding an efficient energy management is not the main concern while performing such an emergency manoeuvre.

The final speed V_{fin} highlights a substantial velocity drop affecting $f_{pass} + f_{T,pass}$ and $f_{pass} + f_{T,act}$, result of the considerable tyre slips. It is interesting to observe that, despite the average torque reduction ($\overline{D}_{cut}$) imposed by the controller, $f_{act} + \mathrm{TV}$ is even able to achieve a final speed (106 km/h) that exceeds the initial one (105 km/h), which corresponds to ~5% final speed increase relative to that of the set-up based on TV only.

Briefly, also in this extreme scenario, the NMPC solution endowed with front-to-

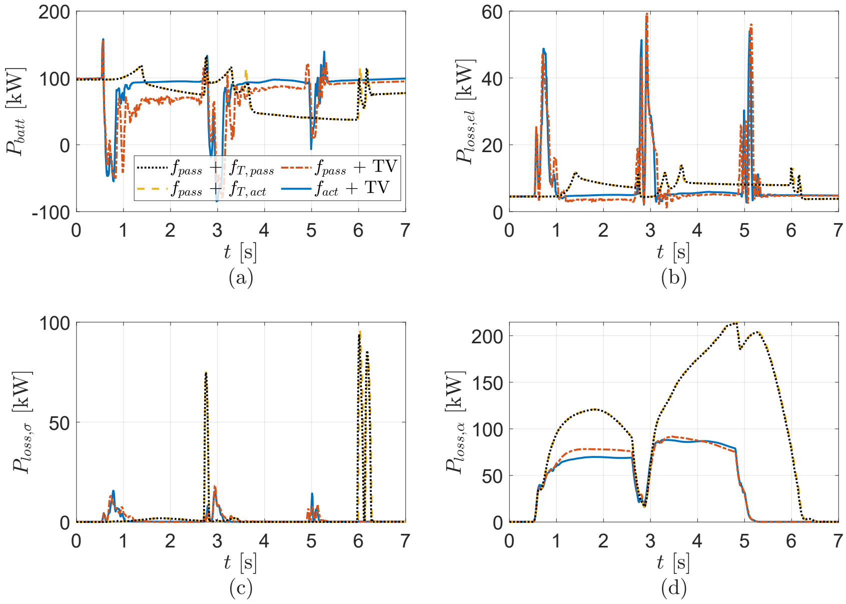

(a) (b)

(c) (d)

Figure 3.15: Double step steer steer manoeuvre: (a) battery power, (b) electric motor power losses, (c) longitudinal tyre slip power losses, (d) lateral tyre slip power losses.

total anti-roll moment distribution in conjunction with torque vectoring outperforms the one relying on TV only, both in terms of stability and power loss reduction.

Finally, the trajectories described by the four vehicles while performing the double step steer manoeuvre are represented in Fig. 3.16.

3.5 Conclusion

The present study demonstrates that it is possible to take advantage from a nonlinear model predictive control to allocate effectively both the torques and the anti-roll moment. The proposed integrated controller is suitable to exploit the fundamental assets offered by the active roll stiffness allotment at medium-to-high lateral accelerations while retaining the unquestionable benefits of torque vectoring. As demonstrated

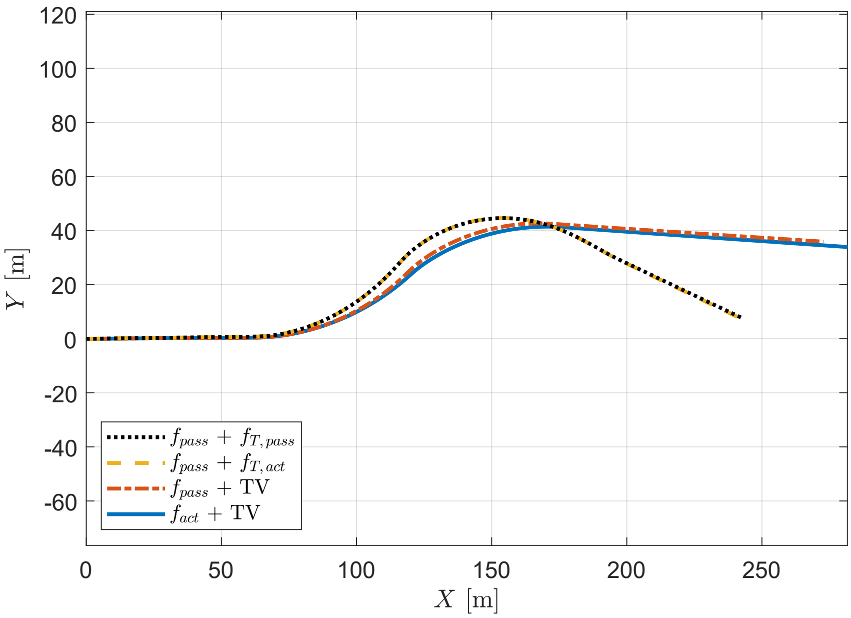

Figure 3.16: Double step steer steer manoeuvre: trajectories.

above, the versatility and robustness of the implementation is such that even a standard controller tuning ensures noticeable performance in a wide span of operating conditions ranging from the steady-state to the most demanding transient manoeuvres.

The fundamental findings of the present study can be summarised as follows:

- In quasi-steady-state conditions, simultaneous and integrated control of direct yaw moment via torque vectoring and anti-roll moment distribution yields remarkable powertrain and tyre slip power losses reduction while ensuring great freedom in terms of cornering response shaping. In fact, in accordance with the discoveries exposed in Chapter 2, generally, the choice of a whatever reference yaw rate providing a lower level of understeer than the baseline is in favour of energy efficiency. This trend is confirmed by the simulations in Section 3.4, which show that substantial energy-saving capabilities supplied by the anti-roll moment distribution in conjunction with TV exist in case of sport-oriented reference yaw rate.

- Torque vectoring as a single actuation offers unquestionable cornering response shaping capabilities; however, its energy-efficiency authority strongly depends on the selected understeer characteristic, which factually poses a compromise between power-saving and cornering behaviour. This statement is confirmed by the results presented in in Chapter 2: specifically, Fig. 2.8a displays that, generally, the energy-efficient understeer characteristic shows a marginally lower level of understeer than the baseline. This trends mirrors the fact that the introduction of a direct yaw moment can promote tyre slip power losses limitation but it is an energy-consuming task from the powertrain viewpoint. Therefore, the torque vectoring strategy on its own for the sake of energy saving finds justification to the extent that the additional power usage imposed by the powertrains is lower than the tyre slip power loss reduction.

- A rule-based strategy for energy-efficient front-to-total motor torque distribution as the one exploited by $f_{pass} + f_{T,act}$ can effectively contribute to limit the powertrain power losses at low-to-medium lateral accelerations, i.e. where longitudinal and lateral tyre slips are negligible.

- In extreme transient conditions, the integrated control strategy based on a nonlinear model predictive control supplies factual benefits in terms of yaw rate tracking, sideslip angle restriction, rollover risk minimisation, overall power loss reduction and travelling speed increase. And the simultaneous control of torque vectoring and front-to-total anti-roll moment distribution brings a systematic benefit in all the aforementioned aspects.

In conclusion, the study has revealed some promising trends concerning the integrated control of torque vectoring and anti-roll moment distribution in favour of vehicle dynamics and energy efficiency. Experimental evaluation of the strategy on an electric vehicle demonstrator will be carried out in the future.

Conclusion

The present study started with a presentation of the mobility electrification scene. Technical advances together with national governments incentives have turned out in a growing number of hybrid an electric vehicles travelling on public roads. After all, such vehicles are not only preferable for reducing the pollutant emissions and noise: they are more and more desirable for their tempting ownership costs compared to traditional solutions. Interestingly, electrification is not limited to passenger cars but also addresses off-road and heavy-duty vehicles such as agricultural tractors. As a proof of that, an emblematic case study was described in detail, outlining the plenty of benefits deriving from an electrified powertrain, which are arguably even more than those offered to passenger cars. Special attention was paid also to the empirical and rule-based strategies that definitely make possible substantial energy saving. Then it was pointed out that electrification convenience can also be found in connection with vehicle dynamics. Indeed, the high bandwidth of electric motors and independent-drive architecture are the ingredients to bring vehicle handling, stability, safety and energy-efficiency to a higher level.

Then, the analysis went through the equations that rule dynamics because they represent the perfect tool to predict the behaviour of a vehicle for the sake of control development. Beside the classical formulations such as multibody, a quite recent approach for vehicle dynamics simulation, i.e. mass-spring soft-body model (MSM), was outlined and compared against the former approaches in three meaningful manoeuvres. Certainly, numerical efficiency and scalability make MSM a potentially viable technique also for model-based controls. Because the approach is very suitable to describe flexible components, MSM may be exploited within model-predictive controls to simulate deformable tyres over rough terrains. This may be very advantageous in the context of off-road vehicle electrification.

Subsequently, an extensive analysis was performed to highlight the energy-efficiency that single and multiple actuations are capable of in quasi-steady-state cornering conditions. The thorough simulation campaign confirmed satisfactory energy-saving capabilities with respect to torque vectoring and rear-wheel steering at low-to-medium lateral accelerations, and revealed substantial authority of anti-roll moment distribution at medium-to-high lateral accelerations. Also, the tests uncovered satisfactory power-saving potentialities as a result of an adequate torque allocation between the motors of the same side. Naturally, combined actuations allow reducing further the overall power consumption throughout the lateral acceleration domain.

Therefore, based on the aforementioned findings concerning individual and multiple actuations, an energy-aware integrated optimal control was developed to exploit the assets of torque vectoring and anti-roll moment distribution. The proposed model-predictive control is effective in quasi-steady-state cornering conditions as well as in extreme safety-critical transient scenarios. In fact, simulations showed that torque vectoring synergistically with anti-roll moment distribution has substantial desirable implications in terms of power-saving, handling, stability and safety. Features that TV on its own cannot catch effectively at the same time.

The research is promising. However there are still some open points that need to be addressed. Firstly, energy-saving capabilities related to the different actuations should be assessed also along full diving cycles. Indeed, a ramp steer manoeuvre has the unique feature of allowing the uniform exploration of the whole spectrum of lateral accelerations, but is not fully representative of some typical driving scenarios. Secondly, throughout this study, the power used by active suspensions has been neglected because the focus was on how the system, which is already available on board for ride comfort purposes, can be further exploited to enhance vehicle safety and range autonomy. Nonetheless, future studies will include the energy-based modelling of suspension actuators to determine their impact on the overall energy efficiency. To this end, a more detailed suspensions model will be developed.

Future work will encompass the assessment of the integrated controller in a wider range of conditions, and its experimental evaluation on an actual electric vehicle demonstrator. Moreover, given the energy-efficiency capabilities of rear-wheel steering, this will be included in the future developments of the control.

Appendix A

Code for extracting the subset for minimum power envelope

Below, the MATLAB code that performs the extraction of the subset of points that are used to compute the minimum power envelope.

```matlab
function [bin, xmin, ymin, zmin, xmax, ymax, zmax] = ...
    cloudslicer(x, y, z, xgrid, ygrid, nworkers)
% CLOUDSLICER groups points (x, y, z) into the bins of the grid
% (xgrid, ygrid) and returns min and max for each bin, in addition to the
% full bins.
%
% Example:
%
% delete(gcp('nocreate'))
%
% x = 2*rand(1e5,1) - 1;
% y = 2*rand(1e5,1) - 1;
% z = 2*rand(1e5,1) - 1;
%
% [xgrid, ygrid] = ...
%     ndgrid(linspace(min(x), max(x), 50), linspace(min(y), 0, 20));
%
```

```
% nworkers = 1;
%
% [bin, xmin, ymin, zmin, xmax, ymax, zmax] = ...
%     cloudslicer(x, y, z, xgrid, ygrid, nworkers);
%
% figure
% scatter3(x, y, z, 50)
% hold on; axis equal;
% scatter3(xmin, ymin, zmin, 40, '*r')
% scatter3(xmax, ymax, zmax, 40, '*r')

%% Skip parfor if there is only one worker
if nworkers == 1
    [bin, xmin, ymin, zmin, xmax, ymax, zmax] = ...
        subcloudslicer(x, y, z, xgrid, ygrid);
    return
end

%% Possibly, flip to slice along the longest dimension
if size(xgrid, 2) < size(xgrid, 1)
    xgrid = xgrid';
    ygrid = ygrid';
end

%% Domain slicing
dlims = round(linspace(1, size(xgrid, 2), nworkers + 1));
subxgrid = cell(nworkers, 1);
subygrid = cell(nworkers, 1);
for ii = 1:nworkers
    col = dlims(ii):dlims(ii + 1);
    subxgrid{ii} = xgrid(:, col);
    subygrid{ii} = ygrid(:, col);
end

%% Parfor
```

```
parpool('local', nworkers)
parfor ii = 1:nworkers
    [subbin{ii}, subxmin{ii}, subymin{ii}, subzmin{ii}, ...
        subxmax{ii}, subymax{ii}, subzmax{ii}] = ...
        subcloudslicer(x, y, z, subxgrid{ii}, subygrid{ii});
end

%% Reassemble the outputs
bin = cell(size(xgrid, 1) - 1, size(ygrid, 2) - 1);
offset = 0;
for ii = 1:nworkers
    len = length(dlims(ii):dlims(ii + 1) - 1);
    bin(:, (1:len) + offset) = subbin{ii};
    offset = len + offset;
end

xmin = cell2mat(subxmin(:));
ymin = cell2mat(subymin(:));
zmin = cell2mat(subzmin(:));

xmax = cell2mat(subxmax(:));
ymax = cell2mat(subymax(:));
zmax = cell2mat(subzmax(:));

end

function [bin, xmin, ymin, zmin, xmax, ymax, zmax] = ...
    subcloudslicer(x, y, z, xgrid, ygrid)
% SUBCLOUDSLICER groups points (x, y, z) into the sub-bins of the grid
% (xgrid, ygrid) and returns min and max for each sub-bin, in addition to
% the full sub-bins.

%% Discard the points that are out of the grid
t1 = [
    xgrid(1,     1), ygrid(1,     1)
```

```
    xgrid(end,   1), ygrid(end,   1)
    xgrid(1,   end), ygrid(1,   end)
    ];

t2 = [
    xgrid(end, end), ygrid(end, end)
    xgrid(end,   1), ygrid(end,   1)
    xgrid(1,   end), ygrid(1,   end)
    ];

is_inside = ...
    point_inside_triangle(t1, [x, y]) | ...
    point_inside_triangle(t2, [x, y]);

cloud = [x(is_inside), y(is_inside), z(is_inside)];
size_cloud_init = size(cloud, 1);

%% Create bins
count = 0;
bin = cell(size(xgrid, 1) - 1, size(ygrid, 2) - 1);
binmin = cell(size(xgrid, 1) - 1, size(ygrid, 2) - 1);
binmax = cell(size(xgrid, 1) - 1, size(ygrid, 2) - 1);
for row = 1:size(xgrid, 1) - 1
    for col = 1:size(ygrid, 2) - 1
        % Find the points inside the patch
        t1 = [
            xgrid(row    , col    ), ygrid(row    , col    )
            xgrid(row + 1, col    ), ygrid(row + 1, col    )
            xgrid(row    , col + 1), ygrid(row    , col + 1)
            ];
        t2 = [
            xgrid(row + 1, col + 1), ygrid(row + 1, col + 1)
            xgrid(row + 1, col    ), ygrid(row + 1, col    )
            xgrid(row    , col + 1), ygrid(row    , col + 1)
            ];
```

```
        is_inside = ...
            point_inside_triangle(t1, cloud(:, 1:2)) | ...
            point_inside_triangle(t2, cloud(:, 1:2));
        % Fill the bin
        bin(row, col) = {cloud(is_inside, :)};
        [~, idxmin] = min(bin{row, col}(:, 3));
        % Find the lowest and highest points of the bin
        pmin = bin{row, col}(idxmin, :);
        [~, idxmax] = max(bin{row, col}(:, 3));
        pmax = bin{row, col}(idxmax, :);
        binmin{row, col} = pmin;
        binmax{row, col} = pmax;
        % Discard the bin points from the cloud
        cloud(is_inside, :) = [];
        % Progress
        count = count + 1;
        fprintf('Progress: %5.1f%%  -  ', ...
            count/((size(xgrid, 1) - 1)*(size(ygrid, 2) - 1))*100)
        fprintf('Grouped %d out of %d points\n', ...
            size_cloud_init - size(cloud, 1), length(x))
    end
end

xyzmin = cell2mat(binmin(:));
xmin = xyzmin(:, 1);
ymin = xyzmin(:, 2);
zmin = xyzmin(:, 3);

xyzmax = cell2mat(binmax(:));
xmax = xyzmax(:, 1);
ymax = xyzmax(:, 2);
zmax = xyzmax(:, 3);

end
```

```
function is_inside = point_inside_triangle(vertices,point)

va = repmat(vertices(1,:),size(point,1),1);
vb = repmat(vertices(2,:),size(point,1),1);
vc = repmat(vertices(3,:),size(point,1),1);

is_inside = ...
    same_side(va,vb,vc,point) & ...
    same_side(vb,vc,va,point) & ...
    same_side(vc,va,vb,point);

end

function is_same_side = same_side(a,b,c,p)

ab = [b-a,zeros(size(p,1),1)];
ac = [c-a,zeros(size(p,1),1)];
ap = [p-a,zeros(size(p,1),1)];
n = cross(ab,repmat([0 0 1],size(p,1),1));
is_same_side = ...
    sign(dot(ac,n,2)) == ...
    sign(dot(ap,n,2));

end
```

Appendix B

Relative distribution of minimum power: additional figures

A selection of figures showing the relative distribution of minimum power (carpet) for further test conditions is reported below.

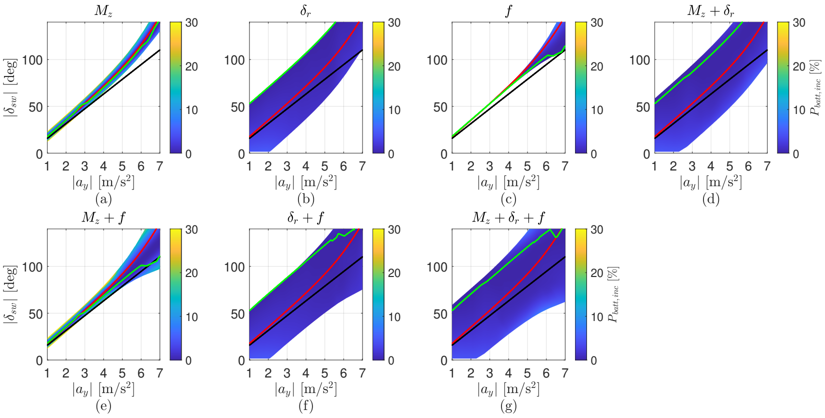

(a) (b) (c) (d) (e) (f) (g)

Figure B.1: Carpets for 2WD drivetrain. $V = 50$ km/h, $\mu_{\%} = 70\%$ and $a_x = 0$ m/s^2.

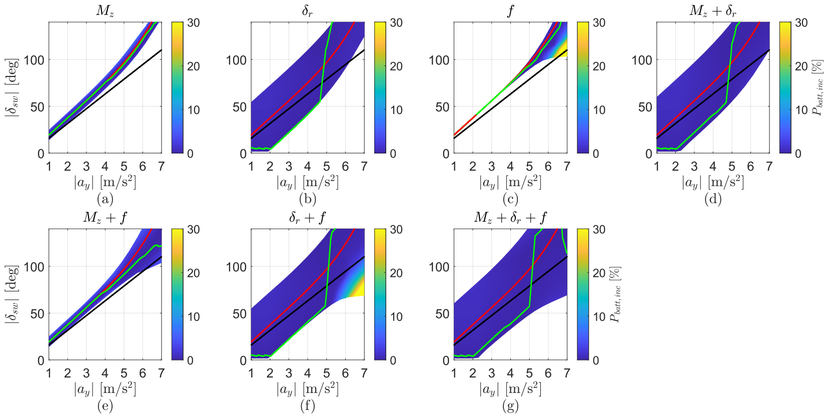

Figure B.2: Carpets for 2WD drivetrain. $V = 50$ km/h, $\mu_{\%} = 70\%$ and $a_x = 1.5$ m/s^2.

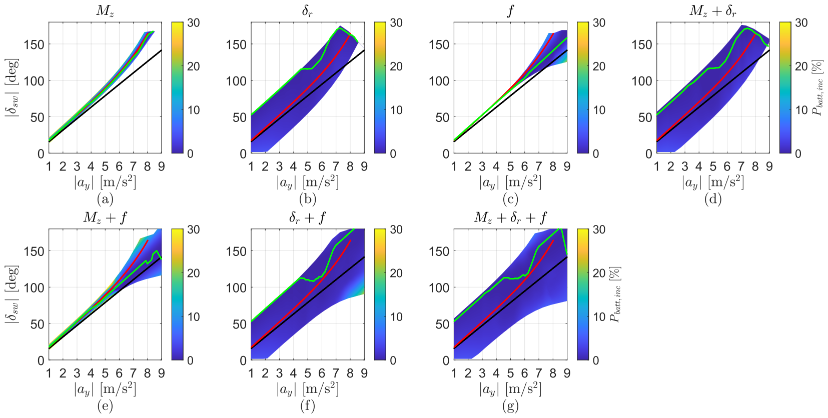

Figure B.3: Carpets for 2WD drivetrain. $V = 50$ km/h, $\mu_{\%} = 100\%$ and $a_x = 0$ m/s^2.

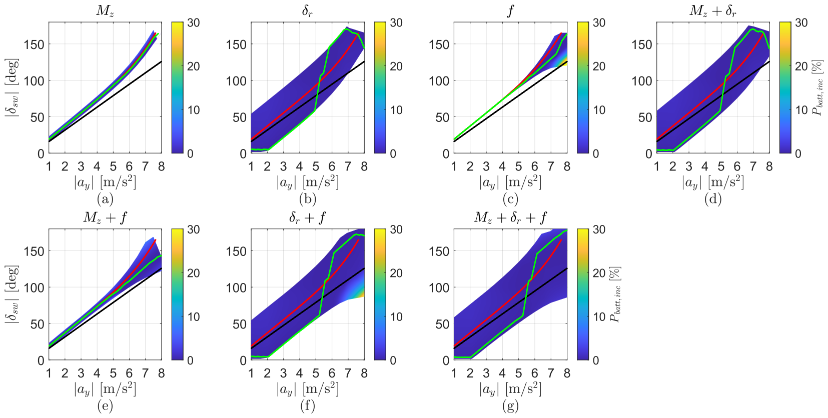

Figure B.4: Carpets for 2WD drivetrain. $V = 50$ km/h, $\mu_{\%} = 100\%$ and $a_x = 1.5$ m/s^2.

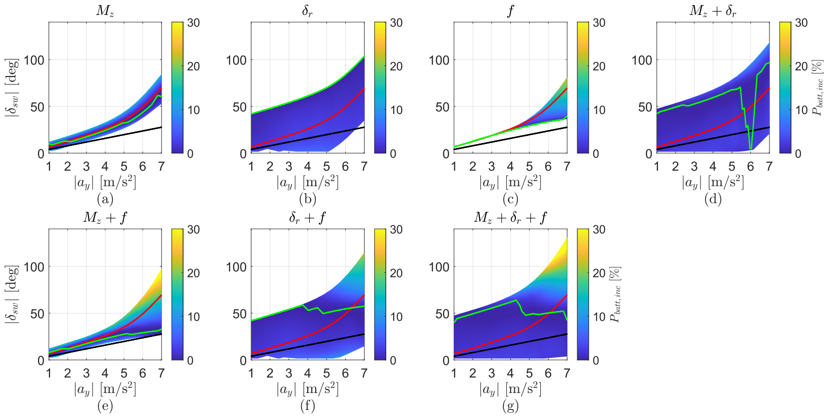

Figure B.5: Carpets for 2WD drivetrain. $V = 100$ km/h, $\mu_{\%} = 70\%$ and $a_x = 0$ m/s^2.

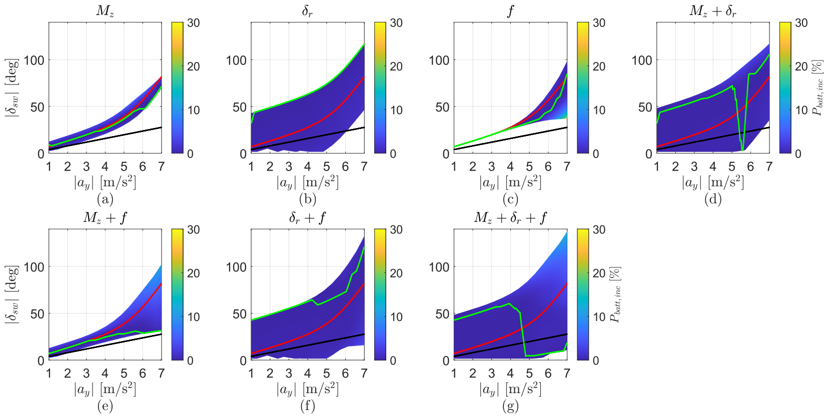

Figure B.6: Carpets for 2WD drivetrain. $V = 100$ km/h, $\mu_{\%} = 70\%$ and $a_x = 1.5$ m/s^2.

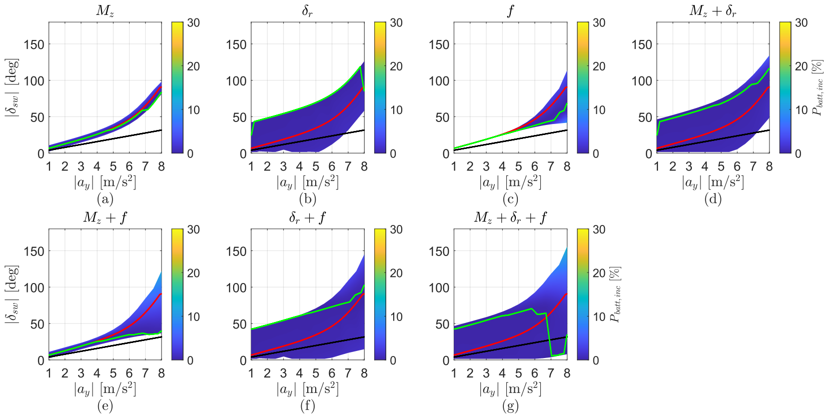

Figure B.7: Carpets for 2WD drivetrain. $V = 100$ km/h, $\mu_{\%} = 100\%$ and $a_x = 1.5$ m/s^2.

Appendix C

Relative profile of minimum power along the energy-efficient understeer characteristic: additional figures

A selection of figures showing for each combination of actuations the relative profile of minimum power along the energy-efficient understeer characteristic for further test conditions is reported below. Reference power profile belongs to the 4WD set-up with $M_z + \delta_r + f$.

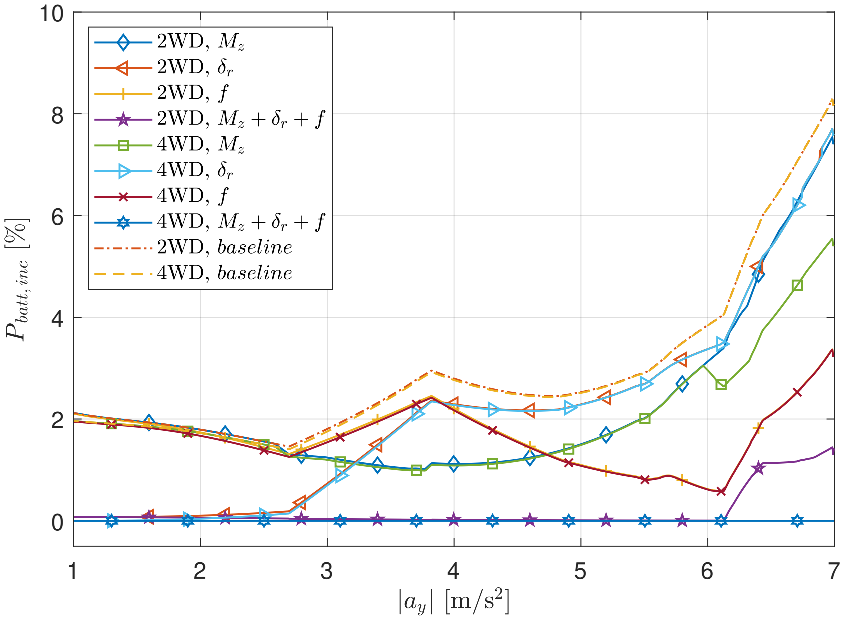

Figure C.1: Relative profile of minimum power along the energy-efficient understeer characteristic. Single actuations. $V = 50$ km/h, $\mu_{\%} = 70\%$ and $a_x = 0$ m/s^2.

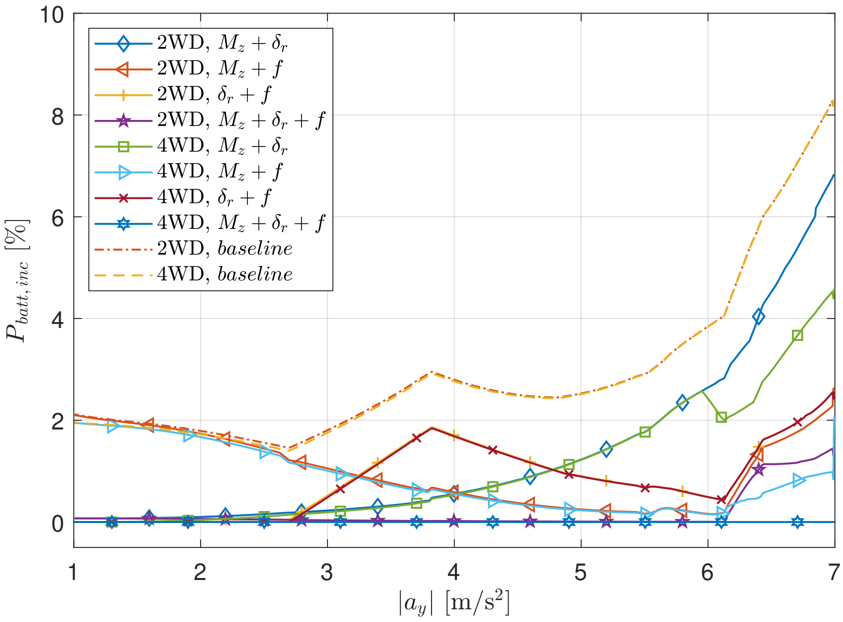

Figure C.2: Relative profile of minimum power along the energy-efficient understeer characteristic. Multiple actuations. $V = 50$ km/h, $\mu_{\%} = 70\%$ and $a_x = 0$ m/s^2.

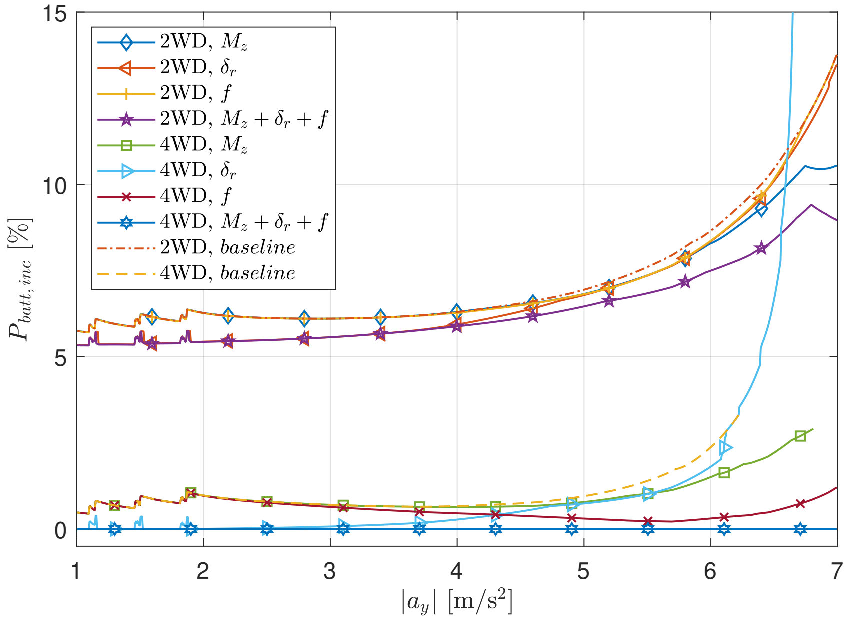

Figure C.3: Relative profile of minimum power along the energy-efficient understeer characteristic. Single actuations. $V = 50$ km/h, $\mu_{\%} = 70\%$ and $a_x = 1.5$ m/s^2.

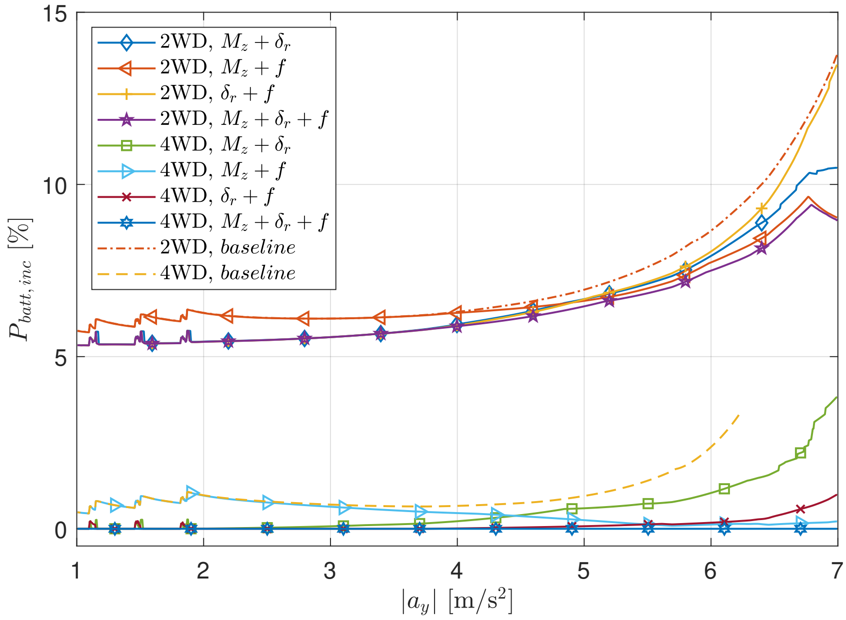

Figure C.4: Relative profile of minimum power along the energy-efficient understeer characteristic. Multiple actuations. $V = 50$ km/h, $\mu_{\%} = 70\%$ and $a_x = 1.5$ m/s^2.

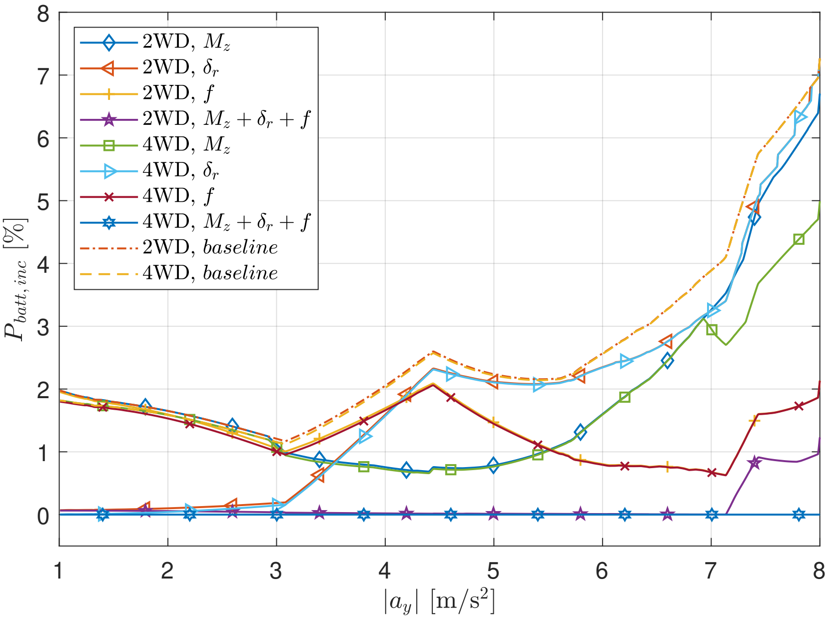

Figure C.5: Relative profile of minimum power along the energy-efficient understeer characteristic. Single actuations. $V = 50$ km/h, $\mu_{\%} = 100\%$ and $a_x = 0$ m/s^2.

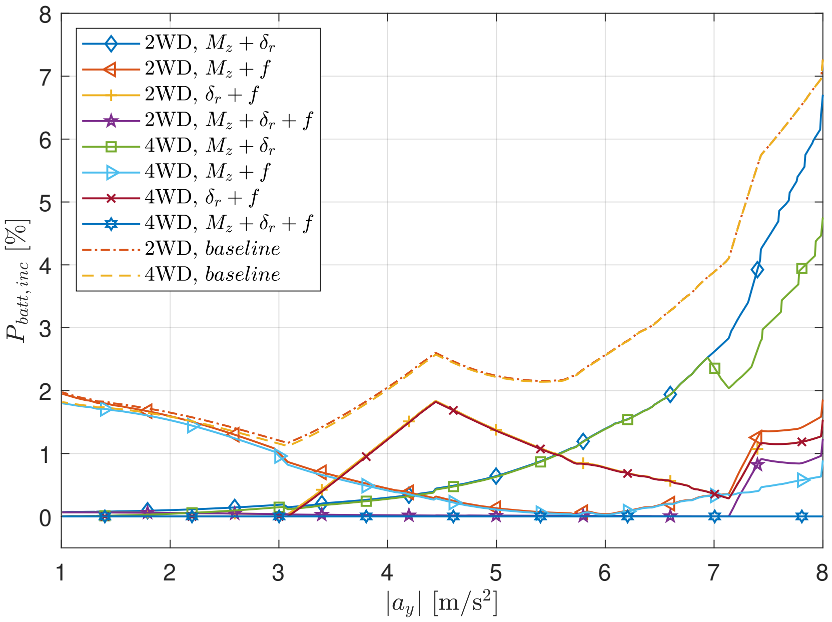

Figure C.6: Relative profile of minimum power along the energy-efficient understeer characteristic. Multiple actuations. $V = 50$ km/h, $\mu_{\%} = 100\%$ and $a_x = 0$ m/s^2.

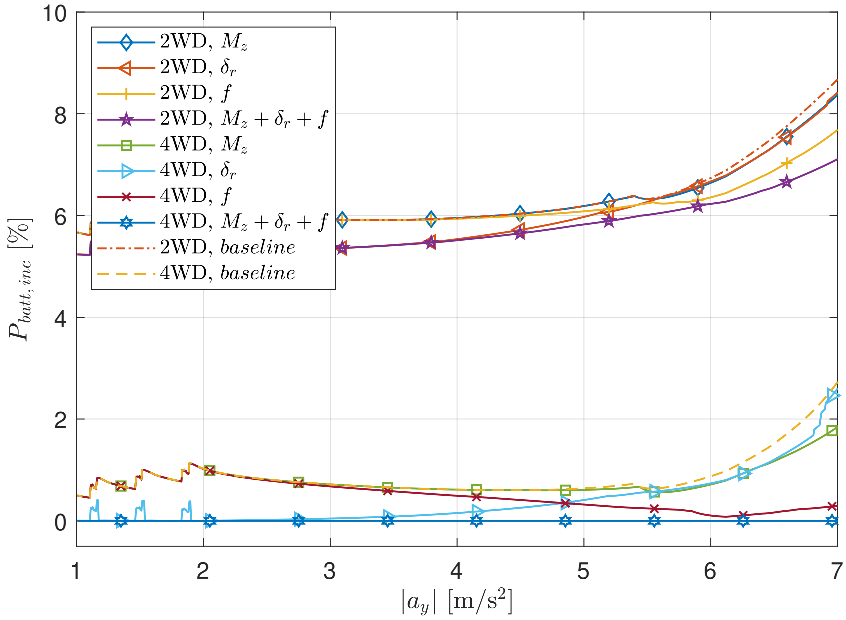

Figure C.7: Relative profile of minimum power along the energy-efficient understeer characteristic. Single actuations. $V = 50$ km/h, $\mu_{\%} = 100\%$ and $a_x = 1.5$ m/s^2.

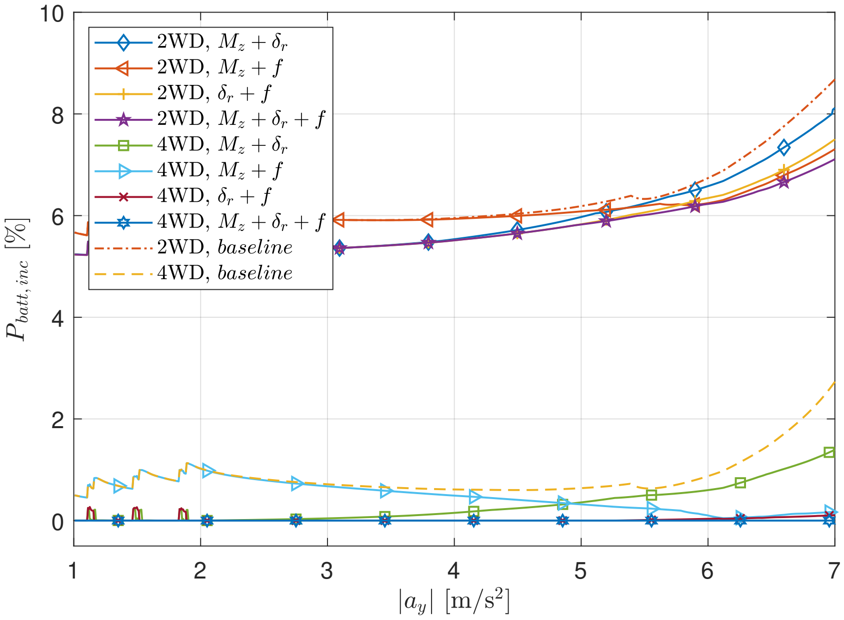

Figure C.8: Relative profile of minimum power along the energy-efficient understeer characteristic. Multiple actuations. $V = 50$ km/h, $\mu_{\%} = 100\%$ and $a_x = 1.5$ m/s^2.

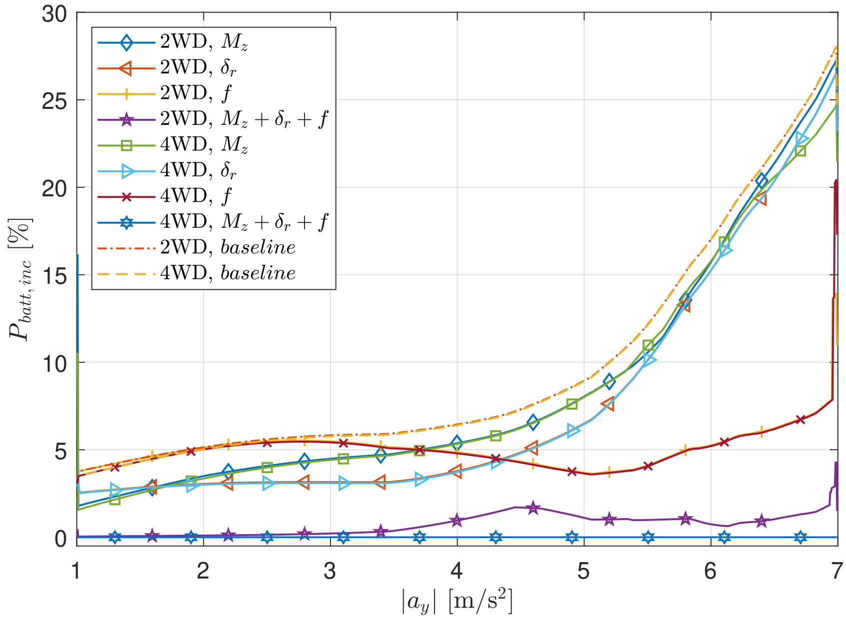

Figure C.9: Relative profile of minimum power along the energy-efficient understeer characteristic. Single actuations. $V = 100$ km/h, $\mu_{\%} = 70\%$ and $a_x = 0$ m/s^2.

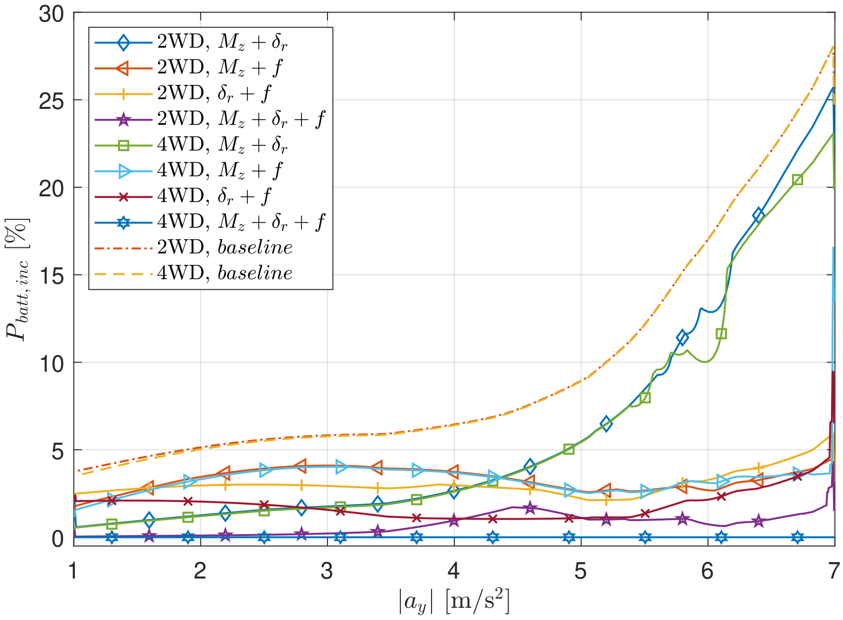

Figure C.10: Relative profile of minimum power along the energy-efficient understeer characteristic. Multiple actuations. $V = 100$ km/h, $\mu_{\%} = 70\%$ and $a_x = 0$ m/s^2.

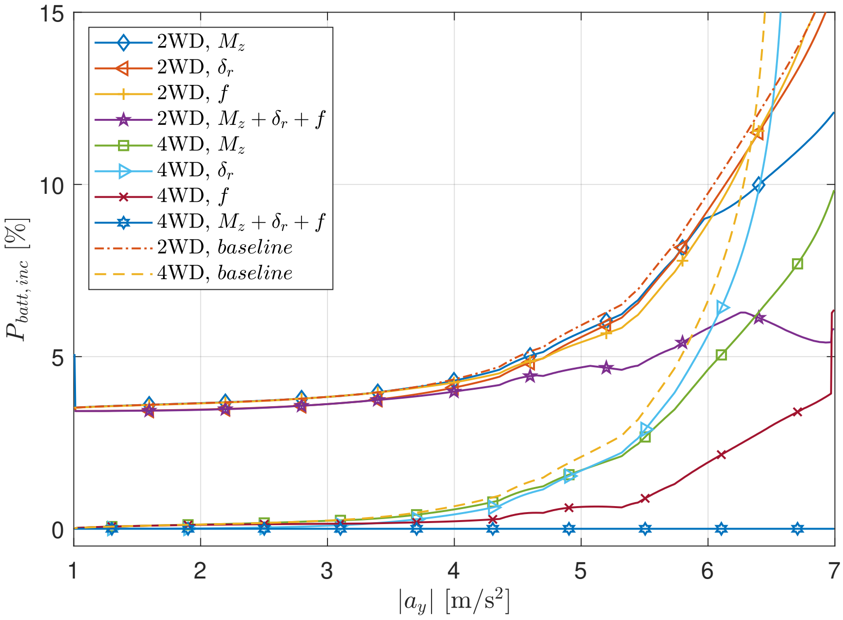

Figure C.11: Relative profile of minimum power along the energy-efficient understeer characteristic. Single actuations. $V = 100$ km/h, $\mu_{\%} = 70\%$ and $a_x = 1.5$ m/s^2.

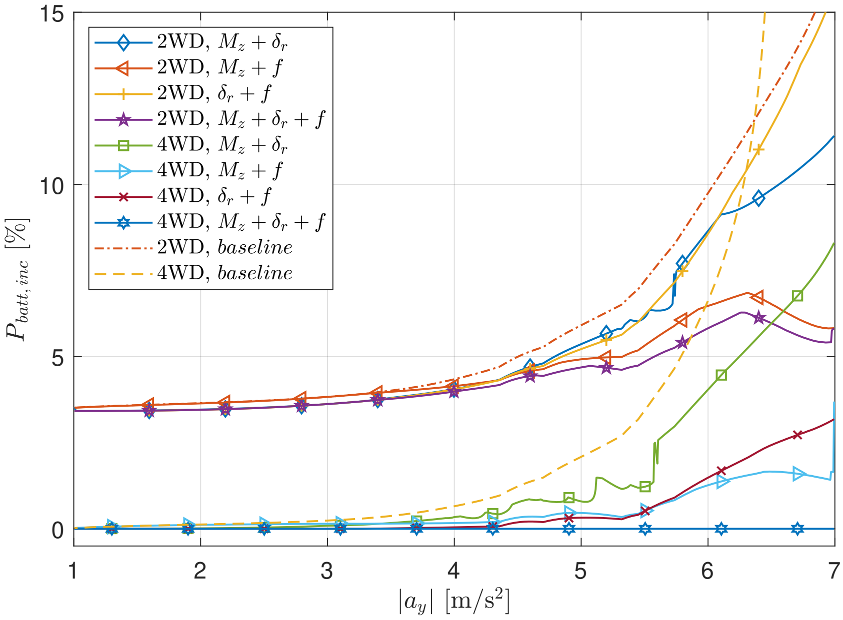

Figure C.12: Relative profile of minimum power along the energy-efficient understeer characteristic. Multiple actuations. $V = 100$ km/h, $\mu_{\%} = 70\%$ and $a_x = 1.5$ m/s^2.

Bibliography

[1] IEA (2020), Global EV Outlook 2020, IEA, Paris.

[2] Peter Weldon, Patrick Morrissey, and Margaret O'Mahony. Long-term cost of ownership comparative analysis between electric vehicles and internal combustion engine vehicles. *Sustainable Cities and Society*, 39:578–591, May 2018.

[3] Antti Lajunen, Panu Sainio, Lasse Laurila, Jenni Pippuri-Mäkeläinen, and Kari Tammi. Overview of Powertrain Electrification and Future Scenarios for Non-Road Mobile Machinery. *Energies*, 11(5):1184, May 2018.

[4] Yimin Gao and M. Ehsani. Parametric design of the traction motor and energy storage for series hybrid off-road and military vehicles. *IEEE Transactions on Power Electronics*, 21(3):749–755, May 2006.

[5] S. Grammatico, A. Balluchi, and E. Cosoli. A series-parallel hybrid electric powertrain for industrial vehicles. In *2010 IEEE Vehicle Power and Propulsion Conference*, pages 1–6, September 2010.

[6] G. P. Moreda, M. A. Muñoz-García, and P. Barreiro. High voltage electrification of tractor and agricultural machinery – A review. *Energy Conversion and Management*, 115:117 – 131, 2016.

[7] C. Jia, W. Qiao, and L. Qu. Modeling and Control of Hybrid Electric Vehicles: A Case Study for Agricultural Tractors. In *2018 IEEE Vehicle Power and Propulsion Conference (VPPC)*, pages 1–6, August 2018.

[8] G. C. David and L. Harper. Challenges of hybridisation of Off-Highway Machinery. In *6th Hybrid and Electric Vehicles Conference (HEVC 2016)*, pages 1–7, November 2016.

[9] R. V. Wagh and N. Sane. Electrification of heavy-duty and off-road vehicles. In *2015 IEEE International Transportation Electrification Conference (ITEC)*, pages 1–3, August 2015.

[10] *Regulation (EU) 2016/1628 of the European Parliament and of the Council of 14 September 2016 on requirements relating to gaseous and particulate pollutant emission limits and type-approval for internal combustion engines for non-road mobile machinery, amending Regulations (EU) No 1024/2012 and (EU) No 167/2013, and amending and repealing Directive 97/68/EC*. September 2016.

[11] M. Dalboni, P. Santarelli, P. Patroncini, A. Soldati, C. Concari, and D. Lusignani. Electrification of a Compact Agricultural Tractor: A Successful Case Study. In *2019 IEEE Transportation Electrification Conference and Expo (ITEC)*, pages 1–6, 2019.

[12] M. Tursini, F. Parasiliti, G. Fabri, and E. Della Loggia. A fault tolerant e-motor drive system for auxiliary services in hybrid electric light commercial vehicle. In *2014 IEEE International Electric Vehicle Conference (IEVC)*, pages 1–6, December 2014.

[13] E. A. Buning. Electric drives in agricultural machinery-approach from the tractor side. *Journal of Agricultural Engineering (New Delhi)*, 47(3):30–35, 2010.

[14] Guang Wu, Xing Zhang, and Zuomin Dong. Powertrain architectures of electrified vehicles: Review, classification and comparison. *Journal of the Franklin Institute*, 352(2):425 – 448, 2015.

[15] J. Wang, Z. Sun, and X. Wei. Performance and characteristic research in LiFePO4 battery for electric vehicle applications. In *2009 IEEE Vehicle Power and Propulsion Conference*, pages 1657–1661, September 2009.

[16] V. Ruiz, A. Pfrang, A. Kriston, N. Omar, P. Van den Bossche, and L. Boon-Brett. A review of international abuse testing standards and regulations for lithium ion batteries in electric and hybrid electric vehicles. *Renewable and Sustainable Energy Reviews*, 81:1427 – 1452, 2018.

[17] G. Gruosso. Optimization and management of energy power flow in hybrid electrical vehicles. In *5th IET Hybrid and Electric Vehicles Conference (HEVC 2014)*, pages 1–5, November 2014.

[18] Anthony Barré, Benjamin Deguilhem, Sébastien Grolleau, Mathias Gérard, Frédéric Suard, and Delphine Riu. A review on lithium-ion battery ageing mechanisms and estimations for automotive applications. *Journal of Power Sources*, 241:680 – 689, 2013.

[19] Leonardo De Novellis, Aldo Sorniotti, Patrick Gruber, Javier Orus, Jose-Manuel Rodriguez Fortun, Johan Theunissen, and Jasper De Smet. Direct yaw moment control actuated through electric drivetrains and friction brakes: Theoretical design and experimental assessment. *Mechatronics*, 26:1–15, March 2015.

[20] Kazuhiko Shimada and Yasuji Shibahata. Comparison of Three Active Chassis Control Methods for Stabilizing Yaw Moments. page 940870, March 1994.

[21] C. Chatzikomis, M. Zanchetta, P. Gruber, A. Sorniotti, B. Modic, T. Motaln, L. Blagotinsek, and G. Gotovac. An energy-efficient torque-vectoring algorithm for electric vehicles with multiple motors. *Mechanical Systems and Signal Processing*, 128:655–673, August 2019.

[22] Zhongliang Han, Nan Xu, Hong Chen, Yanjun Huang, and Bin Zhao. Energy-efficient control of electric vehicles based on linear quadratic regulator and phase plane analysis. *Applied Energy*, 213:639–657, March 2018.

[23] Xiao Hu, Ping Wang, Yunfeng Hu, and Hong Chen. A stability-guaranteed and energy-conserving torque distribution strategy for electric vehicles under extreme conditions. *Applied Energy*, 259:114162, February 2020.

[24] A.M. Dizqah, B.L. Ballard, M.V. Blundell, S. Kanarachos, and M.S. Innocente. A Non-Convex Control Allocation Strategy as Energy-Efficient Torque Distributors for On-Road and Off-Road Vehicles. *Control Engineering Practice*, 95:104256, February 2020.

[25] G. De Filippis, B. Lenzo, A. Sorniotti, K. Sannen, J. De Smet, and P. Gruber. On the Energy Efficiency of Electric Vehicles with Multiple Motors. In *2016 IEEE Vehicle Power and Propulsion Conference (VPPC)*, pages 1–6, 2016.

[26] G. De Filippis, B. Lenzo, A. Sorniotti, P. Gruber, and W. De Nijs. Energy-Efficient Torque-Vectoring Control of Electric Vehicles With Multiple Drivetrains. *IEEE Transactions on Vehicular Technology*, 67(6):4702–4715, 2018.

[27] Johannes Edrén, Mats Jonasson, Jenny Jerrelind, Annika Stensson Trigell, and Lars Drugge. Energy efficient cornering using over-actuation. *Mechatronics*, 59:69–81, May 2019.

[28] Francis B Hoogterp, Joseph H Beno, and Damon A Weeks. An energy efficient electromagnetic active suspension system. *SAE transactions*, pages 536–540, 1997. Publisher: JSTOR.

[29] Jaroslaw Konieczny, Janusz Kowal, Waldemar Raczka, and Marek Sibielak. Bench Tests of Slow and Full Active Suspensions in Terms of Energy Consumption. *Journal of Low Frequency Noise, Vibration and Active Control*, 32(1-2):81–98, March 2013.

[30] Guimin Long, Fei Ding, Nong Zhang, Jie Zhang, and An Qin. Regenerative active suspension system with residual energy for in-wheel motor driven electric vehicle. *Applied Energy*, 260:114180, February 2020.

[31] Matteo Dalboni, Dario Mangoni, Alessandro Soldati, Francesco Corradini, Alessandro Tasora, Filippo Savi, and Davide Lusignani. A fast and lightweight dynamics model oriented to electric vehicle design. In *IECON 2017 - 43rd Annual Conference of the IEEE Industrial Electronics Society*, pages 4603–4608, Beijing, October 2017. IEEE.

[32] Alessandro Soldati, Giorgio Pietrini, University of Parma, Matteo Dalboni, University of Parma, and Carlo Concari. Electric-Vehicle Power Converters Model-Based Design-for-Reliability. *CPSS Transactions on Power Electronics and Applications*, 3(2):102–110, June 2018.

[33] Matteo Dalboni, Dario Mangoni, Davide Lusignani, and Alessandro Soldati. Lightweight dynamic vehicle models oriented to vehicle electrification. *International Journal of Vehicle Performance*, 5(1):40, 2019.

[34] Matteo Dalboni and Alessandro Soldati. Soft-Body Modeling: A Scalable and Efficient Formulation for Control-Oriented Simulation of Electric Vehicles. In *2019 IEEE Transportation Electrification Conference and Expo (ITEC)*, pages 1–6, Detroit, MI, USA, June 2019. IEEE.

[35] F. Zendri, R. Antonello, F. Biral, and H. Fujimoto. Modeling, identification and validation of an electric vehicle for model-based control design. In *2010 11th IEEE International Workshop on Advanced Motion Control (AMC)*, pages 118–123, March 2010.

[36] Y. Hirano. Model based development of an integrated control of front steering and torque vectoring differential gear system. In *2016 55th Annual Conference of the Society of Instrument and Control Engineers of Japan (SICE)*, pages 11–16, September 2016.

[37] S. Koehler, A. Viehl, O. Bringmann, and W. Rosenstiel. Energy-Efficiency Optimization of Torque Vectoring Control for Battery Electric Vehicles. *IEEE Intelligent Transportation Systems Magazine*, 9(3):59–74, 2017.

[38] E. Siampis, E. Velenis, and S. Longo. Model Predictive torque vectoring control for electric vehicles near the limits of handling. In *2015 European Control Conference (ECC)*, pages 2553–2558, 2015.

[39] E. Siampis, E. Velenis, and S. Longo. Predictive rear wheel torque vectoring control with terminal understeer mitigation using nonlinear estimation. In *2015 54th IEEE Conference on Decision and Control (CDC)*, pages 4302–4307, 2015.

[40] Hongliang Yuan, Dong Zhang, and T. J. Gordon. Road vehicle rollover prevention torque vectoring via model predictive control. pages 9401–9406. IEEE, July 2017.

[41] Mike Blundell and D Harty. The Multibody Systems Approach to Vehicle Dynamics. *The Multibody Systems Approach to Vehicle Dynamics*, pages 1–741, 2014.

[42] Rigs of Rods Contributors. *Rigs of Rods*. 2016.

[43] BeamNG GmbH. *BeamNG.Research*. 2018.

[44] Ahmed A. Shabana. *Dynamics of multibody systems*. Cambridge University Press, New York, fourth edition edition, 2014.

[45] F. Zhao and B. G. M. van Wachem. A novel Quaternion integration approach for describing the behaviour of non-spherical particles. *Acta Mechanica*, 224(12):3091–3109, December 2013.

[46] Michel Géradin and Alberto Cardona. *Flexible multibody dynamics: a finite element approach*. John Wiley, New York, 2001.

[47] M. Gander and G. Wanner. From Euler, Ritz, and Galerkin to Modern Computing. *SIAM Review*, 54(4):627–666, 2012.

[48] O.C. Zienkiewicz, R.L. Taylor, and J.Z. Zhu. *The Finite Element Method: Its Basis and Fundamentals*. Elsevier Science, 2005.

[49] Alessandro Tasora, Radu Serban, Hammad Mazhar, Arman Pazouki, Daniel Melanz, Jonathan Fleischmann, Michael Taylor, Hiroyuki Sugiyama, and Dan Negrut. Chrono: An Open Source Multi-physics Dynamics Engine. In *HPCSE*, 2015.

[50] A Nealen, Matthias Müller, Richard Keiser, Eddy Boxerman, and M Carlson. Physically based deformable models in computer graphics. *Eurographics: State of the Art Report*, pages 71–94, 2005.

[51] G. San-Vicente, I. Aguinaga, and J. T. Celigueta. Cubical Mass-Spring Model Design Based on a Tensile Deformation Test and Nonlinear Material Model. *IEEE Transactions on Visualization and Computer Graphics*, 18(2):228–241, February 2012.

[52] Michael Gipser. FTire: 10 Years of Development and Application. 2019.

[53] H. B. Pacejka. *Tyre and vehicle dynamics*. Butterworth-Heinemann, Oxford, 2nd ed edition, 2006.

[54] Carlos Canudas-de Wit, Panagiotis Tsiotras, Efstathios Velenis, Michel Basset, and Gerard Gissinger. Dynamic Friction Models for Road/Tire Longitudinal Interaction. *Vehicle System Dynamics*, 39(3):189–226, 2003.

[55] Georg Rill. *Road Vehicle Dynamics: Fundamentals and Modeling*. CRC Press, 0 edition, September 2011.

[56] Luis Rodolfo García Carrillo, Alejandro Enrique Dzul López, Rogelio Lozano, and Claude Pégard. Modeling the Quad-Rotor Mini-Rotorcraft. In *Quad Rotorcraft Control*, pages 23–34. Springer London, London, 2013.

[57] E Bakker, L Nyborg, and H.B. Pacejka. Tyre Modeling for Use in Vehicle Dynamics Studies. 1987.

[58] Tejas Kinjawadekar, Neha Dixit, Gary J. Heydinger, Dennis A. Guenther, and Mohamed Kamel Salaani. Vehicle Dynamics Modeling and Validation of the 2003 Ford Expedition with ESC using CarSim. 2009.

[59] Jeffery R Anderson and E Harry Law. Fuzzy logic approach to vehicle stability control of oversteer. *SAE International Journal of Passenger Cars-Mechanical Systems*, 4(2011-01-0268):241–250, 2011.

[60] Mustafa Ali Arat, Kanwar Singh, and Saied Taheri. An adaptive vehicle stability control algorithm based on tire slip-angle estimation. Technical report, SAE Technical Paper, 2012.

[61] Jian Zhao and Saied Taheri. A multi-objective LMI-based antiroll control system. *SAE International Journal of Commercial Vehicles*, 5(2012-01-1904):421–428, 2012.

[62] Seyed Hossein Tamaddoni, Saied Taheri, and Mehdi Ahmadian. Robust optimal control of vehicle lateral motion with driver-in-the-loop. Technical report, SAE Technical Paper, 2012.

[63] R R. Ryan. ADAMS — Multibody System Analysis Software. pages 361–402. 1990.

[64] Alexander Eichberger. Prozesssichere Modellreduzierung: Der Schlüssel zur Echtzeit und effizienten MKS-Simulation in der Fahrzeugdynamik 1. 2019.

[65] Stephan Ziegler and Robert Höpler. Extending the IPG CarMaker by FMI Compliant Units. 2011.

[66] Pierangelo Masarati, Marco Morandini, and Paolo Mantegazza. An Efficient Formulation for General-Purpose Multibody/Multiphysics Analysis. *Journal of Computational and Nonlinear Dynamics*, 9(4):041001–041001–9, July 2014.

[67] Erwin Coumans. Bullet Physics Simulation. In *ACM SIGGRAPH 2015 Courses*, SIGGRAPH '15, New York, NY, USA, 2015. ACM.

[68] R Smith. ODE: Open dynamics engine. 2009.

[69] E Fischer. Standard multi-body system software in the vehicle development process. *Proceedings of The Institution of Mechanical Engineers Part K-journal of Multi-body Dynamics - PROC INST MECH ENG K-J MUL D*, 221, 2007.

[70] J. D. Setiawan, M. Safarudin, and A. Singh. Modeling, simulation and validation of 14 DOF full vehicle model. In *International Conference on Instrumentation, Communication, Information Technology, and Biomedical Engineering 2009*, pages 1–6, November 2009.

[71] Z.A. Kadir, K. Hudha, F. Ahmad, Mohamad Faizal Abdullah, A.R. Norwazan, M.Y. Mohd Fazli, A.J. Khalid, and M. Gunasilan. Verification of 14DOF Full Vehicle Model Based on Steering Wheel Input. In *Trends in Automotive Research*, volume 165 of *Applied Mechanics and Materials*, pages 109–113. Trans Tech Publications Ltd, 2012.

[72] H. Sun, H. Wang, and X. Zhao. Line Braking Torque Allocation Scheme for Minimal Braking Loss of Four-Wheel-Drive Electric Vehicles. *IEEE Transactions on Vehicular Technology*, 68(1):180–192, January 2019.

[73] L. Guo, X. Lin, P. Ge, Y. Qiao, L. Xu, and J. Li. Torque distribution for electric vehicle with four in-wheel motors by considering energy optimization and dynamics performance. In *2017 IEEE Intelligent Vehicles Symposium (IV)*, pages 1619–1624, June 2017.

[74] Y. Guodong, Z. Chengjie, and Z. Ning. The torque distribution and anti-slip regulation control for two-wheel independent drive electric vehicle. In *2016 Chinese Control and Decision Conference (CCDC)*, pages 4444–4449, May 2016.

[75] Javier Cuadrado, Daniel Dopico, Jose A. Perez, and Roland Pastorino. Automotive observers based on multibody models and the extended Kalman filter. *Multibody System Dynamics*, 27(1):3–19, January 2012.

[76] C. Lin and L. Zhang. Hardware-in-the-loop simulation and its application in electric vehicle development. In *2008 IEEE Vehicle Power and Propulsion Conference*, pages 1–6, September 2008.

[77] Andreas Vath, Zijad Lemĕs, Hubert Mächer, Matthias Söhn, Norbert Nicoloso, and Thomas Hartkopf. Dynamic modelling and hardware-in-the-loop testing of PEMFC. *Journal of Power Sources*, 157(2):816 – 827, 2006.

[78] Taichi Shiiba and Yoshihiro Suda. Evaluation of driver's behavior with multibody-based driving simulator. *Multibody System Dynamics*, 17(2):195–208, April 2007.

[79] R. Marino, S. Scalzi, G. Orlando, and M. Netto. A nested PID steering control for lane keeping in vision based autonomous vehicles. In *2009 American Control Conference*, pages 2885–2890, June 2009.

[80] Junmin Wang, J. Steiber, and B. Surampudi. Autonomous ground vehicle control system for high-speed and safe operation. In *2008 American Control Conference*, pages 218–223, June 2008.

[81] M. Durali, G. A. Javid, and A. Kasaiezadeh. Collision avoidance maneuver for an autonomous vehicle. In *9th IEEE International Workshop on Advanced Motion Control, 2006.*, pages 249–254, March 2006.

[82] João P. C. Gonçalves and Jorge A. C. Ambrósio. Optimization of Vehicle Suspension Systems for Improved Comfort of Road Vehicles Using Flexible Multibody Dynamics. *Nonlinear Dynamics*, 34(1):113–131, October 2003.

[83] Antonio Recuero, Radu Serban, Bryan Peterson, Hiroyuki Sugiyama, Paramsothy Jayakumar, and Dan Negrut. A high-fidelity approach for vehicle mobility simulation: Nonlinear finite element tires operating on granular material. *Journal of Terramechanics*, 72:39 – 54, 2017.

[84] H. Yu, F. Cheli, and F. Castelli-Dezza. Optimal Design and Control of 4-IWD Electric Vehicles Based on a 14-DOF Vehicle Model. *IEEE Transactions on Vehicular Technology*, 67(11):10457–10469, November 2018.

[85] Y. Zhao, J. Ni, and J. Hu. Research on Independent Driving Electric Vehicle in the Pivot Steering and Experimental Validation. In *2018 IEEE Intelligent Vehicles Symposium (IV)*, pages 880–885, June 2018.

[86] Y. Song, H. Shu, X. Chen, and S. Luo. Direct-yaw-moment control of four-wheel-drive electrical vehicle based on lateral tyre–road forces and sideslip angle observer. *IET Intelligent Transport Systems*, 13(2):303–312, 2019.

[87] Michael Gipser. FTire - The tire simulation model for all applications related to vehicle dynamics. *Vehicle System Dynamics - VEH SYST DYN*, 45:139–151, 2007.

[88] Michael Gipser. FTire: A physically based application-oriented tyre model for use with detailed MBS and finite-element suspension models. *Vehicle System Dynamics*, 43:76–91, 2005.

[89] Anton Riepl, Werner Reinalter, and Markus Schmid. Application of the tyre model FTire in the vehicle development process at MAGNA STEYR Fahrzeugtechnik. *Vehicle System Dynamics*, 43(sup1):370–383, 2005.

[90] Leonardo De Novellis, Aldo Sorniotti, and Patrick Gruber. Optimal Wheel Torque Distribution for a Four-Wheel-Drive Fully Electric Vehicle. *SAE International Journal of Passenger Cars - Mechanical Systems*, 6(1):128–136, April 2013.

[91] Leonardo De Novellis, Aldo Sorniotti, and Patrick Gruber. Driving modes for designing the cornering response of fully electric vehicles with multiple motors. *Mechanical Systems and Signal Processing*, 64-65:1–15, December 2015.

[92] Mats Jonasson, Johan Andreasson, Stefan Solyom, Bengt Jacobson, and Annika Stensson Trigell. Utilization of Actuators to Improve Vehicle Stability at the Limit: From Hydraulic Brakes Toward Electric Propulsion. *Journal of Dynamic Systems, Measurement, and Control*, 133(051003), July 2011.

[93] J. Kang, J. Yoo, and K. Yi. Driving Control Algorithm for Maneuverability, Lateral Stability, and Rollover Prevention of 4WD Electric Vehicles With Independently Driven Front and Rear Wheels. *IEEE Transactions on Vehicular Technology*, 60(7):2987–3001, 2011.

[94] Qian Lu, Pierangelo Gentile, Antonio Tota, Aldo Sorniotti, Patrick Gruber, Fabio Costamagna, and Jasper De Smet. Enhancing vehicle cornering limit through sideslip and yaw rate control. *Mechanical Systems and Signal Processing*, 75:455–472, June 2016.

[95] Andrew Pennycott, Leonardo De Novellis, Patrick Gruber, and Aldo Sorniotti. Sources of power loss during torque-vectoring for fully electric vehicles. *International Journal of Vehicle Design*, 67(2):157, 2015.

[96] J. Tjonnas and T. A. Johansen. Stabilization of Automotive Vehicles Using Active Steering and Adaptive Brake Control Allocation. *IEEE Transactions on Control Systems Technology*, 18(3):545–558, 2010.

[97] A. M. Dizqah, B. Lenzo, A. Sorniotti, P. Gruber, S. Fallah, and J. De Smet. A Fast and Parametric Torque Distribution Strategy for Four-Wheel-Drive Energy-Efficient Electric Vehicles. *IEEE Transactions on Industrial Electronics*, 63(7):4367–4376, 2016.

[98] Rongrong Wang, Yan Chen, Daiwei Feng, Xiaoyu Huang, and Junmin Wang. Development and performance characterization of an electric ground vehicle with independently actuated in-wheel motors. *Journal of Power Sources*, 196(8):3962–3971, April 2011.

[99] Y. Chen and J. Wang. Adaptive Energy-Efficient Control Allocation for Planar Motion Control of Over-Actuated Electric Ground Vehicles. *IEEE Transactions on Control Systems Technology*, 22(4):1362–1373, 2014.

[100] Andrew Pennycott, Leonardo De Novellis, Alessio Sabbatini, Patrick Gruber, and Aldo Sorniotti. Reducing the motor power losses of a four-wheel drive, fully electric vehicle via wheel torque allocation. *Proceedings of the Institution of Mechanical Engineers, Part D: Journal of Automobile Engineering*, 228(7):830–839, June 2014.

[101] X. Yuan and J. Wang. Torque Distribution Strategy for a Front- and Rear-Wheel-Driven Electric Vehicle. *IEEE Transactions on Vehicular Technology*, 61(8):3365–3374, 2012.

[102] H. Fujimoto and S. Harada. Model-Based Range Extension Control System for Electric Vehicles With Front and Rear Driving–Braking Force Distributions. *IEEE Transactions on Industrial Electronics*, 62(5):3245–3254, 2015.

[103] Peikun Sun, Annika Stensson Trigell, Lars Drugge, and Jenny Jerrelind. Energy-Efficient Direct Yaw Moment Control for In-Wheel Motor Electric Vehicles Utilising Motor Efficiency Maps. *Energies*, 13(3):593, January 2020.

[104] L. De Novellis, A. Sorniotti, and P. Gruber. Wheel Torque Distribution Criteria for Electric Vehicles With Torque-Vectoring Differentials. *IEEE Transactions on Vehicular Technology*, 63(4):1593–1602, 2014.

[105] Takao Kobayashi, Etsuo Katsuyama, Hideki Sugiura, Eiichi Ono, and Masaki Yamamoto. Efficient direct yaw moment control: tyre slip power loss minimisation for four-independent wheel drive vehicle. *Vehicle System Dynamics*, 56(5):719–733, May 2018.

[106] Yuta Suzuki, Yoshio Kano, and Masato Abe. A study on tyre force distribution controls for full drive-by-wire electric vehicle. *Vehicle System Dynamics*, 52(sup1):235–250, May 2014.

[107] Takao Kobayashi, Etsuo Katsuyama, Hideki Sugiura, Eiichi Ono, and Masaki Yamamoto. Efficient Direct Yaw Moment Control during Acceleration and Deceleration while Turning (First Report). pages 2016–01–1674, April 2016.

[108] G. Cui, X. Shang, Z. Li, F. Ning, and X. Wu. Lateral Stability Control of Four-wheel Steering Vehicles. In *2019 3rd Conference on Vehicle Control and Intelligence (CVCI)*, pages 1–5, 2019.

[109] N. Hamzah, M. K. Aripin, Y. M. Sam, H. Selamat, and M. F. Ismail. Yaw stability improvement for four-wheel active steering vehicle using sliding mode

control. In *2012 IEEE 8th International Colloquium on Signal Processing and its Applications*, pages 127–132, 2012.

[110] Fengchen Wang and Yan Chen. Hierarchical Input-Output Decoupling Control for Vehicle Rollover Mitigation. In *Volume 1: Advances in Control Design Methods; Advances in Nonlinear Control; Advances in Robotics; Assistive and Rehabilitation Robotics; Automotive Dynamics and Emerging Powertrain Technologies; Automotive Systems; Bio Engineering Applications; Bio-Mechatronics and Physical Human Robot Interaction; Biomedical and Neural Systems; Biomedical and Neural Systems Modeling, Diagnostics, and Healthcare*, page V001T09A005, Atlanta, Georgia, USA, September 2018. American Society of Mechanical Engineers.

[111] B. Yang, M. Wan, and Q. Sun. Control Strategy for Four-Wheel Steering Vehicle Handling Stability Based on Partial Decoupling Design. In *2010 Third International Joint Conference on Computational Science and Optimization*, volume 1, pages 265–267, 2010.

[112] Fengchen Wang, Peidong Xu, Ao Li, and Yan Chen. Energy Optimization of Lateral Motions for Autonomous Ground Vehicles With Four-Wheel Steering Control. In *Volume 1: Advanced Driver Assistance and Autonomous Technologies; Advances in Control Design Methods; Advances in Robotics; Automotive Systems; Design, Modeling, Analysis, and Control of Assistive and Rehabilitation Devices; Diagnostics and Detection; Dynamics and Control of Human-Robot Systems; Energy Optimization for Intelligent Vehicle Systems; Estimation and Identification; Manufacturing*, page V001T08A002, Park City, Utah, USA, October 2019. American Society of Mechanical Engineers.

[113] J. Na, Y. Huang, X. Wu, G. Gao, G. Herrmann, and J. Z. Jiang. Active Adaptive Estimation and Control for Vehicle Suspensions With Prescribed Performance. *IEEE Transactions on Control Systems Technology*, 26(6):2063–2077, 2018.

[114] Ming Chang Chen, Wei-Yen Wang, Shun-Feng Su, and Yi Hsing Chien. Robust T-S Fuzzy-Neural Control of Uncertain Active Suspension Systems. *International Journal of Fuzzy Systems*, 12:321–329, 2010.

[115] D. E. Williams and W. M. Haddad. Nonlinear control of roll moment distribution to influence vehicle yaw characteristics. *IEEE Transactions on Control Systems Technology*, 3(1):110–116, 1995.

[116] M. Ricco, M. Zanchetta, G. C. Rizzo, D. Tavernini, A. Sorniotti, C. Chatzikomis, M. Velardocchia, M. Geraerts, and M. Dhaens. On the Design of Yaw Rate Control via Variable Front-to-Total Anti-Roll Moment Distribution. *IEEE Transactions on Vehicular Technology*, 69(2):1388–1403, 2020.

[117] Mark O. Bodie and Aleksander Hac. Closed Loop Yaw Control of Vehicles Using Magneto-Rheological Dampers. pages 2000–01–0107, March 2000.

[118] P.H. Cronjé and P.S. Els. Improving off-road vehicle handling using an active anti-roll bar. *Journal of Terramechanics*, 47(3):179–189, June 2010.

[119] Ammar A. Aldair and Weiji Wang. The Energy Regeneration of Electromagnetic Energy Saving Active Suspension in Full Vehicle with Neurofuzzy Controller. *International Journal of Artificial Intelligence & Applications*, 2:32–43, 2011.

[120] Long Chen, Dehua Shi, Ruochen Wang, and Huawei Zhou. Energy Conservation Analysis and Control of Hybrid Active Semiactive Suspension with Three Regulating Damping Levels. *Shock and Vibration*, 2016:1–14, 2016.

[121] Aleksander Hac and Mark O. Bodie. Improvements in vehicle handling through integrated control of chassis systems. *International Journal of Vehicle Autonomous Systems*, 1(1):83, 2002.

[122] Arash Hosseinian Ahangarnejad, Stefano Melzi, and Mehdi Ahmadian. Integrated Vehicle Dynamics System through Coordinating Active Aerodynamics Control, Active Rear Steering, Torque Vectoring and Hydraulically In-

terconnected Suspension. *International Journal of Automotive Technology*, 20(5):903–915, October 2019.

[123] B. Lenzo, M. Zanchetta, A. Sorniotti, P. Gruber, and W. De Nijs. Yaw Rate and Sideslip Angle Control Through Single Input Single Output Direct Yaw Moment Control. *IEEE Transactions on Control Systems Technology*, pages 1–16, 2020.

[124] Ningyuan Guo, Xudong Zhang, Yuan Zou, Basilio Lenzo, Tao Zhang, and Dietmar Göhlich. A fast model predictive control allocation of distributed drive electric vehicles for tire slip energy saving with stability constraints. *Control Engineering Practice*, 102:104554, September 2020.

[125] Zhengyuan Wang, Umberto Montanaro, Saber Fallah, Aldo Sorniotti, and Basilio Lenzo. A gain scheduled robust linear quadratic regulator for vehicle direct yaw moment Control. *Mechatronics*, 51:31–45, May 2018.

[126] E. Siampis, E. Velenis, S. Gariuolo, and S. Longo. A Real-Time Nonlinear Model Predictive Control Strategy for Stabilization of an Electric Vehicle at the Limits of Handling. *IEEE Transactions on Control Systems Technology*, 26(6):1982–1994, 2018.

[127] N. Guo, B. Lenzo, X. Zhang, Y. Zou, R. Zhai, and T. Zhang. A Real-Time Nonlinear Model Predictive Controller for Yaw Motion Optimization of Distributed Drive Electric Vehicles. *IEEE Transactions on Vehicular Technology*, 69(5):4935–4946, 2020.

[128] Bin Zhao, Nan Xu, Hong Chen, Konghui Guo, and Yanjun Huang. Stability control of electric vehicles with in-wheel motors by considering tire slip energy. *Mechanical Systems and Signal Processing*, 118:340–359, March 2019.

[129] Johannes Gerhard, Maria-Christina Laiou, Martin Monnigmann, Wolfgang Marquardt, Mohsen Lakehal-Ayat, Edo Aneke, and Rainer Busch. Robust yaw control design with active differential and active roll control systems. *IFAC Proceedings Volumes*, 38(1):73–78, 2005.

[130] Aldo Sorniotti and Nicolò D'Alfio. Vehicle Dynamics Simulation to Develop an Active Roll Control System. pages 2007–01–0828, April 2007.

[131] Jing Zhao, Pak Kin Wong, Xinbo Ma, and Zhengchao Xie. Chassis integrated control for active suspension, active front steering and direct yaw moment systems using hierarchical strategy. *Vehicle System Dynamics*, 55(1):72–103, January 2017.

[132] Hyundong Her, Kyongsu Yi, Jeeyoon Suh, and Chongkap Kim. Development of Integrated Control of Electronic Stability Control, Continuous Damping Control and Active Anti-Roll Bar for Vehicle Yaw Stability. *IFAC Proceedings Volumes*, 46(21):83–88, 2013.

[133] H. Her, Y. Koh, E. Joa, K. Yi, and K. Kim. An Integrated Control of Differential Braking, Front/Rear Traction, and Active Roll Moment for Limit Handling Performance. *IEEE Transactions on Vehicular Technology*, 65(6):4288–4300, 2016.

[134] B. Houska, H. J. Ferreau, and M. Diehl. ACADO Toolkit – An Open Source Framework for Automatic Control and Dynamic Optimization. *Optimal Control Applications and Methods*, 32(3):298–312, 2011.

[135] H. J. Ferreau, C. Kirches, A. Potschka, H. G. Bock, and M. Diehl. qpOASES: A parametric active-set algorithm for quadratic programming. *Mathematical Programming Computation*, 6(4):327–363, 2014.

Ringraziamenti

Non posso che manifestare la mia riconoscenza verso il Prof. Aldo Sorniotti, Davide Tavernini e Umberto Montanaro, con i quali ho avuto l'onore di collaborare e realizzare gran parte del lavoro racchiuso in questa tesi.

Ringrazio anche tutti i ragazzi che ho conosciuto durante la mia esperienza presso l'Università del Surrey. Un riconoscimento particolare va a Gil Martins, il cui contributo è stato determinante per realizzare lo studio presentato nel secondo capitolo.

Rivolgo inoltre un sentito ringraziamento al Prof. Carlo Concari e al mitico gruppo di ricerca della "Palazzina 4".

Grazie davvero di cuore a tutti gli amici di Parma, con i quali ho condiviso momenti fantastici nel corso di questi tre anni di dottorato. A proposito: a quando la prossima merenda?

Ma senza dubbio un ringraziamento veramente speciale va ad Alessandro Soldati, eccezionale guida scientifica e morale, che più di ogni altro mi ha sostenuto e incoraggiato verso i traguardi più ambiziosi.